UNIVERSIDADE DE SÃO PAULO
INSTITUTO DE FÍSICA DE SÃO CARLOS

Lucca Radicce Justino

Exploring the inert doublet model of dark matter with very high-energy gamma-rays observatories

São Carlos

2024

Lucca Radicce Justino

Exploring the inert doublet model of dark matter with very high-energy gamma-rays observatories

Dissertation presented to the Graduate Program in Physics at the Instituto de Física de São Carlos da Universidade de São Paulo, to obtain the degree of Master in Science.

Concentration area: Theoretical and Experimental Physics

Advisor: Prof. Dr. Aion da Escóssia Melo Viana

Coadvisor: Dr. Clarissa Martins Siqueira

Versão corrigida

(Versão original disponível na Unidade que aloja o Programa)

São Carlos

2024

Justino, Lucca Radicce
Exploring the inert doublet model of dark matter with very high-energy gamma-rays observatories / Lucca Radicce Justino; advisor Aion da Escóssia Melo Viana; co-advisor Clarissa Martins Siqueira - corrected version -- São Carlos 2024.
135 p.

Dissertation (Master's degree - Graduate Program in Theoretical and Experimental Physics) -- Instituto de Física de São Carlos, Universidade de São Paulo - Brasil , 2024.

1. Dark matter. 2. Gamma-ray astronomy. 3. Indirect detection. 4. Inert doublet model. I. Viana, Aion da Escóssia Melo, advisor. II. Siqueira, Clarissa Martins, co-advisor. III. Title.

To my grandparents, Gilberto and Elza Maria

ACKNOWLEDGEMENTS

To my family for all their support in all these years, especially my mother, father, brother, and uncle and aunt.

To Prof. Aion da Escóssia Melo Viana for accepting me as a student. I am grateful for his orientation and guidance over the last three years. His work and dedication were fundamental for the progress and completion of this project. His advice helped me to walk in my professional and scientific career. I can only thank him for all this support.

To Dr. Clarissa Martins Siqueira for all the guidance as my co-adviser. Her knowledge and dedication were fundamental for the development of this work. Her help and attention have been of fundamental importance for me.

To Prof. Edivaldo Moura Santos and to Prof. Enrico Bertuzzo for the revision of this work as members of the Thesis committee and for their suggestions for its final version.

To Prof. Luiz Vitor de Souza Filho, Prof. Carlos José Todero Peixoto and Prof. Leonardo Paulo Maia for their participation in the APOEMA group. I am grateful to Prof. Luiz Vitor de Souza Filho for his leadership of the group and Prof. Leonardo Paulo Maia for his classes on statistical and mathematical physics and for his professional advice.

To Prof. Attilio Cucchieri for accepting me as his student of scientific initiation. To Prof. Ana Paula Peron for accepting me as her assistant in Calculus II classes. To all my professors and mentors during these six years at the São Carlos Institute of Physics. Especially Prof. Eric de Castro e Andrade, Prof. Frederico Borges Britto and Prof. Daniel Augusto Turolla Vanzella. I am especially grateful to Prof. Vanzella for his classes on relativity and cosmology.

To all my friends and colleagues of the APOEMA group, in alphabetic order: Ana Vitoria de Almeida Martinheira Braga, Andrés Gabriel Delgado Giler, Bruna Vaz, Cainã Oliveira, Daniel Cecchin Momesso, Davi Bessa de Souza, Guilherme Santana Pereira, Igor Reis, Juan Vítor Fagiani, Julia Gouvêa Mamprim, Leandro Matheus Morais da Silva, Luciana Andrade Dourado, Maria Eliza de Melo Ramos, Matheus Duarte Francisco, Micael Jonathan Duarte Andrade, Murillo Gregorio Grefener da Silva, Tales Ferraz de Paula, Tales Leme Mundo, Victor Bastos Canut Costa and Vinicius dos Santos Malafatti

To the postdocs in the APOEMA group, in alphabetic order: Guillermo Gerardo Rivera Gambini, Luan Bonneau Arbeletche, Luiz Salvador Miranda Palacios, and Tania Elizabeth Medina Torrejón.

To all students and researchers of other institutions for their collaboration. Espe-

cially to Jacinto Paulo Neto, Letícia Valença Guedes, Lucía Correa Angel, and to Prof. Farinaldo da Silva Queiroz for his lectures on dark matter science.

To all my friends and colleagues I made in the São Carlos Institute of Physics and the São Carlos City, especially to Vinícius Pereira Pinto, Vinícius Jerez Costa, Saulo Serejo Paschoa Sobrinho, Rafael De Oliveira Moura, Nataly Melo Campos and Marcos Vinícius Ribeiro Ferreira.

To CAPES and São Paulo Research Foundation (FAPESP) (grants 88887.684414/2022-00 and 2022/01962-0) for their financial support.

To the São Carlos Institute of Physics for providing my superior education and my academic formation as a physicist. To the employees of the Institute, especially Ricardo Vital do Prado, from the postgraduate program, for his assistance with administrative issues, and Maria Neusa de Aguiar Azevedo, from the Library, for helping me with the formatting of the text.

To the University of São Paulo for giving me the academic opportunities I had and for its contributions to Science in Brazil.

To all the people who believe in the importance of Science and Education.

"Each one of us composes our own story"
Almir Sater and Renato Teixeira
"The good life is one inspired by love and guided by knowledge"
Bertrand Russell
"Our knowledge can only be finite, while our ignorance must necessarily be infinite"
Karl Popper

ABSTRACT

JUSTINO, L. R. **Exploring the inert doublet model of dark matter with very high-energy gamma-rays observatories**. 2024. 135p. Dissertation (Master in Science) - Instituto de Física de São Carlos, Universidade de São Paulo, São Carlos, 2024.

One of the most intriguing problems in particle physics and cosmology nowadays is the so-called dark matter problem. We have several evidences, like galaxy rotation curves, galaxy cluster collision, baryon acoustic oscillation, structure formation, among others, implying that we need a new particle, beyond the standard model of particle physics, to explain the major matter component of the universe and to address all these evidences. One primary direction for dark matter searches is for Weakly Interacting Massive Particles (WIMPs). These are particles with masses in the GeV – TeV range and weak-scale interaction strength. The attempts to discover the dark matter particle could be via collider, direct and indirect detection searches. In the indirect scenario, dark matter particles may self-annihilate on stable standard model particles, such as neutrinos, cosmic rays and gamma rays, which can be detected by experiments on Earth. In the WIMP paradigm, a viable model for dark matter particles must predict the observed abundance as a thermal relic of the early universe through a freeze-out mechanism. Indirect detection searches can give constraints in the parameter space of velocity-averaged annihilation cross-section $\langle \sigma_{ann} v \rangle$ versus the dark matter particle mass, and are complementary to relic abundance and direct detection limits. In this work, we study the phenomenology of a specific model of dark matter particle, the *Inert Doublet Model*, and evaluate the sensitivity of gamma-ray observatories (like HESS and CTA) to detect an annihilation signal in the Galactic Center region.

Keywords: Dark matter. Gamma-ray astronomy. Indirect detection. Inert doublet model.

RESUMO

JUSTINO, L. R. **Explorando o modelo de dubleto inerte de matéria escura com observatórios de raios gama de muito altas energias**. 2024. 135p. Dissertação (Mestrado em Ciências) - Instituto de Física de São Carlos, Universidade de São Paulo, São Carlos, 2024.

Um dos problemas mais intrigantes da física de partículas e da cosmologia, atualmente, é o problema da matéria escura. Temos diversas evidências, como curvas de rotação de galáxias, colisão de aglomerados de galáxias, oscilação acústicas de bárions, formação de estruturas em larga escala, entre outros, implicando que precisamos de uma nova partícula, além do modelo padrão da física de partículas, para explicar a principal componente de matéria do universo e explicar todas essas evidências. Uma direção principal para pesquisas de matéria escura é as *Weakly Interacting Massive Particles* (WIMPs). Essas seriam partículas com massas na faixa de GeV – TeV e interação na escala da força fraca. As tentativas de descobrir a partícula de matéria escura podem ser feitas através de colisores, buscas de detecção direta e indireta. No cenário de detecção indireta, partículas de matéria escura podem se autoaniquilar em partículas estáveis do modelo padrão, como neutrinos, raios cósmicos e raios gama, que podem ser detectados por experimentos na Terra. No paradigma das WIMPs, um modelo viável para partículas de matéria escura deve prever a abundância observada como um relíquia térmica do universo primordial através do mecanismo de *Freeze-out*. Buscas de detecção indireta pode fornecer restrições no espaço de parâmetros da seção transversal de aniquilação com média de velocidade $\langle \sigma\, v \rangle$ versus a massa de partícula de matéria escura m_{DM} e são complementares à abundância de relíquia e limites de detecção direta. Neste trabalho estudamos a fenomenologia de um modelo específico da partícula de matéria escura, o Modelo de Dubleto Inerte, e estimamos a sensibilidade de observatórios de raio gamma (como HESS e CTA) para detectar um sinal de aniquilação na Região do Centro Galáctico..

Palavras-chave: Matéria escura. Astronomia de raios gama. Detecção indireta. Modelo de dubleto inerte.

LIST OF FIGURES

LIST OF TABLES

LIST OF ABBREVIATIONS AND ACRONYMS

SM	Standard Model of Particle Physics
DM	Dark Matter
CBM	Cosmic Microwave Background
BAO	Baryon Acoustic Oscillations
MOND	MOdified Newtonian Dynamics
ΛCDM	Λ Cold Dark Matter Model
CP	Charge conjugation-Parity (symmetry)
NFW	Navarro-Frank White
PPPC 4 DM ID	Poor Particle Physicist Cookbook for Dark Matter Indirect Detection 4
SIDM	Self-Interacting Dark Matter
SD	Spin-Dependent
SI	Spin-Independent
DD	Direct Detection
ID	Indirect Detection
GC	Galactic Center
EW	ElectroWeak
VIB	Virtual Internal Bremsstrahlung
GRB	Gamma-Ray Burst
IACT	Imaging Atmospheric Cherenkov Telescope
LAT	Large Area Telescope
HAWC	High-Altitude Water Cherenkov Gamma-ray Observatory
LHAASO	Large High Altitude Air Shower Observatory
SWGO	Southern Wide-Field Gamma-ray Observatory

HESS	High Energy Stereoscopic System
VERITAS	Very Energetic Radiation Imaging Telescope Array System
MAGIC	Major Atmospheric Gamma Imaging Cherenkov telescope
CTA	Cherenkov Telescope Array
CTAO	Cherenkov Telescope Array Observatory
LST	Large Sized Telescope
MST	Medium Sized Telescope
SST	Small Sized Telescope
IRF	Instrument Response Function
LLRT	Log-Likelihood Ratio Test
IDM	Inert Doublet Model
LHC	Large Hadron Collider
LEP	Large Electron-Positron collider
EWPT	ElectroWeak Precision Test
MSSM	Minimal Supersymmetric Standard Model

LIST OF SYMBOLS

ρ	Mass/energy density
M or m	Mass
K	Kinetic energy
U	Potential energy
v	Velocity
G	Newton's gravitational constant
R or r	Radius/distance
σ	Cross-section
$\langle \sigma\, v \rangle$	Thermally-averaged cross-section
H	Hubble parameter
a	Scale factor
n	Number density
f	State function
E	Energy
x	Rescaled time
Y	Abundance
Γ	Interaction rate
J	J-factor
D	D-factor
$\frac{dN}{dE}$	Annihilation spectrum
B_i	Branching ratio
$\mathcal{L}$	Likelihood
TS	Test statistic
D_μ	Covariant derivative
Δ	Mass-splitting

CONTENTS

1 INTRODUCTION

So far, Science has been the best way to understand the world around us. One of its fundamental objectives is to understand what the Universe is composed of and how its constituents interact. After several decades of development, models of two extreme scales arose. At the microscopic level, the Standard Model of Particle Physics (SM) seems to be the best description of what are the fundamental constituents of matter and how their interactions work. At the cosmological level, General Relativity is the best theory to describe the large scale of the Universe and to understand its evolution. Several evidences have suggested that the major matter component in the Universe interacts gravitationally but not with light, and neither seems to interact significantly with ordinary matter through other fundamental forces. However, the SM has no candidate that fulfills all the requirements and several other extensions of SM try to explain it. One of the main approaches is to consider that dark matter is composed of a new particle, beyond the Standard Model. Especially interesting are the Weakly Interacting Massive Particles (WIMPs) because they predict the right observed abundance of dark matter in the Universe. These are massive particles, with masses in the GeV - TeV range, and which have interactions with the SM of the order of the weak scale interaction strength. Due to its couplings with the SM, WIMPs are dark matter candidates that could be detected in ways other than only by gravity.

Among the detection methods of WIMPs are collider searches, direct detection, and indirect detection. In the indirect detection strategy, we expect that dark matter particles in highly dense astrophysical environments may self-annihilate or decay. These particles will then produce stable SM particles, such as photons, cosmic rays, and neutrinos, that will travel throughout space and eventually reach the Earth. If an excess of one of these cosmic messengers is detected, this signal could indicate a discovery of dark matter particles in the Universe. Cosmic rays are strongly affected by propagation effects while neutrinos are very hard to detect, due to their very small interactions. Gamma rays at TeV scale, in turn, do not suffer propagation effects in galactic scales and are easier to detect. With this method, we are able to probe the annihilation cross-section $\langle \sigma_{\rm ann}\, v \rangle$ (or decay time τ_{DM}) and the mass m_{DM} of the dark matter particle. The largest signal from dark matter annihilation is expected to come from the Galactic Center (GC), due to its proximity to Earth. Using Imaging Cherenkov Telescopes Arrays (IACTs) such as the working telescope HESS or the future CTA observatory is the best way to search for indirect detection signals of WIMPs with masses in the TeV scale.

In this work, we aim to analyze the phenomenology of a specific model of dark matter and evaluate the indirect detection limits from gamma rays associated to annihila-

tion in this model. The model we chose to analyze is the *Inert Doublet Model* (IDM). This is a minimal extension of the scalar sector of the SM where a new scalar doublet is added and its lightest state becomes a candidate for dark matter. The IDM has an interesting property that, due to the presence of partner particles of the doublet, co-annihilation processes enhance the effective annihilation cross-section. This improves the annihilation signal making it a promising model to be searched by indirect detection. Previous results have pointed out that CTA will be able to probe almost all the scenarios of the model. In this work, we intend to use the new, updated, instrument response functions of CTA and the new data from HESS to update the indirect detection limits on the IDM. In both cases, we take the GC as the target. We also intend to analyze the complementarity of indirect detection with direct detection and relic abundance constraints.

This dissertation is structured as follows: chapter 2 lists the main evidences of dark matter and some of the principal candidates to explain it. A brief summary of the Λ Cold Dark Matter (ΛCDM) model of cosmology is presented. Chapter 3 presents the WIMP dark matter paradigm, where dark matter is expected to be thermally produced in the Early Universe. Then, the dark matter halo models are shown. The final sections of the chapter discuss the methods of detection of particle dark matter and the gamma-ray flux from dark matter annihilation. Chapter 4 deals with how gamma-ray telescopes can be used for dark matter indirect detection. The main instruments and techniques are cited and the likelihood method for statistical analysis is presented. At the end of this chapter, the ON/OFF methodology in the GC is shown. In chapter 5, the IDM is reviewed, from its lagrangian to all the relevant interaction cross-sections. We also review the constraints from theoretical considerations, colliders, direct detection, and relic abundance. Chapter 6 shows the results of indirect detection limits to the IDM and the comparison with the other limits.

2 EVIDENCES AND CANDIDATES FOR DARK MATTER

Dark matter is one of the major questions of modern science. Current data point out that $\approx 85\%$ of the matter content of the Universe is non-baryonic. (7) This means that most of matter in the Universe is composed of something different from the matter that composes chemical elements, stars, planets, and all the stuff we are familiar with. Nowadays, the main hypothesis for explaining this problem is that dark matter is composed of a particle beyond the Standard Model.

The first suggestion of invisible mass in galactic scales started in the early 20th century with estimations of the local density of gravitational matter in the vicinity of the Sun. (10) It was, however, with the studies of the dynamics of the Coma Cluster, by Fritz Zwicky (11), that the existence of missing matter became clear. This problem had been treated as a problem of astronomy without connection with cosmology or particle physics for many decades. (10) The importance of the dark matter problem started to be recognized by the rest of the scientific community with the studies of galaxy rotation curves by Rubin and Ford in the 1970s. Since then, it has become clear that some kind of matter dominates gravitationally the Universe in both galactic and cosmological scales.

This chapter will present the main evidences of the existence of dark matter such as the evidence of galaxy clusters' velocity dispersion, galaxy rotation curves, the Cosmic Microwave Background, Large Structure Formation, and gravitational lensing. After that, the principal types of theory to explain dark matter will be presented. Among them, we can cite modified gravity theories, compact objects, and primordial black holes. One of the most promising candidates for dark matter comes from extensions of the Standard Model that predicts a non-relativistic (cold) dark matter particle. At the end of this chapter, the standard cosmological model of cold dark matter will be presented.

2.1 Evidences for dark matter

The first significant evidence that the Universe is filled by some kind of matter that is different from the ordinary, baryonic, matter, which we are familiar, arose with the studies of the velocity dispersion of galaxy clusters by Swiss astronomer Fritz Zwicky during the 1930s. (11) Using the virial theorem to relate the mass of the Coma Cluster with the size of the Cluster he estimated the dispersion velocity of the galaxies and compared it with observations. He noticed a discrepancy of around 100 times more matter than there could be according to optical observations. He called the invisible amount of matter in the cluster "dunkle materie" (in German, dark matter). These studies did not receive the proper attention of the physics community and the awareness of the importance of this problem had to wait until the first results by Rubin and Ford on the galaxy rotation

curves in the 1970s. (10)

The idea, however, that galaxies could contain some amount of non-luminous matter was not first proposed by Zwicky or Rubin. In the early 1900s, Lord Kelvin applied the kinetic theory of gases to the stars of the Milky Way and determined the relation between the stars' velocity and the size of the galaxy, considering the action of the gravitational law. (12) Based on the agreement of the estimation of the velocity dispersion by Kelvin with observations, the French mathematician Henri Poincaré observed that the quantity of non-visible matter ("matière obscure" (10) in French) should be of order or less than the amount of visible matter in the galaxy. (13) A detailed model of the structure and dynamics of the Milky Way was first developed by the Dutch astronomer Jacobus Kapteyn. He considered the stars in the Galaxy as particles in a gas. With this, he could establish the local density of dark matter as around $\rho_{DM} = 0.099\,\mathrm{M}_{\odot}\mathrm{pc}^{-3}$. Other researchers have found different values, but all in the same order of magnitude(10), $\rho_{DM} = 0.143\,\mathrm{M}_{\odot}\mathrm{pc}^{-3}$ according to Jeans (14) and $\rho_{DM} = 0.092\,\mathrm{M}_{\odot}\mathrm{pc}^{-3}$ according to Oort. (15) What those scientists had in mind with dark matter is not what we usually understand today, that would be a new particle or a new kind of law of gravity, but just faint stars, gas, solid objects, etc. (10) Anyways, the idea of using the dynamics of the stars is still the approach to determine the local density of dark matter even nowadays. This determination is very important in direct and indirect detection searches of dark matter, which will be explained in the next chapter.

The next subsections will deal with the most important evidence of the existence of missing gravitational mass in galactic and cosmological scales. After that, more recent evidence of the existence of dark matter, such as from the Cosmic Microwave Background, structure formation, and gravitational lensing will be reviewed.

2.1.1 Zwicky and the Coma Cluster

In two papers, one published in 1933 (11) and the other in 1937, (16) Zwicky applied the virial theorem to estimate the velocity dispersion of the Coma Cluster and compared it with the measurements from the Doppler effect. The virial theorem states that the average over time of the total kinetic energy of a stationary conservative system is

$$\langle K \rangle = -\frac{1}{2} \sum_i \langle \mathbf{F}_i \cdot \mathbf{r}_i \rangle \,, \tag{2.1}$$

where $\mathbf{F}_i$ is the total force over the i-th particle and $\mathbf{r}_i$ is its position. If the only force present is a central force with potential $U_{ij}\left(r_{ij}\right) = a r_{ij}^n$, where r_{ij} the relative distance between two particles i and j, thus the virial theorem can be rewritten as

$$2\,\langle K \rangle = n\,\langle U \rangle \,, \tag{2.2}$$

where U is the total potential energy of the system. For the gravitational law, finally, we get

$$\langle U \rangle = -2 \langle K \rangle , \tag{2.3}$$

which can be used to relate the distribution of matter in a gravitationally bound stationary system, through U, with the velocities of particles implicit in K. Hereafter the average over time will be always considered and the brackets $\langle\rangle$ omitted.

Zwicky modeled the Coma Cluster as a sphere with a homogeneous distribution of matter of radius R and mass M. The internal potential energy of such a system is

$$U = -\frac{3GM^2}{5R}, \tag{2.4}$$

where G is Newton's gravitational constant. The total kinetic energy will be given by

$$2K = \sum_i m_i v_i^2 = \frac{3GM^2}{5R}. \tag{2.5}$$

In this expression, the velocities are not according to the observer frame, but in the center of mass frame. This means that the sum in the kinetic term is the velocity dispersion of the particles (in the considered case, the galaxies in Coma) as measured by an observer. Supposing that all the galaxies have the same mass,

$$\sum_i m_i v_i^2 = M \left\langle v^2 \right\rangle \implies \left\langle v^2 \right\rangle = \frac{3GM}{5R}, \tag{2.6}$$

where $\langle v^2 \rangle$ is the velocity dispersion, i.e., the mean square of velocities of the ensemble of particles.

With Eq. (2.6) Zwicky was able to relate the mass M, the radius R, and the velocity dispersion $\langle v^2 \rangle$ of the Coma Custer. He considered the average mass of each galaxy to be around $10^9 M_\odot$ and the total mass as the product of this value and 800 galaxies in the cluster. He estimated the size as $R = 10^6$ ly, which yields, according to Eq. (2.6), a velocity dispersion of about 80 km/s. (11) However, the measurements indicated a velocity dispersion of around 1000 km/s. This discrepancy, according to Zwicky, means that a large amount of dark matter would be present in the Coma Cluster, at least one order of magnitude higher than luminous matter.

In 1937 Zwicky redid his calculations of the Coma Cluster with some refinements. (16) He then considered 100 galaxies of $4.5 \times 10^{10}\ M_\odot$ of mass within 2×10^6 ly. Using the velocity dispersion of 700 km/s Zwicky has obtained a mass-to-luminosity ratio around 500 $M_\odot/L_\odot$, where $L_\odot$ is the solar luminosity. However, this calculation was overestimated because Zwicky applied a value for the Hubble constant of $H = 558\,\mathrm{km\,.\,s^{-1}\,.\,Mpc^{-1}}$ (17) around 8 times greater than the actual measurements of $H \approx 70\,\mathrm{km\,.\,s^{-1}\,.\,Mpc^{-1}}$. Despite this error, the magnitude of the mass-to-luminosity ratio in the Coma Cluster, $\approx 350 M_\odot/L_\odot$ according to modern estimations (18), still points to the presence of dark

matter in this system. That was the first robust evidence of the presence of non-luminous matter in the extragalactic scales. The convincing of the scientific community of this problem had to wait some decades for more evidence. In the next sections, we will review some of them.

2.1.2 Galaxy rotation curves

During the 1920s, when it started to become clear that the galaxies, such as Andromeda (M31), were objects outside the Milky Way, the measurements of redshift allowed us to estimate the velocity of the star around the galaxy centers. These measurements give an estimation of the gravitational mass in the galaxies. The luminosity of those galaxies can also be measured, given the mass-to-luminosity ratio, which can be compared with the value in the solar vicinity $M_{\odot}/L_{\odot}$. The pioneering works on this were done in the 1920s and 1930 by scientists such as Hubble (1926)(19), Oort (1932) (15) and Babcock (1939) (1). After World War II, developments in radio astronomy allowed measurements of the redshift of the 21 cm line of hydrogen in the outer parts of galaxies. An important advance in this technique was the determination of the first rotation curve in radio data of M31 by van de Hulst, Raimond, and Woerden. (20) Despite these studies having pointed mass-to-luminosity ratios slightly greater than expected it was usually understood as the result of absorption of the galactic light by gas and dust. The convenient results that were the first clear evidence of the existence of dark matter in the outer parts of galactic halos were established in the 1970s with results from the galaxy rotation data obtained by Rubin and Ford.

Before discussing the galaxy rotation data from the 1970s, let us briefly explain what would be the expected velocity rotation $v(r)$ dependency on the distance from the center r. The dynamics of stars in a spiral galaxy is quite a complex problem. The baryonic matter is distributed in the Bulge region, in the inner parts, which can be modeled as a sphere that ends at a given distance, a disk that extends to a greater radius, and a spherical low dense distribution of stars. Besides, the trajectories are expected to be elliptical and its solution is very difficult. We can, however, consider a simple toy-model where the orbits are circular and the mass distribution is spherically symmetric. In this case, the centripetal force expression and Gauss' law imply that the orbital velocity will be given by

$$v(r)^2 = \frac{GM(r)}{r}, \tag{2.7}$$

where $M(r)$ is the mass enclosed in the orbit of radius r.

For the small radius, the galaxy is dominated by the bulge, which can be modeled by a uniform sphere of radius r and total mass M. The mass within the radius r for a spherically symmetric distribution of density $\rho(\mathbf{r}) = \rho(r)$ is given by

$$M(r) = 4\pi \int_0^r \rho(r')\, r'^2 dr'. \tag{2.8}$$

The orbital velocity, inside and outside the total radius R, will be

$$v(r) = \begin{cases} \sqrt{\frac{4\pi G\rho}{3}}\, r & , r \leq R \\ \sqrt{\frac{GM}{r}} & , r > R \end{cases} . \tag{2.9}$$

This result means that, for a small radius, near the bulge, the orbital velocity must increase linearly with distance, while in the outer parts of the galaxy, the velocity goes to $v \sim 1/\sqrt{r}$, which is usually known as Keplerian curve.

The deviation from the Keplerian orbits described by Eq. (2.9) by distant stars would indicate the presence of different mass distributions from what was assumed as the main constituents of galaxies. Despite previous indications from the Coma Cluster by Zwicky or older studies of the galaxy rotation curves, it was in the 1970s that unequivocal evidence of the presence of a great amount of non-luminous matter came to light.

In 1970 the astronomers Kent Ford and Vera Rubin published the best measurements at the epoch for the rotation curve of Andromeda. (2) In the same year, Ken Freeman made a systematic study comparing the rotation curves predicted by the photometric measurements, i.e., the one expected by the presence of luminous matter only, and the 21 cm results. (4) Modeling the disk as a decreasing exponential, with a specific scale length fitted according to the photometric data, he has found that the rotation curves extended at further distances than expected, indicating that some amount of gravitational mass could be present at higher radii. In 1972 Rogstad and Shostak made a similar work, (21) where they found a mass-to-luminosity ratio around 20 at larger radii. M. Roberts and R. Whitehurst published in 1972 a rotation curve of M31 (3) and in the following year, together with Arnold Rots, they made the same analysis for M81 and M101. (22) In all the cases they concluded that the rotation curves must be flat at larger radii, i.e., in the outer regions of the galaxies.

In 1974 two important articles put together the evidence of missing mass from galaxy clusters and galaxy rotation curves indicating that the masses of galaxies have been underestimated by a factor of ten. (10) One by Ostriker, Peebles and Yahil, and the other by Einasto, Kaasik, and Enn Saar. (23) Albert Bosma, in his PhD thesis (24), showed the results of 25 galaxy rotation curves. He proved that the rotation curves extended far beyond the optical limits of the galaxies, indicating an important amount of unseen mass at larger distances. At the same epoch, Rubin, Ford, and Thonnard published rotation curves of ten spiral galaxies that also indicate a flat velocity at the outer distances from the center. (25)

But what does an almost constant orbital velocity mean? According to Eq. (2.9) the velocity of stars around the galaxy should drop out according to a $v \sim 1/\sqrt{r}$ law. Since the data from Rubin, Ford, Roberts, Whitehurst, and others indicated an almost flat velocity out of the luminous part of the galaxy, some matter distribution with different density may be present. According to Eq. (2.7) a constant velocity implies an enclosed

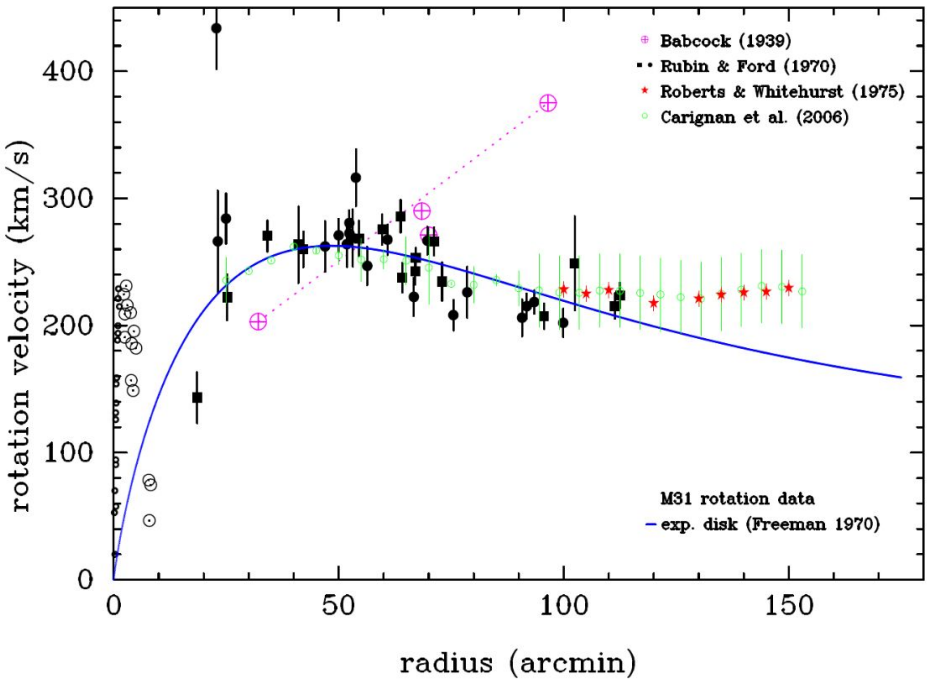

Figure 1 – Rotation curve of M31, according to data from Babcock (1), Rubin & Ford (2), and Roberts & Whitehurst (3). The exponential disk model by Freeman (4) is shown in solid blue.

Source: BERTONE; HOOPER. (10)

mass that grows linear to the distance r. For a spherically symmetric distribution, Eq. (2.8) implies that this is only possible if $\rho \sim 1/r^2$, i.e.,

$$v\,(r) \sim CONST \implies M\,(r) \sim r \implies \rho\,(r) \sim \frac{1}{r^2}. \tag{2.10}$$

This is one strong evidence that some amount of matter that is non-luminous is present in the galaxy in a $\sim 1/r^2$ profile halo beyond the end of the baryonic matter.

Figure 1 shows a compilation of different measurements of the galaxy rotation curve of M31 according to the studies cited before. It also presents the model by Freeman (4) and how the curve becomes flat around 100 arcmin, indicating the presence of a dark matter halo in the outer parts of the galaxy.

2.1.3 Cosmic Microwave Background

In 1948 the researchers Ralph A. Alpher and Robert C. Herman (26) followed the theory of the Big Bang elaborated by George Gamow (27) on the evolution of the primordial universe. In the Early Universe, baryons and leptons were in a primordial plasma and the photons were suffering Compton scatterings with the electric charges, the reason why the Universe is said to be opaque. As the Universe expanded its temperature dropped. At a certain point, the electrons are cooled enough to form atomic hydrogen

together with the nuclei, a phenomenon which is named recombination. Some moments later, around $z = 1100$, or 380,000 years after the Big Bang, when the mean energy of photons was $E \approx 0.3\,\text{eV}$ (28), the Thomson process $e^- + \gamma \leftrightarrow e^- + \gamma$ was no longer efficient, and the photons decouple and start to propagate freely throughout the Universe, i.e., the Universe becomes transparent to light. Throughout the Universe's expansion, this radiation has been redshifted and today its electromagnetic spectrum consists of a black body radiation in the infrared frequencies. In 1964 Arno A. Penzias and Robert W. Wilson detected an irremovable radio background signal at 4 GHz that seemed to be isotropic and unpolarized. (29) Dicke *et al.* (30) proposed that the signal detected by Penzias & Wilson was the black body radiation previously predicted by Alpher in 1948, with an expected temperature of a few Kelvins. The detection of the *Cosmic Microwave Background* (CMB) was one of the strongest evidence in favor of the Big Bang model. The present data give a black body radiation temperature of $T = 2.7255 \pm 0.0006\,\text{K}$. (31)

Studying the CMB is fundamental for observational cosmology because its data give important information about the evolution of the Universe, its energy composition, and structure formation. One of the principal features of the CMB is its anisotropies. Due to quantum fluctuations that expanded with the Universe, over-density and under-density regions of the baryonic matter were formed. From these excess-density regions the large structures of the Universe, such as galaxies and galaxy clusters, were formed. These regions are imprinted in the angular distribution of the CMB and tell us important information about the Universe at the epoch of decoupling. (28) The first observation of this effect was made by the Cosmic Background Explorer (COBE) satellite in 1990, which found anisotropies of the order $\Delta T \approx 30\,\mu\text{K}$. (32) After that, the Wilkinson Microwave Anisotropy Probe (WMAP) mission improved the CMB anisotropy measurements (33). Currently, the best telescope for studying the CMB is the Planck satellite (7) from which the most precise cosmology parameters come. The anisotropy map of the CMB temperature according to Planck is shown in Figure 2.

The anisotropies of the CMB temperature can be expanded in spherical harmonics of modes l from which the power spectrum $\mathcal{D}_l$ can be obtained. The power spectrum depends mainly on the Baryon Acoustic Oscillations (BAOs). In the Early Universe, the baryonic matter was attracted by the gravitational potential in the high density regions and repelled by the radiation pressure. These oscillations produced acoustic waves that propagate at the sound speed in this medium. These waves could propagate until the recombination epoch when the acoustic waves froze. The typical size of these waves is imprinted in the CMB and in the large structures of the Universe and, therefore, yields important information on the baryon distribution at the recombination time. (28) Dark matter is especially important for this phenomenon because it contributes to the gravitational potential but does not to the radiation pressure.

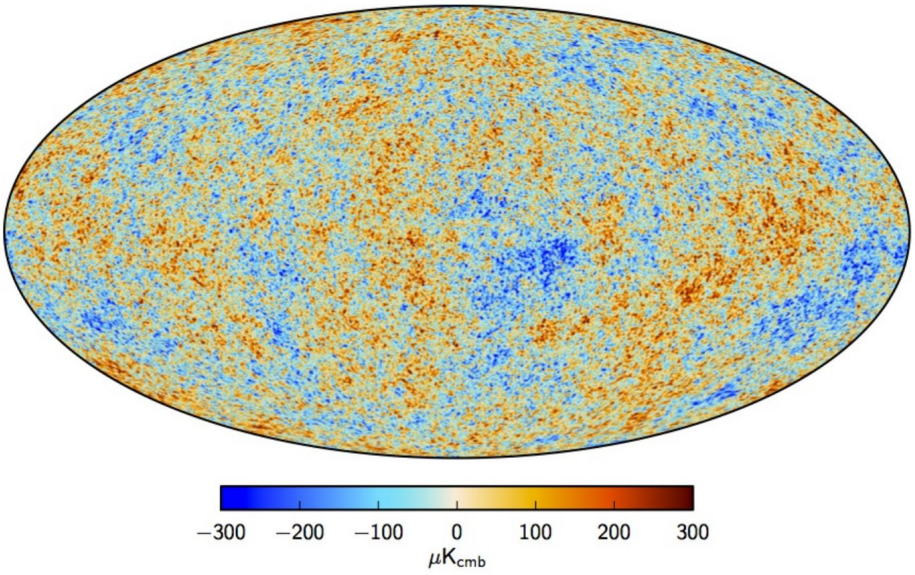

Figure 2 – Anisotropies map of the CMB temperature (in micro-Kelvin) as measured by the Planck satellite. The red spots indicate a positive fluctuation in the temperature while the blue spots indicate negative fluctuations.

Source: ADAM *et al.* (34)

Figure 3 shows the power spectrum measured by the Planck satellite. (7) In the first order, the first peak gives information about the curvature of the Universe (positive, negative, or flat); the second peak is related to the abundance of baryon matter; and the third to the dark matter abundance.

2.1.4 Large Scale Structure Formation

Large Scale Structures in the Universe refer to the distribution of galaxies in clusters of galaxies, superclusters, filaments of clusters, and cosmic void structures that are present in the Universe on large scales. The theoretical explanation for the Large Structure Formation is that the fluctuations in the matter density in the Universe expanded after inflation. These regions collapsed in the gravitational potentials forming the galaxies and clusters of galaxies. Simulations of this large scale universe formation started in the 1970s and were not able to explain the observed structure. (35) This problem is fixed when dark matter is taken into account. Dark matter enhances the baryon collapse and allows the formation of filaments of clusters of galaxies which is observed in large scale surveys. Between the filaments, there are regions with a low number of galaxies, known as cosmic voids.

Two important mappings of the sky show with precision the large scale structure of the Universe. They are the 2dF Galaxy Redshift Survey (2dFGRS) which mapped 543 galaxy clusters (37) and the Baryon Oscillation Spectroscopic Survey that was made

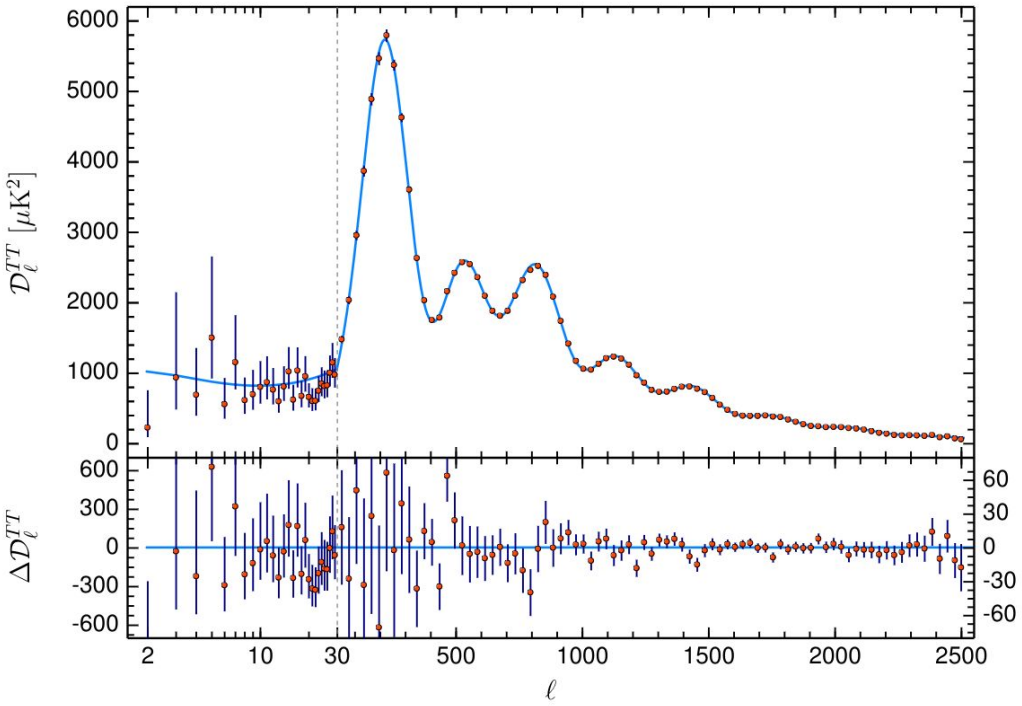

Figure 3 – Temperature power spectrum $\mathcal{D}_l$ of the CMB measured by the Planck satellite.

Source: AGHANIM *et al.* (7)

by the SDSS collaboration. (38) Not only observational advances were made but also numerical N-body simulations allowed the reconstruction of the large structure universe. One of them is the 'Millennium simulation', developed by the Max Planck Institute for Astrophysics (39), which simulated a cubic region of 2 billion light-years in each direction. The other one is the *AbacusSummit* simulation which considers $\approx$ 60 trillion particles and tests 97 different cosmological models. (40)

Figure 4 compiles the large structure surveys and simulations cited before. It is possible to see how galaxy clusters are bound together in filaments. Simulations show that this geometry is only possible if dark matter is taken into account. Without it, the Universe becomes more diffuse. Moreover, these simulations show that dark matter cannot be hot, i.e., a relativistic particle, because it would evaporate the original over-density regions of the Universe. In this sense, the observations and simulations of the large structure of the Universe provide convincing evidence of the existence of dark matter in the Universe. (36)

2.1.5 Gravitational lensing and the Bullet Cluster

The deflection and magnification of light by gravity is known as gravitational lensing. The idea that light could be deviated by gravity appeared for the first time in

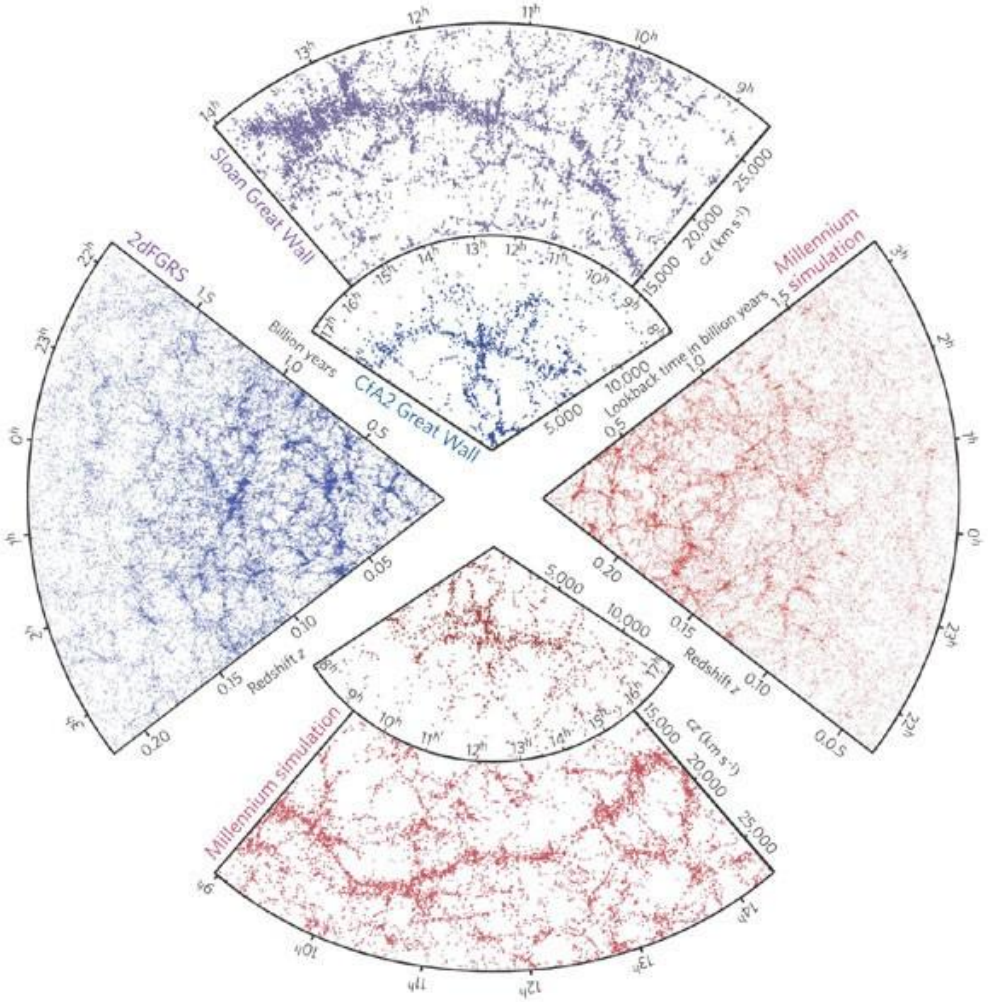

Figure 4 – Galaxy distribution according to redshift surveys and cosmological simulations. Top cones: the SDSS survey which shows the 'Sloan Great Wall', (5) one of the largest structures in the observable universe. Left cone: the 2dfGRS survey. Right and bottom cones: mock galaxy surveys obtained from the Millennium simulation, chosen to match the observed geometry.

Source: SPRINGEL; FRENK; WHITE. (36)

Newtonian theory. However, it was with Einstein's (1915) theory of General Relativity (GR) that the effect of gravity on light rays became clear. In GR gravity is nothing more than the effect of the geometry of space-time over matter and energy and vice versa. The trajectories of free particles, such as photons, are supposed to be geodesics in a given metric. Suppose that a light ray travels near a spherical and non-rotating mass distribution with total mass M and impact parameter b. In this case, the Schwarzschild

metric can be used. The deflection angle $\delta\phi$, in first order, will be given by (41)

$$\delta\phi = \frac{4GM}{b}, \tag{2.11}$$

twice the prediction of Newtonian gravity. This effect could be detected in a solar eclipse when the apparent positions of stars change with the presence of the Sun. It was observed in Sobral, Brazil, and São Tomé and Príncipe, West Africa, during the total solar eclipse of 1919. (42) The deflection of light by a massive body was the first test of GR. Since then, gravitational lensing has been used to estimate mass distributions in cosmology and astrophysics.

Gravitational lensing can be classified into three types: strong lensing, weak lensing, and microlensing. (43) Strong lensing occurs when gravity bends the light rays and makes them travel through different paths. With this, multiple images of the same object can be formed, or distortions of this object can be visible. With a mass distribution of circular symmetry the image of a ring can be formed (Einstein ring). Some geometries can provide multiple replicated images of the same object, such as the Einstein cross. (44) Strong lensing is produced, for instance, in galaxy clusters when background galaxy images are distorted by the gravitational potential of the cluster. Weak lensing occurs when just small deviations are present and the detection of the phenomenon is only possible with the statistical analysis of many light sources. This method is applicable in the search for dark matter in galaxy clusters. Measuring the weak lensing in these clusters provides the mass distribution present in it, and indicates the excess of the invisible mass. (45) Microlensing, in turn, consists of the amplification of the background light when a massive body passes in front of a light source but without detectable image distortion.

An important evidence in favor of the existence of dark matter is the weak lensing in the Bullet Cluster. (46) The Bullet Cluster (1E 0657-558) is a merger of two galaxy clusters where their centers of mass have passed through each other at approximately 4,700 km . s^{-1} leaving a shock-wave in the hot gas. In this type of cluster, the major component of baryonic matter is the hot gas (47) instead of the luminous matter of galaxies. In 2006 a group of astronomers compared the hot gas distribution obtained by X-ray maps of the Chandra telescope with the gravitational mass distribution obtained by weak gravitational lensing. They have concluded that there is a separation of the gravitational centers of the clusters and the gas distribution. (46) Moreover, the luminous matter remains mostly bound by the gravitational potential estimated by weak lensing. This decoupling of most of the baryonic matter (gas) and the gravitational matter is considered the first direct evidence of dark matter in cosmological scales that alternative theories such as modifications of gravity have difficulty in explaining. Figure 5 shows the Bullet Cluster in the measurements of X rays and weak lensing where it is possible to see a clear decoupling between the baryonic matter and the gravitational matter.

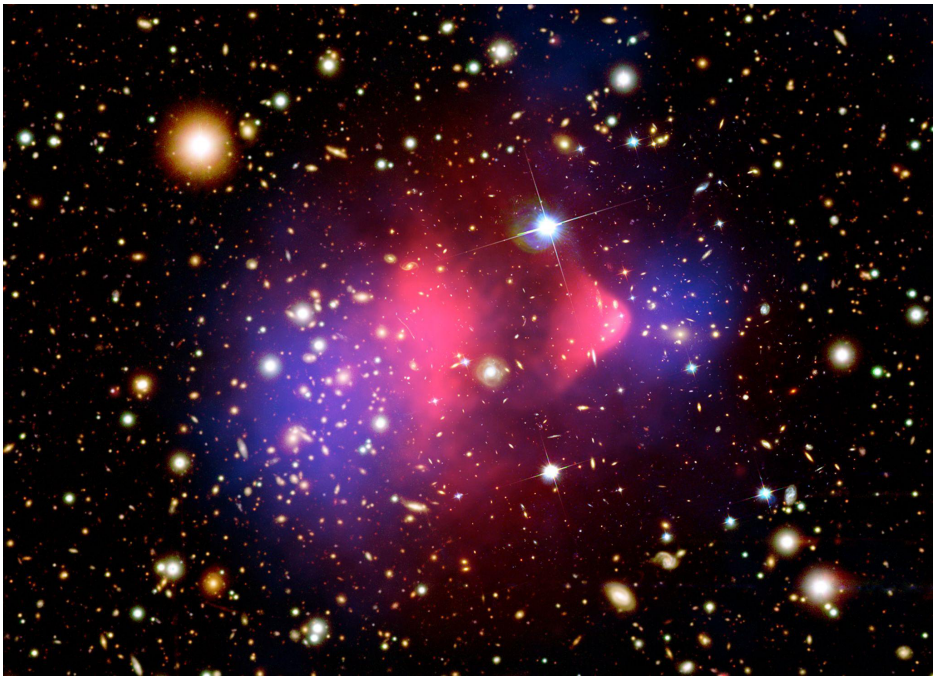

Figure 5 – The Bullet Cluster (1E 0657-558) in three different signals: optical (galaxies), X rays from the hot gas (red), and the gravitational matter (blue).

Source: ESA. (48)

The Bullet Cluster can also impose constraints on the self-interaction of dark matter. The data and simulations of the Bullet Cluster pointed out that the mass distribution behaves collisionless and puts an upper limit for self-interaction of a hypothetical particle of dark matter as (49)

$$\frac{\sigma}{m_{DM}} < 1.25\,\mathrm{cm}^2.\mathrm{g}^{-1}, \tag{2.12}$$

where σ is the cross-section of the self-interaction of dark matter and m_{DM} is its mass.

This section has reviewed the main evidence of the existence of missing mass in astrophysical and cosmological scales. The next section shows the principal candidates to explain the missing mass problem and the conditions that these theories have to obey.

2.2 Candidates for dark matter

As discussed in the previous section, several evidences indicate that the major component of matter in the Universe is not composed of the baryonic matter that we are familiar with. There are many theories to explain the dark matter problem (also called the missing mass problem). One of the first ideas to explain the missing mass problem was to suppose that, at galactic scales, gravity acts differently from Newton's law. As will be briefly discussed later, these theories have problems with some evidence such as structure formation and the Bullet Cluster. When it became clear that dark matter was a very important problem to cosmology, some particle physicists started to search for

particle candidates to explain dark matter. The observational evidence of dark matter establishes some basic properties that usually must be fulfilled by a satisfactory particle physics theory of dark matter:

- **1) Neutral**: dark matter must be electrically neutral to avoid interactions with electromagnetic radiation. Otherwise, it would be visible and the discrepancy between luminous and non-luminous matter would not be present. Even supposing a non-integer charge, the limits on the electric charge are strong, $q_{DM} \lesssim 10^{-14}\,(\mathrm{m/GeV})\ e$, (50) where e is the elementary charge.

- **2) Interactions**: dark matter certainly interacts through gravitation, as all previous evidence indicated. The Bullet Cluster imposes a superior bound to the self-interaction cross-section to mass ratio $\sigma/m_{DM} < 1.25\mathrm{cm}^2.\mathrm{g}^{-1}$. (49) This means that, for most proposals, dark matter can be considered non-collisional. Other interactions with the Standard Model sector are not guaranteed but many of the dark matter models suppose it to obtain thermal relic dark matter density. This is especially true for WIMP models which will be discussed later.

- **3) Cold or warm**: Large Scale Structure Formation suggests that dark matter cannot be hot, i.e., it must not have been relativistic at the epoch of structure formation. The numerical simulations of structure formation showed that hot dark matter, such as standard neutrinos, would first form structures and then collapse into smaller dark matter halos, i.e., a top-down structure formation, while cold or warm dark matter would follow a bottom-up formation. The comparison with galaxy surveys has shown that hot dark matter is not compatible with the observed structure of the Universe. (51)

- **4) Stable**: since most of the matter in the Universe is composed of dark matter, it could not be an unstable particle with a lifetime smaller than the age of the Universe. Otherwise, dark matter would have decayed and it would not be detectable nowadays. Current bounds put an inferior limit for the decay lifetime of the dark matter particle as $\tau_{dDM} \gtrsim 10 f_{dDM} \tau_{\mathrm{uni}}$, (52) where τ_{dDM} is the lifetime of decaying dark matter, f_{dDM} is the fraction of dark matter that is unstable and τ_{uni} is the age of the Universe.

- **5) Right abundance**: a dark matter model must provide the right abundance according to CMB data. As cited before the abundance Ω_{DM} of dark matter can be obtained by the power-spectrum of the CMB temperature (see Figure 3). The actual data from the Planck satellite provide $\Omega_{DM} h^2 = 0.1200 \pm 0.0012$. (7) In section 3.1.3 we will discuss how the WIMP candidates can explain the right dark matter abundance.

2.2.1 Main explanations for the missing mass problem

Since the 1980s, when the galaxy rotation data and structure formation studies became robust, several theories have been proposed. Among them, the modified gravity theories provided good predictions for galaxy rotation data but failed to explain structure formation and other observations. New theories of modified gravity were proposed but still have some difficulties. (6) Another class of candidates is the *Massive Compact Halo Objects* (MACHOs) which would consist of faint luminous or dark astrophysical objects such as brown dwarfs, neutron stars and black holes. But they were already ruled out by microlensing and structure formation data. (10) The remaining candidates are particles that would satisfy the conditions cited before. (53) Since the standard neutrinos were discarded by structure formation many Beyond Standard Model of Particle Physics (BSM) candidates arose. Many of these models emerged from the solutions to the hierarchy problem and others from particle physics. (54) All these candidates for dark matter are resumed in Figure 6 and described below.

Figure 6 – Diagram of models of dark matter grouped in clusters of theories.

Source: BERTONE; TAIT. (55)

- Modified Gravity: the first proposal of adapting the gravitational law to explain the galaxy rotation data was made by Milgrom in 1983. (56) He proposed that Newton's

2nd law would change at low acceleration, assuming the form

$$\mathbf{F} = m\mu\left(\frac{a}{a_o}\right)\mathbf{a}, \tag{2.13}$$

where a is the scalar acceleration and μ is a function that goes $\mu(x) \to 1$ if $a \gg a_o$ and $\mu(x) \to x$ if $a \ll a_o$. With this new law, Milgrom was able to explain the galaxy rotation data, obtaining a value of $a_o \approx 10^{-8}\,\mathrm{cm^2.s^{-1}}$. (57) This theory, the *MOdified Newtonian Dynamics* (MOND), however, has problems explaining other data such as the Bullet Cluster (46), galaxy clusters (58), the CMB and structure formation. (59) Other theories of modified gravity try to change gravity at the GR level. One of the most important among them is the *Tensor-vector-scalar gravity* (TeVeS) theory. (60) It proposes that beyond the tensor field of GR $g_{\mu\nu}$, there are a scalar field ϕ and a vector field V_μ that are responsible for the effects associated with dark matter. This theory has advantages such as explaining some data of gravitational lensing (61) but still has problems with data from CMB and structure formation. (59)

- MACHOs: one of the simplest hypotheses to explain dark matter is to suppose that it is composed of compact objects with very low luminosity such as planets, brown dwarfs, white dwarfs, neutron stars, black holes and so on. Kim Griest called them *Massive Astrophysical Compact Halo Objects*. MACHOs should produce gravitational microlensing effects on the Milky Way stars. (62) Several microlensing observations have discarded MACHOS as the major component of dark matter in our galaxy. (63) MACHOs are also problematic given they are of baryonic origin and CMB data points to a discrepancy between baryonic and the total matter in the Universe. (7)

- Primordial Black Holes: a special type of MACHO is the *Primordial Black Holes* (PBH). They can evade the usual constraints of MACHOs from the CBM. (64) PBHs have gained the attention of the community since they can be obtained in standard cosmology (65) and were suggested as candidates for the black hole binary merger detected by LIGO. (66) The main important constraint to the mass of PBH mass is Hawking radiation (67) which puts the upper limit of $\sim 10^{-18}\,M_\odot$. PBHs are also constrained by microlensing (68), CMB (69), X rays and radio (70), and gamma-ray bursts. (71) Despite these constraints, PBHs are still possible candidates to explain at least part of dark matter in the Universe or even all the dark matter abundance in a slight region of the parameter space.

- Axions and axion-like particles: axions arise as a solution for the strong CP problem. (72) (73) Axions would be light bosons that could predict many dark matter observations. (53) Due to their small interactions they could not have been produced by standard thermal processes in the Early Universe. If axions are dark matter other production mechanism is necessary. (74) Inspired by the axions, similar particles,

called *axion-like particles* (ALPs), (75) were proposed. The parameter space of ALP consists of its mass and coupling to the electromagnetic field. They are viable dark matter candidates and can be probed by different kinds of experiments such as optics experiments or effects on the gamma rays propagation. See Ref. (76) for further details.

- Sterile Neutrinos: as discussed previously, SM neutrinos are already excluded as dark matter candidates due to structure formation. (51) But particles similar to neutrinos without the weak coupling to the leptons (77) are still viable candidates for dark matter. The *sterile neutrinos* were first proposed by Dodelson & Windrow in 1994. (78) A sterile neutrino appears in many extensions of the SM as a right-handed neutrino that is mixed with the SM left-handed neutrino. Sterile neutrinos appear in many extensions of the SM to explain the problem of neutrino masses. (77) This mixture implies that right-handed neutrinos will eventually decay into SM neutrinos. If the decay lifetime is larger than the age of the Universe, these sterile neutrinos can act as dark matter candidates. (77) In other models, the dark matter particle has a portal to right-handed neutrinos. Further details of these models can be seen in Refs (79) and (80).

- WIMPs: the *Weakly Interacting Massive Particles* (WIMPs) are hypothetical particles with mass m lying in the GeV - TeV scale with interactions with the SM sector in the order of the weak scale, i.e., $\sigma v \sim G_F^2 m^2$. The term WIMP encodes a set of different classes of particle models that have been proposed since dark matter was understood as an important problem in cosmology and particle physics (see Refs (81) (82) (83) for instance). Historically, supersymmetric candidates and solutions of the hierarchy problem were the first popular WIMPs in the community. (10) Neutral Supersymmetric particles such as neutralinos, gravitinos and axinos arise as natural dark matter candidates. (84) (85) Other kinds of candidates are, for instance, states from extra dimensions in Kaluza-Klein models (86), candidates from little Higgs models (87) and other extensions of the scalar sector (88). WIMPs can be produced by thermal processes in the Early Universe, following the established paradigm of thermal relic production, and predict the exact amount of dark matter that is observed according to CMB data. For this reason, WIMPs are very promising candidates. This property will be further explained in subsection 3.1.3.

In the next section, let us review the consequences of cold dark matter for cosmology and how the CMB measurements constrain this assumption.

2.3 Cosmology and the ΛCDM Model

The idea that dark matter is a fundamental ingredient of the Universe's composition, together with other considerations, led to the establishment of a standard cosmological model. This model was proposed in 1995 by Ostriker and Steinhardt (89) and can address some of the most important problems in cosmology. The Λ *Cold Dark Matter* (ΛCDM) model is based on the following assumptions: 1) GR is the right theory of gravity and describes the Universe at cosmological scales. 2) the Universe is homogeneous and isotropic at large scales. 3) the Universe's content is composed of ordinary matter, cold dark matter and a cosmological constant. 4) A fast inflationary period occurred in the first moments after the Big Bang. 1) and 2) are the usual assumptions of standard cosmology. 3) is based on all the evidences of the existence of dark matter pointed out in section 2.1 plus the observation of an accelerated expansion rate of the Universe (dark energy). 4) address the horizon, the flatness, and the magnetic monopole problems. Let us briefly describe the dynamics of the Universe in this model.

In a homogenous and isotropic expanding universe, space-time is described by the FLRW metric given by

$$ds^2 = -c^2 dt^2 + a\left(t\right)^2 dl^2, \tag{2.14}$$

where ds^2 is the invariant interval, dt is the time differential, dl is the space differential and a is the scale factor, which accounts for the expansion of the Universe. In this metric, Einstein Equations of GR are reduced to the Friedmann equations, (90)

$$\begin{cases} H^2 = \frac{8\pi G\rho}{3} - \frac{k}{a^2} \\ \frac{\ddot{a}}{a} = \frac{-4\pi G}{3}\left(\rho + 3P\right) \end{cases}, \tag{2.15}$$

where ρ is the energy density in the Universe, P is its pressure, k is its curvature and H is the Hubble parameter, defined as

$$H = \frac{\dot{a}}{a}, \tag{2.16}$$

which is related to the actual Hubble constant by $H_o = H\left(t = 0\right)$. The speed of light is $c = 1$. The first Friedmann equation describes the Universe's expansion, while the second is acceleration. Beyond the Friedmann equations (2.15), energy conservation implies that the energy density must follow the relation

$$\frac{d\rho}{dt} = -3H\left(\rho + P\right). \tag{2.17}$$

These three equations give us the basic dynamics of an expanding universe.

It is more usual, however, to rewrite these equations in more convenient parameters. Defining the critical density of the Universe as

$$\rho_c = \frac{3H^2}{8\pi G}, \tag{2.18}$$

the energy density is now rewritten as the energy parameter defined as

$$\Omega = \frac{\rho}{\rho_c}. \tag{2.19}$$

Let us consider, also, that are many non-interacting energy components, with a j index. In this case, the first Friedmann equation reads

$$\Omega_k + \sum_j \Omega_j = 1, \tag{2.20}$$

where Ω_k accounts for the geometry of the Universe, i.e.,

$$\Omega_k = -\frac{k}{a^2 H^2}. \tag{2.21}$$

The last information to solve Friedmann equations is to relate the energy densities of the components and the pressure contribution of each component. In this case, the energy conservation equation remains valid for each component separately. The usual approach is to consider a equation of state that relates energy and pressure by

$$w_j = \frac{P_j}{\rho_j}. \tag{2.22}$$

For most proposes, w can be taken as a constant: $w = 1/3$ for radiation, $w = 0$ for non-relativistic matter, and $w = -1$ for dark energy, for instance. The energy conservation for each component will be, thus,

$$\frac{d\rho_j}{dt} + 3\frac{\dot{a}}{a}\rho_j \left(1 + w_j\right) = 0, \tag{2.23}$$

for each j-component. The solution in function of the scale parameter will be, finally,

$$\rho_j = \rho_{jo} \left(\frac{a_o}{a}\right)^{3(1+w_j)}. \tag{2.24}$$

This solution implies that radiation evolves as $\rho \sim a^{-4}$ and radiation as $\rho \sim a^{-3}$ in an expanding, non-interaction components universe. In the next chapter, the dynamics in the Early Universe, where the components interact, will be described.

In the ΛCDM Model, thus, the first Friedmann equation will be written as

$$\Omega_k + \Omega_b + \Omega_{DM} + \Omega_\gamma + \Omega_\Lambda = 1, \tag{2.25}$$

where Ω_b, Ω_{DM}, Ω_γ, and Ω_Λ are the density parameters of baryonic matter, cold dark matter, radiation, and dark energy, respectively. These parameters can be obtained by the measurements of the CMB temperature anisotropies. The current best fit parameters, according to Planck satellite (7), are given in Table 1, where beyond the cited parameters Ω_m is the parameter of the total matter and $h = H/(100\text{km.s}^{-1}.\text{Mpc}^{-1})$ is the normalization of Hubble constant. With the results from Planck, it is possible to test the right abundance of dark matter for a dark matter candidate of a given theory.

Table 1 – Parameters of the ΛCDM Model according to the best-fit results obtained by the Planck satellite.

Parameter	Best fit
$\Omega_b h^2$	0.02237 ± 0.00015
$\Omega_{DM} h^2$	0.1200 ± 0.0012
$\Omega_m h^2$	0.1430 ± 0.0011
Ω_Λ	0.6847 ± 0.0011
$\lvert\Omega_k\rvert$	< 0.05
$H_o\,[\mathrm{km.s^{-1}.Mpc^{-1}}]$	67.36 ± 0.0011

Source: AGHANIM. (7)

ΛCDM Model is, nowadays, the standard cosmological model in the physics community which includes all the considerations stated before. One of its main components, cold dark matter, however, is not consistent with any particle that is present in the Standard Model of Particle Physics. The difficulties of SM particles explaining dark matter are pointed out by several evidences reviewed here, such as the CMB power-spectrum, structure formation, gravitational lensing, and others. This means that contemporary physics lives a duality: SM describes well* particle physics and ΛCDM Model describes well the cosmological observations, but they are not compatible with each other. This incompatibility is used by many physicists as an argument that some new physics, Beyond the Standard Model (BSM), is necessary to extend the SM to explain cosmology.

The next chapter will explain how a new particle can describe dark matter, how it could have been produced in the Early Universe and how it can be detected by astrophysical and other experiments.

* Despite some issues such as neutrino masses, strong CP, and others, it is important to emphasize that particle physics is well-described by the Standard Model.

3 THE PARTICLE DARK MATTER PARADIGM

After discussing the main evidences of the existence of dark matter, it has become clear that it is necessary a new particle, beyond the Standard Model, to explain the paradigm of cold dark matter of cosmology. This new particle must guarantee certain properties such as neutrality, being collisionless, being non-relativistic (cold) and stability at cosmological times. The origin of this particle can be explained by thermal production processes in the Early Universe. Special attention will be given to the WIMPs. In this chapter, some properties of the *particle dark matter* paradigm will be reviewed, such as its production in the Early Universe and its distribution in dark matter halos at galactic scales. Then, the methods of detection of detection will be described, with focus of indirect detection, which is the target of this study.

3.1 Thermal production in the Early Universe

In the late expanding universe, the energy densities of radiation (relativistic) and matter (non-relativistic) states are well-described by the Friedmann equations, which imply, for non-interacting components, that radiation density scales as $\rho \sim a^{-4}$ and matter density $\rho \sim a^{-3}$. That can only be true if the Hubble expansion rate is bigger than the interaction between constituents rate, i.e., $H >> \Gamma_{int}$. That was not true in the Early Universe when the species were produced and therefore the particle interactions must be taken into account. In this epoch, different kinds of reactions were occurring like particle/antiparticle pair production or annihilation, scattering with the photons of the thermal bath, and so on. The regime considered to understand that dynamics is the "thermodynamical equilibrium": as the Universe expands, the temperature drops, but the temperature is always high enough to guarantee that particles continue near the chemical and kinetic equilibrium. That condition breaks as the interaction rate becomes close to the expansion rate, $\Gamma_{int}(T_f) \approx H_f$, and then the particle abundance is just diluted by Hubble expansion. This mechanism, the *freeze-out*, predicts the abundance of dark matter in the cold dark matter paradigm. The foundations of thermodynamics in the Early Universe and the general ideas of the thermal production of dark matter are presented in this section. The discussions and calculations here were based on the books by Kolb & Turner, "The Early Universe" (90), Stefano Profumo's "An Introduction to Particle Dark Matter" (6) and Bauer & Plehn's lecture notes "Yet Another Introduction to Dark Matter The Particle Physics Approach" (91), which are suggested for in-depth studies.

3.1.1 Thermodynamics in the Early Universe

If the species are in kinetic equilibrium with each other, then the phase space functions f, the number n and energy densities ρ will be given by the expressions derived from the statistical quantum mechanics. These quantities, f, n, and ρ are, for fermions (Fermi-Dirac distributions, FD) and for bosons (Bose-Einstein distributions, BE), given by

$$f(\mathbf{p}) = \frac{1}{e^{\frac{E(\mathbf{p})-\mu}{T}} \pm 1}, \quad \text{for fermions (bosons)}, \tag{3.1}$$

$$n = \frac{g}{(2\pi)^3} \int d^3\,\mathbf{p}\, f(\mathbf{p}), \tag{3.2}$$

$$\rho = \frac{g}{(2\pi)^3} \int d^3\,\mathbf{p}\, E(\mathbf{p})\, f(\mathbf{p}), \tag{3.3}$$

where $+(-)$ refers to fermions (bosons), $E(\mathbf{p})$ is the dispersion relation, g is the number of degrees of freedom, and μ is the chemical potential. These relations are valid for each species of particle in thermal equilibrium. Chemical equilibrium means that the chemical potentials in each reaction are balanced. For the purposes here, μ can be taken as zero without greater problems.

Substituting Eq. (3.1) into (3.2) and (3.3) one obtains for n and ρ, in the relativistic limit ($T >> m$),

$$n_R = \begin{cases} \frac{\zeta(3)}{\pi^2} g\, T^3 & \text{(Bose-Einstein)} \\ \frac{3}{4}\frac{\zeta(3)}{\pi^2} g\, T^3 & \text{(Fermi-Dirac)} \end{cases}, \tag{3.4}$$

which can be rewritten in terms of an effective number of degrees of freedom,

$$n_R = \frac{\zeta(3)}{\pi^2} g_{eff}\, T^3, \quad g_{eff}^{\text{BE (FD)}} = 1(3/4)\ , \tag{3.5}$$

$$\rho_R = \begin{cases} \frac{\pi^2}{30} g\, T^4 & \text{(Bose-Einstein)} \\ \frac{7}{8}\frac{\pi^2}{30} g\, T^4 & \text{(Fermi-Dirac)} \end{cases}. \tag{3.6}$$

In the non-relativistic limit ($m >> T$),

$$n_{NR} = g\left(\frac{mT}{2\pi}\right)^{\frac{3}{2}} e^{-\left(\frac{m}{T}\right)}, \quad \rho_{NR} = m\, n_{NR}\ . \tag{3.7}$$

The expressions above show that, at high temperatures, the energy density scales faster for relativistic components than for non-relativistic ones. In other words, in the radiation-dominated universe energy density goes as $\rho \sim T^4$. This dependency will motivate rescale time t (or the a factor) to temperature in the Early Universe. In the approximation of taking into account only relativistic components, the total energy density can be written as

$$\rho_R^{\text{Total}} = \frac{\pi^2}{30} g_*(T)\ T^4. \tag{3.8}$$

In this expression, g_* is the effective number of degrees of freedom weighted over all the relativistic species and T is the temperature of the photon thermal bath. The degrees

of freedom change on temperature since a given i-th species becomes relativistic when $T \gg m_i$, i.e., the mass of each species is a threshold for activating new degrees of freedom. The dependency of g_* for the particles of the Standard Model is shown in Figure 7. The effective number of degrees is thus given by

$$g_* = \sum_{\text{bosons}} g_i \left(\frac{T_i}{T}\right)^4 + \frac{7}{8} \sum_{\text{fermions}} g_i \left(\frac{T_i}{T}\right)^4, \tag{3.9}$$

where 7/8 accounts for Fermi-Dirac statistics, and not all the species are supposed to have the same temperature, i.e., each species has its specific temperature T_i.

In the radiation-dominated era, almost all energy was in relativistic species $\rho^{\text{Total}} \approx \rho_R^{\text{Total}}$, what enables substituting Eq. (3.8) into the Friedmann Equation,

$$H^2 = \frac{8\pi\rho}{3m_{PL}^2} \approx \frac{8\pi^3 g_* T^4}{90 m_{PL}^2}, \tag{3.10}$$

$$H(T) = 1.66\sqrt{g_*(T)}\,\frac{T^2}{m_{PL}}. \tag{3.11}$$

Time can also be rescaled to temperature (90),

$$t = 0.301\, g_*^{-1/2} \frac{m_{PL}}{T^2}. \tag{3.12}$$

These two Equations relate the Hubble rate and time with temperature and now define the temperature of the photon thermal bath T as the parameter of cosmological time in the radiation era. (91)

The thermodynamics expression (3.11) will enable a direct comparison between H and Γ_{int} since both depend on the temperature. This comparison will determine the thermal decoupling of species. The last step that must be taken to simplify thermal production calculations is to rescale the abundance n for a new variable that does not change with Hubble dilution. That will be possible considering the entropy conservation in the Universe.

The entropy density in a homogeneous Universe can be defined as (90)

$$s = \frac{\rho + P}{T}, \tag{3.13}$$

and the total entropy contained in a comoving volume $V = a^3$ as

$$S = sa^3 = \frac{(\rho + P)}{T} a^3. \tag{3.14}$$

It is possible to show that, from Friedman Equations and the first law of thermodynamics, the entropy in the comoving volume is conserved along the Universe expansion (90), i.e., an isentropic expansion,

$$S = s\, a^3 = \text{CONST}. \tag{3.15}$$

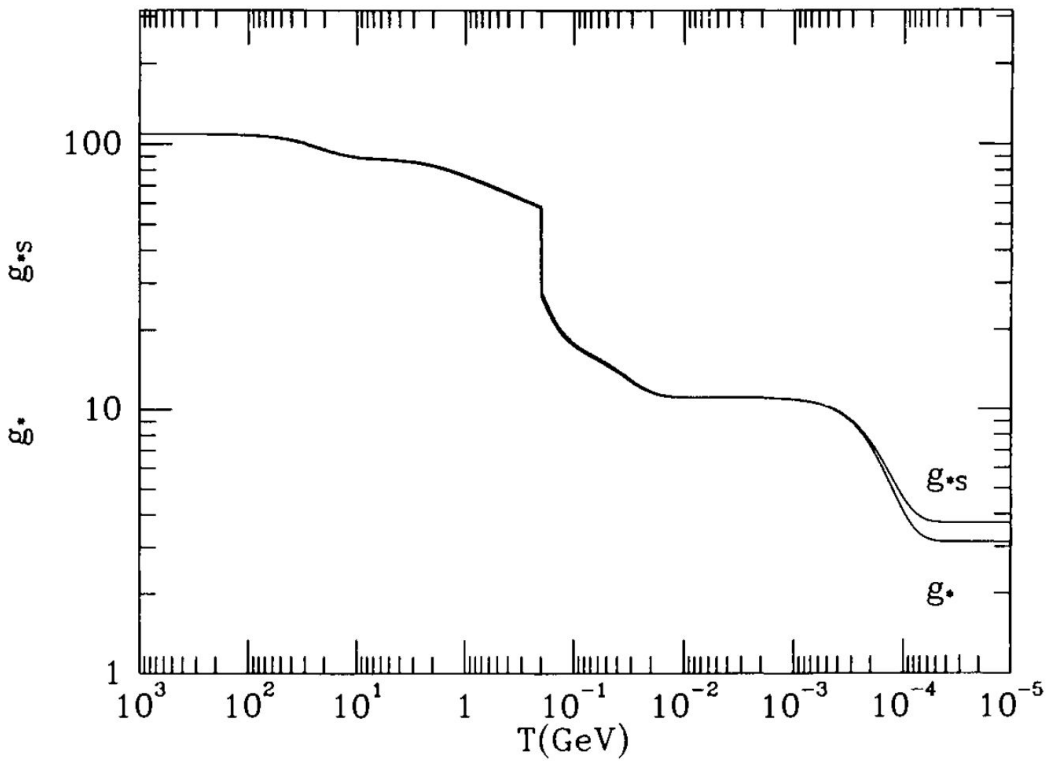

Figure 7 – Number of degrees of freedom for energy g_* and for entropy g_{*S} in function of temperature for the $SU_C(3) \otimes SU_L(2) \otimes U_Y(1)$ Standard Model theory.

Source: KOLB; TURNER. (90)

For the relativistic regime, the entropy density can be written in a very similar way as (3.8) was, considering the degrees of freedom of different species,

$$s = \frac{2\pi^2}{45} g_{*S}(T)\, T^3, \tag{3.16}$$

where

$$g_{*s} = \sum_{\text{bosons}} g_i \left(\frac{T_i}{T}\right)^3 + \frac{7}{8} \sum_{\text{fermions}} g_i \left(\frac{T_i}{T}\right)^3. \tag{3.17}$$

The only differences are the T^3 dependence, instead T^4, and the $(1 + w) = 4/3$ factor that comes from the equation of state of the relativistic gas. The number of degrees of freedom for both energy and entropy is plotted in Figure 7.

With entropy conservation (3.14), s drops as $\sim a^{-3}$, the same as the number density n_i for a decoupled component. The effect of Hubble expansion can then be discounted considering the number of particles in a comoving volume as

$$Y = \frac{n}{s}. \tag{3.18}$$

This quantity is very convenient once the number of particles in the comoving volume is conserved after freeze-out.

This subsection has discussed the equilibrium distributions of species at thermal equilibrium in the Early Universe. Useful relations like the Hubble rate in function of temperature and the entropy conservation were obtained. With these tools, we will be able to determine the abundance of thermal relics.

3.1.2 Boltzmann Equation

The evolution of species abundances is well understood in both Early and Late Universe limits. In the earlier epoch, the species were in thermal equilibrium and their number densities are given by Equations (3.5) and (3.7), which come from Bose-Einstein or Fermi-Dirac distributions. After the decoupling of species, the number of particles in a comoving volume must be conserved and thus $n \sim a^{-3}$. (90) It is in the decoupling epoch where determining species abundances is truly difficult because when $\Gamma_{\text{int}} \approx H$ both particle interactions and the Universe expansion must be taken into account.

To understand what happens during the freeze-out time the usual approach is to analyze the evolution of the distribution function f in the phase space (x^μ, p^μ). This is made through the Boltzmann equation (90),

$$L[f] = C[f], \tag{3.19}$$

where L is the Liouville operator, which encodes the properties of space-time, and C is the collision operator, which determines the interactions of one species with the others.

For the non-relativist limit, the Liouville operator is written as

$$L_{\text{NR}} = \frac{\partial}{\partial t} + \mathbf{v} \cdot \nabla + \frac{d\mathbf{v}}{dt} \cdot \nabla_{\mathbf{v}}, \tag{3.20}$$

where $\mathbf{v} = \mathbf{p}/m$. While the relativistic, covariant definition of the Liouville operator is (90)

$$L_{\text{cov}} = p^\alpha \frac{\partial}{\partial x^\alpha} - \Gamma^\alpha_{\beta\gamma} p^\beta p^\gamma \frac{\partial}{\partial p^\alpha}, \tag{3.21}$$

where p is the 4-momentum and $\Gamma^\alpha_{\beta\gamma}$ stands for the Christoffel symbols.

In the case of a homogeneous and isotropic system, such as our universe, the phase space distribution depends only on energy and time, $f = f(|\mathbf{p}|, t) = f(E, t)$. For the case of the FLRW metric the Liouville operator assumes the form (92)

$$L[f(E,t)] = \frac{\partial f}{\partial t} - \frac{\dot{a}}{a} \frac{|\mathbf{p}|^2}{E} \frac{\partial f}{\partial E}. \tag{3.22}$$

This expression for L can be substituted in Eq. (3.19) to obtain an equation for n,

$$\frac{g}{(2\pi)^3} \int d^3p L[f(E,t)] = \frac{g}{(2\pi)^3} \int d^3p\, C[f(E,t)], \tag{3.23}$$

which, integrating by parts, gives

$$\frac{dn}{dt} + 3Hn = \frac{g}{(2\pi)^3} \int d^3p\, C[f(E,t)]. \tag{3.24}$$

At this point, some assumptions should be made to simplify the collision term on the right-hand side of this equation. In the first place, it will be considered processes of the type $1 + 2 \leftrightarrow 3 + 4$, where 1 and 2 are dark matter particles that annihilate in the 3 and 4 SM particles, like

$$\chi\ \chi' \leftrightarrow SM\ SM, \tag{3.25}$$

for instance. That kind of process was studied in detail by Gondolo & Gelmini in Ref. (92). According to them, some approximations must be made: all the species remain in kinetic equilibrium; the distributions can be approximated to Maxwell-Boltzman, i.e., $f_i \sim e^{E/T}$; the SM particles 3 and 4 are in thermal equilibrium with the thermal bath. After some calculations, the Boltzmann equation assumes the form (93)

$$\frac{dn_1}{dt} + 3Hn_1 = -\left\langle \sigma\, v \right\rangle_{12} n_1 n_2 + \left\langle \sigma\, v \right\rangle_{34} n_3 n_4, \tag{3.26}$$

where $\left\langle \sigma\, v \right\rangle_{ij}$ is the *thermally averaged annihilation cross-section times velocity* for the i and j particles. This expression still can be simplified considering the detailed balance at equilibrium, $\left\langle \sigma\, v \right\rangle_{34} n_3 n_4 \approx \left\langle \sigma\, v \right\rangle_{34} n_3^{eq} n_4^{eq} = \left\langle \sigma\, v \right\rangle_{12} n_1^{eq} n_2^{eq}$. Therefore, the equation becomes

$$\frac{dn_1}{dt} = -3Hn_1 - \left\langle \sigma\, v \right\rangle_{12} \left(n_1 n_2 - n_1^{eq} n_2^{eq}\right). \tag{3.27}$$

If 1 and 2 are identical particles ($n_1 = n_2 = n$), such as Majorana fermions or neutral bosons, thus,

$$\frac{dn}{dt} = -3Hn - \left\langle \sigma\, v \right\rangle \left(n^2 - n^{eq\,2}\right), \tag{3.28}$$

which is the usual form of the Boltzmann equation for thermal relics.

In the expressions above the annihilation rate depends on the thermally averaged annihilation cross-section times velocity, which is defined as

$$\left\langle \sigma\, v \right\rangle = \frac{\int d^3p_1 d^3p_2\, \sigma\, v\, e^{-E_1/T} e^{-E_2/T}}{\int d^3p_1 d^3p_2\, e^{-E_1/T} e^{-E_2/T}}, \tag{3.29}$$

where the cross-section is the cross-section summed over all possible final Standard Model states,

$$\sigma = \sum_f \sigma_{12 \to f}, \tag{3.30}$$

and v is the Møller velocity for the particles 1 and 2, given by

$$v = v_{M\varnothing l}^{12} = \frac{\sqrt{\left(p_1 \cdot p_2\right)^2 - m_1^2 m_2^2}}{E_1 E_2}. \tag{3.31}$$

See that in Eq. (3.28) and in the denominator of (3.29) the number density at equilibrium for a Maxwell Boltzmann distribution is present. It is given by

$$n^{eq}\left(T\right) = \frac{g}{\left(2\pi\right)^3} \int d^3p\, e^{-E/T}, \tag{3.32}$$

which, using the relativistic dispersion relation $E = \sqrt{\mathbf{p}^2 + m^2}$ and $d^3p = 4\pi\sqrt{E^2 - m^2}EdE$, yields

$$n^{eq}(T) = \frac{T}{2\pi^2} g m^2 K_2\left(\frac{m}{T}\right), \tag{3.33}$$

where K_2 is the modified Bessel function of the second kind. This expression can be substituted in the definition of $\langle\sigma\, v\rangle$ (3.29) and a similar integration in the numerator gives

$$\langle\sigma\, v\rangle = \frac{2\pi^2 T \int_{4m}^{\infty} ds\, \sigma(s)\, \sqrt{s}\,(s - 4m^2)\, K_1\left(\frac{\sqrt{s}}{T}\right)}{\left(4\pi m^2 T K_2\left(\frac{m}{T}\right)\right)^2}, \tag{3.34}$$

where K_1 is the modified Bessel function of the first kind, $s = (p_1 + p_2)^2$ is the energy squared of the 1+2 system at the center of mass frame and $\sigma(s)$ is the annihilation cross-section.

In principle, if the dependence of the total annihilation cross-section on s is known, $\langle\sigma\, v\rangle$ can be determined. But in the non-relativistic limit ($x = m/T \gg 1$), it is useful to expand s in terms of the relative velocity v, $s \approx 4m^2 + m^2v^2$ and expand σv in powers of v^2 (92),

$$\langle\sigma\, v\rangle = \left\langle a + bv^2 + cv^4 + ...\right\rangle, \tag{3.35}$$

$$\langle\sigma\, v\rangle = a + \frac{3}{2}bx^{-1} + \frac{15}{8}cx^{-2} + ... \tag{3.36}$$

This series is known as the partial wave expansion and the dominant term depends on the model considered. If a is the dominant term, it is called a s-wave scattering, if b dominates, it is called a p-wave scattering. (93)

The last step to get a convenient form of the Boltzmann equation is to use the number of particles per comoving volume $Y = n/s$. Using Eq. (3.15) one gets

$$\dot{s} = -3Hs \implies \dot{n} + 3Hn = s\dot{Y}. \tag{3.37}$$

Changing the variable n to Y, the Boltzmann equation assumes the form

$$\frac{dY}{dt} = -\langle\sigma\, v\rangle\, s\left(Y^2 - Y_{eq}^2\right), \tag{3.38}$$

which is not useful once it depends on the cosmological time, whereas a function on $x = m/T$ would be preferable. In the new variable,

$$\frac{dY}{dx} = -\frac{\langle\sigma\, v\rangle\, xs}{H(m)}\left(Y^2 - Y_{eq}^2\right), \tag{3.39}$$

where $H(m) \equiv x\frac{dx}{dt}$. For a radiation-dominated Universe, if the number of degrees of freedom is near constant, Eq. (3.11) and (3.12) imply that $H(m) = H(T)\, x^2$. The Boltzmann equation can thus be finally written as

$$\frac{x}{Y_{eq}}\frac{dY}{dx} = -\frac{\Gamma_{eq}}{H}\left[\left(\frac{Y}{Y_{eq}}\right)^2 - 1\right], \tag{3.40}$$

where

$$\Gamma_{eq} = \langle \sigma\, v \rangle\, n_{eq} \tag{3.41}$$

is the interaction rate at equilibrium.

Now that the Boltzmann equation is defined conveniently, the next subsection shows how thermal particle production can explain the observed amount of dark matter in the Universe and how WIMPs appear to be natural candidates for it.

3.1.3 Freeze-out and the WIMP miracle

The Boltzmann equation (3.40) dictates the evolution of the comoving abundance with the temperature decreasing. Solving it analytically is not possible and then it should be done numerically. Even so, its qualitative behavior can be deduced from its format. The rate Γ_{eq}/H represents the χ annihilation and determines that Y is not so far the equilibrium values Y_{eq}, if $\Gamma/H >> 1$. In the relativistic limit ($x << 3$) (90), $n_{eq} \sim T^3$ and the annihilation rate usually will also depend on temperature through a power-law, $\Gamma_{eq} \sim T^{\alpha}$, while in the non-relativistic limit the interaction rate is suppressed by the Boltzmann factor, $\Gamma \sim \exp(-x)$. As temperature decreases, H becomes dominant and annihilation is not efficient enough to maintain Y close to Y_{eq}. At this point, when $\Gamma_{eq} \approx H$, the species could no more be in equilibrium and Y *freezes-out*. Thus, in resume, $Y(x) \approx Y_{eq}(x)$, for $x < x_f$ and $Y(x) \approx Y_f = Y(x_f)$, for $x > x_f$, where x_f corresponds to the temperature when freeze-out happens. If the particle was relativist at freeze-out, it is called a *hot thermal relic*. That is the case of the neutrinos, for instance. However, we know that dark matter cannot be composed by hot relics, instead it should be a *cold thermal relic*, i.e., it was already non-relativistic at freeze-out. In the following, let us analyze the determination of the abundance of a cold relic such as dark matter.

The exact solution of the Boltzmann equation must be obtained with numerical methods. Nevertheless, obtaining an approximate solution that gives us some insights about the abundance of cold relics is still possible. The next steps were based on the discussion contained in Ref. (90).

In the first place, when the species is already non-relativistic, its annihilation-cross section depends on a power law of the dominant term of the expansion (3.36),

$$\langle \sigma\, v \rangle = \sigma_o x^{-n}, \tag{3.42}$$

and the equilibrium abundance is given by

$$Y_{eq} = 0.145\,(g/g_{*S})\, x^{3/2} e^{-x}. \tag{3.43}$$

With this, Eq. (3.39) can be rewritten as

$$\frac{dY}{dx} = -\frac{\lambda}{x^{n+2}} \left(Y^2 - Y_{eq}^2\right), \tag{3.44}$$

where λ is the annihilation term at zero order and is defined by

$$\lambda = \left[\frac{\langle\sigma\, v\rangle\, xs}{H\,(m)}\right]_{x=1} = 0.264\left(g_{*S}/g_*^{1/2}\right) m_{PL} m \sigma_o. \tag{3.45}$$

Eq. (3.44) can be approximately solved considering the difference between the abundance yield and the abundance yield at equilibrium $\Delta = Y - Y_{eq}$. The Boltzmann equation now reads

$$\Delta' = -Y'_{eq} - \lambda x^{-(n+2)} \Delta\left(2Y_{eq} + \Delta\right), \tag{3.46}$$

whose approximate solutions are

$$\begin{array}{lll} \Delta & \approx & \frac{x^{n+2}}{2\lambda} \quad , 3 < x << x_f, \\ \Delta_\infty & \approx & \frac{n+1}{\lambda} x_f^{n+1} \quad , x_f << x. \end{array} \tag{3.47}$$

For $x >> x_f$ Boltzmann attenuation makes $Y_{eq} \to 0$ and thus today abundance is the one at freeze-out, $Y_\infty \approx \Delta_\infty$. Substituting the definition of λ and $\langle\sigma\, v\rangle$, the actual cold relic abundance is given by (90)

$$Y_\infty = \frac{3.79\,(n+1)\, x_f^{n+1}}{\left(g_{*S}/g_*^{1/2}\right) m_{PL} m \sigma_o} = \frac{3.79\,(n+1)\, x_f}{\left(g_{*S}/g_*^{1/2}\right) m_{PL} m \,\langle\sigma\, v\rangle}, \tag{3.48}$$

which is the expression that relates the parameters of the cold relic particle, its mass m, and the annihilation cross-section $\langle\sigma\, v\rangle$, with the abundance from thermal production.

See that the abundance expression in Eq. (3.48) depends on the time of freeze-out, x_f, which is a model-dependent parameter. It can be determined by some numerical criterion, usually $\Delta\,(x_f) = \delta Y_{eq}\,(x_f)$, (90) where δ is a number near the unity. Let us consider here a heavy (m in the GeV-TeV range) particle with a cross-section in the order of the weak scale, $\langle\sigma\, v\rangle \sim G_F^2 m^2$, where G_F is the Fermi constant. This kind of hypothetical particle is known as a *Weakly Interacting Massive Particle* (WIMP). For WIMPs, the annihilation cross-section will be, thus (6)

$$\langle\sigma\, v\rangle \sim G_F^2 m^2 \sim 10^{-10}\left(\frac{m}{\mathrm{GeV}}\right)^2 \mathrm{GeV}^{-2} \sim 10^{-27}\left(\frac{m}{\mathrm{GeV}}\right)^2 \mathrm{cm}^3\mathrm{s}^{-1}. \tag{3.49}$$

Using values of mass and cross-section at these orders gives a freeze-out time x_f in the range $20 - 50$. See Refs. (6) and (91) for a detailed discussion.

Now that the typical values of m, $\langle\sigma\, v\rangle$, and x_f for the WIMP paradigm are known, one can estimate the abundance of a WIMP cold relic nowadays Ω_o as (90)

$$\Omega_o = \frac{m s_o Y_o}{\rho_c} \implies \Omega_o h^2 \approx 10^9 \frac{(n+1)\, x_f}{\left(g_{*S}/g_*^{1/2}\right) m_{PL}\,\langle\sigma\, v\rangle}\,\mathrm{GeV}^{-1}, \tag{3.50}$$

which, considering the typical parameters of a WIMP, gives

$$\Omega_o h^2 \approx 0.1 \quad \frac{10^{-26}\,\mathrm{cm}^3/\mathrm{s}}{\langle\sigma\, v\rangle}. \tag{3.51}$$

Substituting the WIMP mass value as some GeV in Eq. (3.49) yields the exact observed abundance of dark matter in the Universe, $\Omega_o h^2 \approx 0.1$. This astonishing result that massive particles with interactions on the weak scale provide the correct amount of dark matter that we observe is known as the *WIMP miracle*. Further stipulations show that the typical value of the thermal annihilation cross-section of WIMP must be $\langle \sigma\, v \rangle = 3 \times 10^{-26}\,\mathrm{cm^3 s^{-1}}$ to provide the right abundance of dark matter. Figure 8 shows the curves of abundance as a function of x and the freeze-out mechanism, for different values of mass and annihilation cross-section in the WIMP scale.

The WIMP miracle is one of the best evidences that thermal relic production could explain dark matter. Other classes of models can explain the observed amount of dark matter in the Universe, with different masses or cross-sections than those of WIMPs, but the WIMP paradigm is still one of the best and simplest classes of models for dark matter. For that reason, the focus of this work will be the WIMPs.

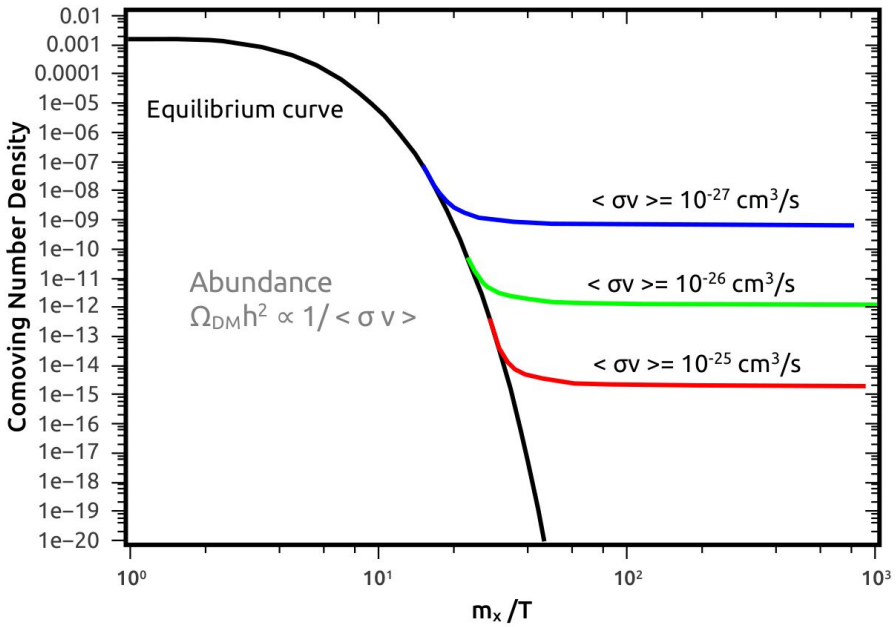

Figure 8 – Representation of the evolution of abundance per comoving volume Y in function of the time parameter $x = m/T$. The black curve represents the equilibrium curve $Y = Y_{eq}$ and the other curves correspond to the freeze-out for annihilation cross-section $\langle \sigma v \rangle = 10^{-27}$(blue), 10^{-26} (green), 10^{-25} (red) $\mathrm{cm^3\ s^{-1}}$.

Source: ARCADI *et al.* (94)

3.1.4 Co-annihilation

There are some exceptions to the abundance evaluations that were presented in the previous subsection. Three important cases that modify the standard calculation of thermal production were discussed in a paper by Griest and Seckel (95), among them the so-called co-annihilation regime. This case goes as follows. Consider a new sector, usually

called the dark sector, beyond the Standard Model of Particle Physics. These particles are characterized by some new quantum number, associated with a new symmetry, for instance. There will be then particles with masses $m_1, m_2, m_3, ..., N$ for a total of N new particles. Supposing no identical masses and an extra symmetry, the lightest particle among them will be stable and thus is a viable dark matter particle. Let us consider that there are just two new particles χ_1 and χ_2 with $m_1 < m_2$. The possible processes that produce SM particles are

$$\begin{aligned} \chi_1\chi_1 &\leftrightarrow SMSM \\ \chi_1\chi_2 &\leftrightarrow SMSM \\ \chi_2\chi_2 &\leftrightarrow SMSM. \end{aligned} \tag{3.52}$$

The first process is the ordinary annihilation, and the second and third are known as *co-annihilation processes* where a different, more massive, particle is on the left side of the reaction. The (co-) annihilation cross-section is defined as a sum over the final SM states f,

$$\sigma_{ij} = \sum_f \sigma_{ij\to f}. \tag{3.53}$$

As the co-annihilating particles are unstable, they will eventually decay into the lightest new particle. The (inverse) decay processes read

$$\chi_i \leftrightarrow \chi_j SMSM \tag{3.54}$$

These processes have a associated decay width, which is also given by the sum over the final states (96),

$$\Gamma_{ij} = \sum_f \Gamma_{i\to jf}. \tag{3.55}$$

The key condition of the co-annihilation regime is that the mass and co-annihilation cross-section of the partner particles are very close to the mass and annihilation cross-section of the lightest particle (let us call it χ_1). In this case, the abundances of all the beyond SM particles will evolve according to the Boltzmann equation and freeze-out nearly at the same time, with similar frozen-out abundances. The co-annihilating particles will then eventually decay into χ_1 efficiently *after freeze-out*. This means that if χ_1 is the dark matter particle, a suppressed dark matter abundance produced by an annihilation cross-section larger than the usual will be enhanced by the co-annihilating particles that will decay into the dark matter particle. So, at the end of the day, the final effect of co-annihilation for dark matter models is to *enhance the dark matter annihilation cross-section for the same relic abundance.*

Let us see in further detail how the co-annihilation regime works. Considering the cited processes, the Boltzmann equation for each i species will be (95)

$$\frac{dn_i}{dt} = -3Hn_i - \sum_j \langle \sigma_{ij}\, v_{ij} \rangle \left(n_i n_j - n_i^{eq} n_j^{eq} \right) - \sum_{j\neq i} \Gamma_{ij} \left(n_i - n_i^{eq} \right), \tag{3.56}$$

where $\langle \sigma_{ij}\, v_{ij} \rangle$ is the thermally averaged (co-)annihilation cross-section, defined analogously to Eq. (3.29) with the correspondent v_{ij} Møller velocity, as displayed in Eq. (3.31), n_i is the number density of the i-th particle and n_i its equilibrium value. However, since the unstable particles will decay into χ_1 just after the freeze-out, the relevant quantities for a cold relic abundance are the total number density and the equilibrium total number density, defined as (96)

$$n = \textstyle\sum_i n_i, \quad n^{eq} = \sum_i n_i^{eq}. \tag{3.57}$$

Thus, the Boltzmann equation for the total density is

$$\frac{dn}{dt} = -3Hn - \sum_{i,j} \langle \sigma_{ij}\, v_{ij} \rangle \left(n_i n_j - n_i^{eq} n_j^{eq} \right), \tag{3.58}$$

since decay conserves the total number of particles. The last step is to simplify the second term on the left side of the equation to use just n and n^{eq} as parameters.

Before freeze-out, (co-)annihilation is very efficient, which means that all n_i abundances are very close to equilibrium, and so is the ratio between abundances (95),

$$\frac{n_i}{n} \approx \frac{n_i^{eq}}{n^{eq}}, \tag{3.59}$$

which is a very reasonable approximation. With this, the Boltzmann equation comes back to a familiar format,

$$\frac{dn}{dt} = -3Hn - \langle \sigma_{\text{eff}}\, v \rangle \left(n^2 - n_{eq}^2 \right), \tag{3.60}$$

where the effective annihilation cross-section is defined as

$$\langle \sigma_{\text{eff}}\, v \rangle = \sum_{ij} \langle \sigma_{ij} v_{ij} \rangle \frac{n_i^{eq} n_j^{eq}}{n^{eq2}}, \tag{3.61}$$

which is an average over the (co-)annihilation cross-section weighted over the equilibrium abundances. These are given by the same expression in Eq. (3.33),

$$n_i^{eq}(T) = \tfrac{T}{2\pi^2} g_i m_i^2 K_2 \left(\tfrac{m_i}{T} \right), \quad n^{eq}(T) = \tfrac{T}{2\pi^2} \textstyle\sum_i g_i m_i^2 K_2 \left(\tfrac{m_i}{T} \right). \tag{3.62}$$

Thus, knowing the annihilation and co-annihilation cross-sections σ_{ij} and substituting the densities of Eq. (3.62) into Eq. (3.61) enables obtaining the effective annihilation cross-section in the co-annihilation regime.

The precise calculation of the effective cross-section through the expression of Eq. (3.61) and the thermal averaging in it can be tough. For that reason, Edsjo and Gondolo obtained a routine (96) for this evaluation using the neutralino as an example. This work is suggested for further details since it is not the focus of this work. Nevertheless, it is still interesting to obtain the effective cross-section (not the thermally averaged) in the non-relativistic limit. In this case, n_i^{eq} follows the expression $\sim g_i m^{3/2} \exp(-m/T)$ of Eq. (3.7) and the effective annihilation cross-section becomes (95)

$$\sigma_{\text{eff}} = \sum_{ij} \sigma_{ij} \frac{g_i g_j}{g_{\text{eff}}^2} \left(1 + \frac{\Delta m_i}{m_1} \right)^{3/2} \left(1 + \frac{\Delta m_j}{m_1} \right)^{3/2} e^{-\frac{\Delta m_i + \Delta m_j}{T}}, \tag{3.63}$$

where $\Delta m_i = m_i - m_1$ is the mass-splitting between the i-th particle and the stable dark matter particle 1 and the effective number of degrees of freedom is

$$g_{\text{eff}} = \sum_i g_i \left(1 + \frac{\Delta m_i}{m_1}\right)^{3/2} e^{-\frac{\Delta m_i}{T}}. \tag{3.64}$$

The effective cross-section for the co-annihilation regime defined in Eq. (3.63) can be then substituted into Eq. (3.29) and the effective thermally averaged cross-section $\langle \sigma_{eff}\, v \rangle$ that is in the Boltzmann equation (3.60) determined.

Evaluating in detail the solution of the Boltzmann equation for the co-annihilation regime is not in the scope of this work. This task will be done with the help of consolidated numerical programs in chapter 6. However, some insights can be obtained from Eq. (3.63). In the first place, for co-annihilation to be important, the mass-splittings of the particles must be $\Delta m_i/m_1 < 10\%$ due to the Boltzmann suppression factor $\exp(\Delta m_i/T)$. Another feature is that σ_{eff} will change according to x, so for the present time $T \to 0$ implies $\sigma_{eff} \to \sigma_{11}$, which is the self-annihilation cross-section today, while at x_f, when abundance froze-out, the co-annihilation processes can change $\sigma_{eff} \neq \sigma_{11}$. This means that, for a dark matter model with co-annihilation, the current annihilation cross-section can be higher than $3 \times 10^{-26}\,\text{cm}^3\text{s}^{-1}$ because what sets the relic abundance is $\langle \sigma_{eff} v \rangle$ at x_f, not today.

Now that the main aspects of thermal cold relics have been discussed, that is, how cold dark matter can be produced, the next section discusses how it is distributed in astrophysical objects of the present universe.

3.2 Dark matter halo models

The particle dark matter paradigm not only can explain the observed amount of dark matter in the Universe but can also help us understand how it is distributed in galactic scales. The galaxy rotation curves data suggest that dark matter should be distributed in the galaxies following a $\sim 1/r^2$ to produce flat rotation curves. (53) Using the Boltzmann equation in the non-relativistic limit (3.20), one gets

$$\frac{\partial f}{\partial t} + \mathbf{v} \cdot \nabla f + \frac{d\mathbf{v}}{dt} \cdot \nabla_{\mathbf{v}} f = 0, \tag{3.65}$$

where the annihilation effect is neglected. According to Jeans' theorem (see Lisanti's 2017 lectures notes (93) for further details), the solution, will be, for an isotropic and equilibrium distribution,

$$f(\mathbf{r}, \mathbf{v}) \sim e^{m\epsilon/KT}, \quad \text{where}\, \epsilon = \tfrac{v^2}{2} - \Phi, \tag{3.66}$$

Φ is the Newtonian gravitational potential, m is the particle mass, K is the Boltzmann constant and T is the equilibrium temperature. Using that the density is proportional to the phase space function integrated over the velocity space, one gets the relation

$$\rho \sim e^{\Phi/\sigma^2}. \tag{3.67}$$

This relation, in turn, can be substituted into the Poisson Equation making $\Phi \sim \ln(\rho)$, therefore

$$\nabla^2\phi = -4\pi G\rho \implies \rho = \frac{\sigma^2}{2\pi G r^2}, \tag{3.68}$$

i.e., $\sim 1/r^2$, just as indicated by galaxy rotation curves. This profile is usually known as the isothermal profile.

Despite this interesting result, the isothermal profile model is not realistic. (9) In the last decades, several models of dark matter distribution in galactic scales have been proposed. Some of them are obtained from N-body simulations, which usually provide a power-law $\sim 1/r^\gamma$, $\gamma > 0$, profile to inner regions of the halo, the reason they are called "peaked profiles" or "cuspy profiles". This slop increases considerably the dark matter density near the center. Other profiles, called cored profiles, are characterized by being flat near the halo center and describe better the galactic rotation data of some dwarf galaxies. (84) In this case the dark matter density must tend to a constant value in the center.

Numerical N-body simulations have been made since the first work by Navarro, Frenk, and White (NFW) (97), where they found a profile that goes to $\sim 1/r$ for the inner region ($r << r_s$) of galaxies and $\sim 1/r^3$ in the outer regions. For many models, the halo profile can be parameterized as

$$\rho(r) = \frac{\rho_s}{(r/r_s)^\gamma \left[1 + (r/r_s)^\alpha\right]^{(\beta-\gamma)/\alpha}}, \tag{3.69}$$

where $(\alpha, \beta, \gamma) = (1,3,1)$ in the case of the NFW profile. After this initial work, other groups made similar simulations and found different parameters for the same parameterization. For instance, Moore *et al.* (98) have found an even steeper profile at inner regions $(\alpha, \beta, \gamma) = (1, 3, 1.16)$. More recent simulations were fitted by a continuously-varying slope profile called Einasto, where $d\ln\rho/d\ln r = -2(r/r_s)^{\alpha_E}$. On the other hand, among the examples of cored profiles, we can cite the (modified) isothermal (99) (100) or the Burket profile. (101) The expressions for all these profiles (9) are given bellow (9):

$$\begin{aligned}
&\text{NFW:} && \rho_{\text{NFW}}(r) = \frac{\rho_s r_s}{r\left(1+\frac{r}{r_s}\right)^2} \\
&\text{Einasto:} && \rho_{\text{Ein}}(r) = \rho_s \exp\left(-\frac{2}{\alpha_E}\left[\left(\frac{r}{r_s}\right)^{\alpha_E} - 1\right]\right) \\
&\text{Isothermal:} && \rho_{\text{Iso}}(r) = \frac{\rho_s}{1+(r/r_s)^2} \\
&\text{Burket:} && \rho_{\text{Bur}}(r) = \frac{\rho_s}{(1+r/r_s)\left(1+(r/r_s)^2\right)} \\
&\text{Moore:} && \rho_{\text{Moo}}(r) = \rho_s \left(\frac{r_s}{r}\right)^{1.16} \left(1 + \frac{r}{r_s}\right)^{-1.84}
\end{aligned} \tag{3.70}$$

All these models have two parameters, r_s and ρ_s (and α_E, for Einasto), that usually give the scales of radius and density for the halo, respectively. In the case of the Milky Way, these variables must be fitted according to two astrophysical constraints (9):

- The dark matter density at the Solar vicinity $r_\odot = 8.33\,\mathrm{kpc}$ (102) that is around $\rho_\odot = \rho\,(r_\odot) \approx 0.3\,\mathrm{GeVcm^{-3}}$. (9) However, that estimation could vary a lot due to errors of the same magnitude, as recent studies that point to higher values in the range $0.3-0.6\,\mathrm{GeVcm^{-3}}$. In this work we use the updated value $\rho_\odot = 0.39\,\mathrm{GeVcm^{-3}}$. (103)
- The mass inside the 60 kpc radius in the Milky Way as $M_{60} = 4.7 \times 10^{11}\,M_\odot$. This value was obtained on the recent surveys of stars by the SDSS Collaboration. (104)

The parameters ρ_s and r_s (and α_E for Einasto) that fill the requirements above for the cited profiles are specified in Table 2. All these parameterizations were extracted from PPPC 4 DM ID (9), except Einasto, where the profile used by the CTA collaboration is considered (8). The profiles are plotted in Figure 9, where it is possible to see the big variability of predicted dark matter density from different profile models. This difference is clearer when comparing cored profiles, favored by galactic rotation data of some dwarf galaxies, (84) and cuspy profiles, favored by N-body simulations. This tension is known as the core-cuspy problem and is one of the biggest problems of dark matter science. (53) This controversy has led to different attempts at solutions, like considering warm dark matter or supposing Self-Interacting Dark Matter (SIDM), among others. (53) In the case of the Milky Way, estimating the dark matter density in the inner part of the galaxy is very difficult because the galactic bulge is baryonic dominated, leading to high uncertainties (105). This model dependency makes it inefficient to compare all possible halo models. The usual approach in dark matter indirect searches (see 3.4) is to choose one dark matter profile and compare the limits from different observatories with the same model. Sometimes the cored and cuspy profiles are used as two extreme limits.

Table 2 – List of parameters (r_s, ρ_s, α_E) that fit the Milky Way data according to different halo models (Eq. (3.70)). Except for the Einasto model, which was extracted from CTA analysis (8), the parameters' values were obtained from PPPC 4 DM IDM (9).

Dark matter profile	r_s [kpc]	ρ_s [GeV/cm^3]	α_E
NFW	24.42	0.184	-
Einasto	20	0.081	0.17
Isothermal	4.38	1.387	-
Burket	12.67	0.712	-
Moore	30.28	0.105	-

Source: CIRELLI *et al.* (9); CHERENKOV TELESCOPE ARRAY. (8)

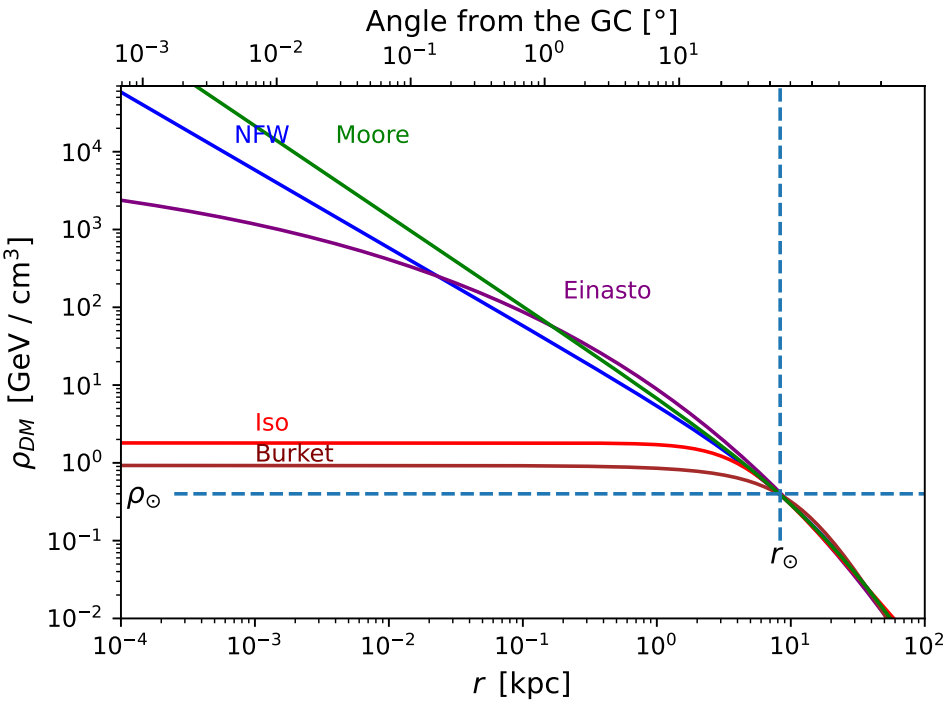

Figure 9 – Dark matter density versus distance from the Galactic Center for the Milky Way halo according to the profile models of Table 2.

Source: Adapted from CIRELLI *et al.* (9)

Now that the thermal production of dark matter and its distribution in halos have been discussed, the following section will address the promising methods that can detect the dark matter particle. The discussion of density profile models will be especially important to the indirect dark matter searches.

3.3 Dark matter detection methods

In the particle dark matter paradigm, it is expected that these particles should have some coupling to the Standard Model. This coupling enables the detection of the dark matter particle by three main methods of search: colliders, direct detection and indirect detection. These processes are represented in Figure 10, where the incoming and outgoing particles can be dark matter particles (DM) or Standard Model particles (SM) and the box in black represents some beyond SM physics process that is not known nowadays. (94)

In colliders, dark matter particles can be created by the collision of two SM particles. Since these particles interact very little, they can only be detected by the missing transverse energy. In direct detection searches, the dark matter particles that travel in the dark matter halo in Earth's vicinity are expected to scatter with SM particles. This can be detected by measuring the recoil energy of atomic nuclei (or even electrons) in a target. Indirect detection, by turn, consists of searching for some excess of SM particles

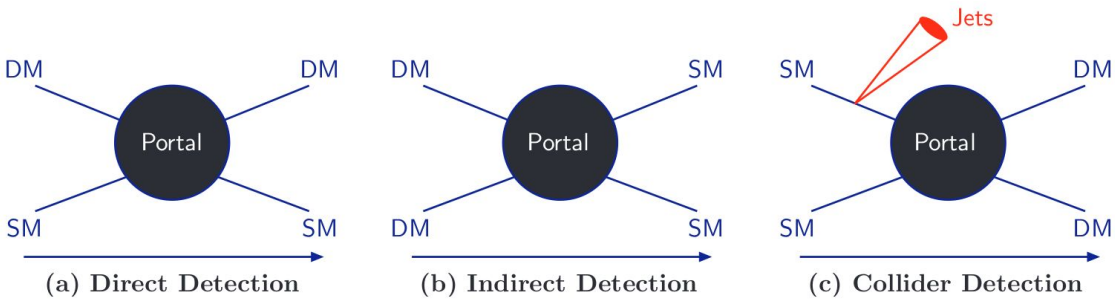

Figure 10 – Diagrams that represent the possible channels of dark matter detection: (a) direct detection, (b) indirect detection and (c) collider detection. The right arrow indicates the time direction.

Source: ARCADI *et al.* (94)

produced in the dark matter self-annihilation or decay in astrophysical objects. Let us discuss in further detail these three methods.

3.3.1 Colliders

Dark matter particles such as WIMPs can be produced in particle colliders, such as the LHC, if the necessary energy is supplied. If these particles are weakly interacting, electrically neutral, and stable at cosmological time, they can be searched by some amount of *missing transverse energy* after collision. (106) That is, colliders cannot 'see' dark matter particles, but it is possible to infer the existence of missing particles by analyzing the expected signal from the SM counterpart, such as jets or charged leptons. Colliders have the advantage of being very controlled experiments but have some disadvantages: they can only produce particles with the mass in the energy range of the experiment (the center of mass energy) and they cannot distinguish a dark matter particle from any other particle that has a decay time sufficient for survival within the collider. Confirmation of a truly dark matter signal relies on direct or indirect detection methods, (106) which will be discussed next.

3.3.2 Direct detection

Another method for searching WIMP dark matter particles is direct detection. It is expected that dark matter particles traveling around in the dark matter halo will

pass through the Earth and, with some probability, interact with matter. Putting an underground detector, with some inert material, a dark matter particle can scatter off an atomic nucleus of the target material and its recoil energy E_R can be in principle measured. (107)

Supposing that the nucleus is at rest in the laboratory frame, the squared transferred momentum to the nucleus by the dark matter particle will be

$$q^2 = 2\mu^2 v^2 \left(1 - \cos\theta\right), \tag{3.71}$$

where v is the velocity of the dark matter particle (typically $v \approx 10^{-3}c$), θ is the scattering angle, and $\mu \equiv m_N m_{DM} / \left(m_N + m_{DM}\right)$ is the reduced mass of the nucleus-dark matter particle system. The recoil energy then, by its turn, is given by

$$E_R = \frac{q^2}{2m_N} = \frac{\mu^2 v^2}{m_N} \left(1 - \cos\theta\right), \tag{3.72}$$

where m_N is the mass of the target nucleus and m_{DM} is the dark matter particle mass.

Beyond the kinematic relations above, it is necessary to relate the rate of scattering events with the dark matter observables. The differential rate of events per target mass and per time (usually in $\text{keV}^{-1}.\text{kg}^{-1}.\text{day}^{-1}$ units) is (93)

$$\frac{dR}{dE_R} = \frac{N_t\, \rho_{DM}}{m_{DM}} \left\langle \frac{d\sigma_{DM-N}}{dE_R}\, v \right\rangle, \tag{3.73}$$

where N_t is the number of target nuclei per material mass, ρ_{DM} is the dark matter energy density, $\frac{d\sigma_{DM-N}}{dE_R}$ is the differential nucleus-dark matter particle scattering cross-section, and v is the velocity of the dark matter particle in the laboratory frame. The brackets represent the average over the dark matter velocities distribution and it can be written as

$$\frac{dR}{dE_R} = \frac{N_t\, \rho_{DM}}{m_{DM}} \int_{v_{\min}}^{v_{\max}} f\left(v\right) \frac{d\sigma_{DM-N}}{dE_R}\, v\, d^3 v, \tag{3.74}$$

where $f\left(v\right)$ is the velocity distribution (usually a Maxwell-Boltzmann distribution is considered), $v_{\max}$ is the escape velocity in the Milky Way (around $\sim 500 - 600$ km/s (108)), and $v_{\min}$ is the minimal velocity kinetically allowed for a given recoil energy E_R,

$$v_{\min} = \sqrt{\frac{E_R m_N}{2\mu^2}}. \tag{3.75}$$

The WIMP-nucleus differential cross-section can be separated into a spin-independent (SI) and a spin-dependent (SD) component (84) as

$$\frac{d\sigma_{DM-N}}{dE_R} = \left(\frac{d\sigma_{DM-N}}{dE_R}\right)_{SI} + \left(\frac{d\sigma_{DM-N}}{dE_R}\right)_{SD}, \tag{3.76}$$

where spin-dependent and spin-independent terms depend on the nuclear wave functions, what is usually encoded by the form factors $F_{SI}\left(E_R\right)$ and $F_{SD}\left(E_R\right)$. The total cross-section can then be rewritten as

$$\frac{d\sigma_{DM-N}}{dE_R} = \frac{m_N}{2\mu^2 v^2} \left(\sigma_o^{SI} F_{SI}^2\left(E_R\right) + \sigma_o^{SD} F_{SD}^2\left(E_R\right)\right). \tag{3.77}$$

The form factors and the cross-section amplitudes σ_o^{SI} (spin-independent) and σ_o^{SD} (spin-dependent) can be derived from the interaction Lagrangian between the dark matter particle and the quarks inside the nucleons. For that reason, the WIMP-nucleon cross-section will depend on the dark matter model. Some examples of these calculations are reviewed in some detail in Bertone's 2010 book (84).

Figure 11 shows the upper limits on the total SI WIMP-nucleon cross-section σ_{DM-N} from different direct detection experiments, particularly the limits from the XENONnT experiment, the most restrictive among direct detection experiments. In panel (a), it is shown that direct detection experiments are going to become sensitive to detect scattering from neutrinos, the *neutrino floor*, which represents a lower limit in the sensitivity of direct detection experiments. (111)

3.3.3 Indirect detection

Since dark matter dominates gravitationally the Universe in galactic scales, its density must be very high in many astrophysical environments, such as the Milky Way Galactic Center (GC), dwarf spheroidal galaxies (dSph), galaxy clusters, and satellite galaxies of the Milky Way. In self-annihilating dark matter models, such astrophysical objects can provide high fluxes of particles. If dark matter particles annihilate, they can produce pairs of SM particle/antiparticles such as pairs of gauge bosons (W^+W^-, ZZ, ...), quarks/antiquarks ($c\bar{c}$, $b\bar{b}$,...), leptons/antileptons (e^+e^-, $\mu^+\mu^-$,...) and so on. Some of these particles are unstable and will suffer the process of hadronization or decay producing stable SM particles that can propagate through space. These particles can be charged particles, as e^+e^- or $p\overline{p}$, or neutral messengers like neutrinos ν or gamma rays γ and even deuterium $d\overline{d}$. (9) Despite not being the focus of this work, analogous processes occur for decaying dark matter. The processes of dark matter annihilation (or decay) into primary channels and the subsequently decaying and hadronization to stable particles are very well described by Cirelli *et al.* in the PPPC 4 DM ID (9) and represented here in Figure 12. This technique is particularly interesting because in many models dark matter has a mass that lies in the (multi)-TeV range, an energy scale that is not yet accessible in collider experiments on Earth.

Detecting an excess of these particles could characterize a discovery of dark matter annihilation in the Universe, allowing us to probe two important properties of the dark matter particle: its mass m_{DM} and the thermally averaged annihilation cross-section $\langle \sigma\, v \rangle$. This kind of excess can be classified into three types (9): cosmic-rays (charged particles), neutrinos, and gamma rays. Charged cosmic rays like protons, nuclei, electrons and positrons are strongly affected by propagation effects, especially deflection, diffusion by galactic, extragalactic magnetic fields, and loss processes. (112) These phenomena produce a loss of directionality and energy making the analysis more difficult. However, an

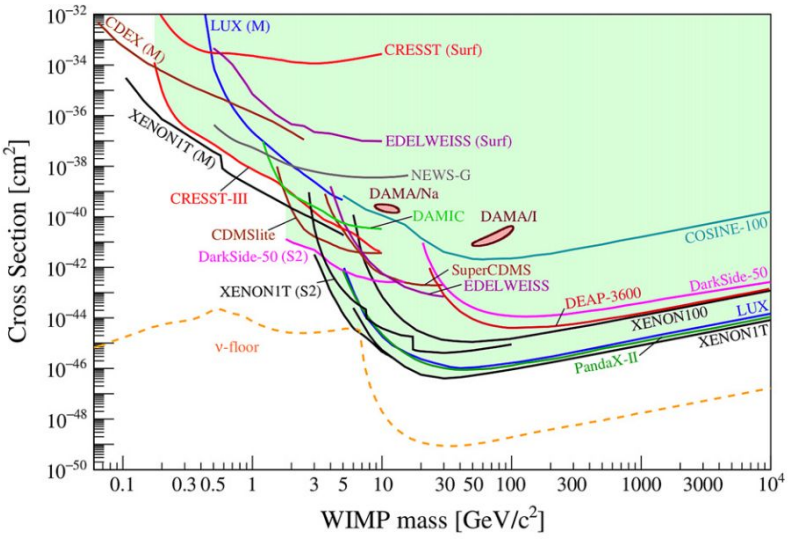

(a) Compilation of limits for the SI WIMP-proton cross-section from different experiments.

Source: BILLARD. *et al.* (109)

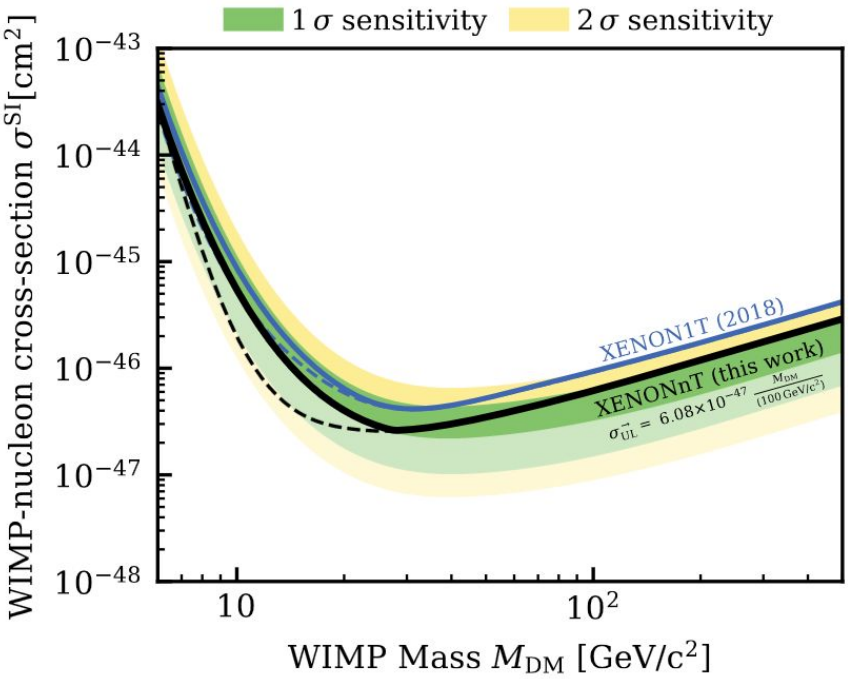

(b) Limits for the SI WIMP-nucleon cross-section from the XENONnT results.

Source: APRILE *et al.* (110)

Figure 11 – Upper limits at 90 % of confidence level on the SI WIMP-nucleon cross-section σ_{DM-N} in function of the dark matter mass m_{DM} for (a) a compilation of different experiments and for (b) the recent results obtained from XENONnT.

excess of these particles and their energy spectral signatures can be searched by experiments such as the AMS-02 mission in the International Space Station. (113) Gamma rays and neutrinos, on the other hand, do not suffer directional effects. Nevertheless, neutrinos

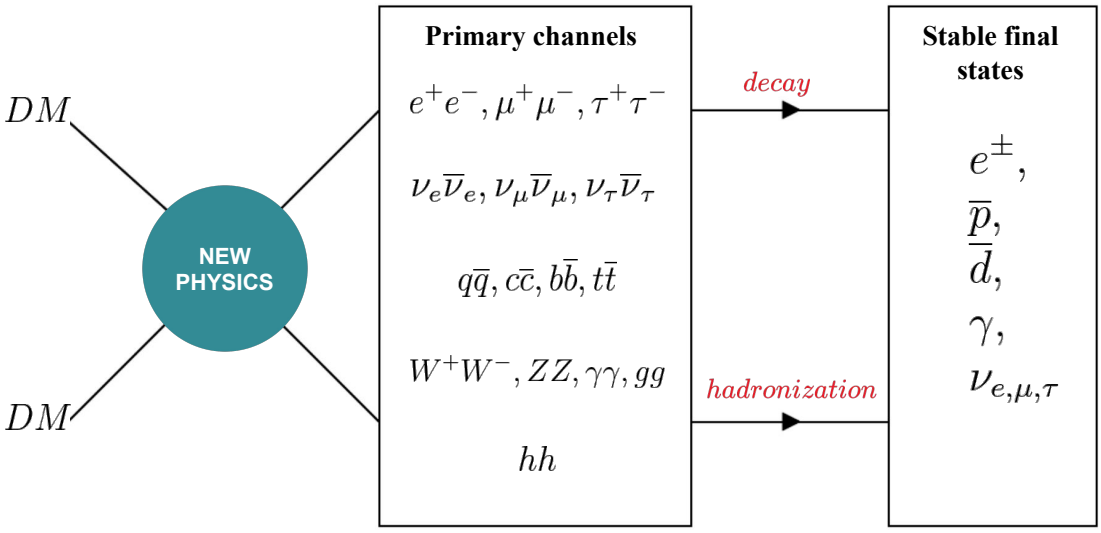

Figure 12 – Diagram of dark matter annihilation through primary channels and subsequently hadronization or decay, producing stable SM particles, also known as final states. The processes are similar to dark matter decay.

Source: By the author.

are very hard to detect and thus the limits from neutrino detectors such as ICE-CUBE and ANTARES are comparatively weaker than the ones from gamma rays (114). GeV-TeV gamma rays are attenuated by pair production in interaction with the CMB and the extragalactic background light (EBL) but with a mean-free path much greater than galactic dimensions. The comparison of limits from positrons, neutrinos, and gamma rays is represented in Figure 13.

With all these considerations, we see that gamma rays are the ideal cosmic messengers to detect dark matter annihilation in the Universe, and for that reason, it will be the channel of search in this work. The gamma-ray signal from dark matter annihilation and the way that dark matter observables $\langle \sigma\, v \rangle$ and m_{DM} can be probed will be discussed in the following section.

3.4 Gamma rays from dark matter annihilation

As discussed in the previous subsection, gamma rays provide the best channel for indirect detection of dark matter from annihilation. This section describes the gamma-ray flux from annihilation and the parameters that determine it, especially the astrophysical J-factor and the Monte-Carlo simulated spectra for different channels dN_i/dE. The ex-

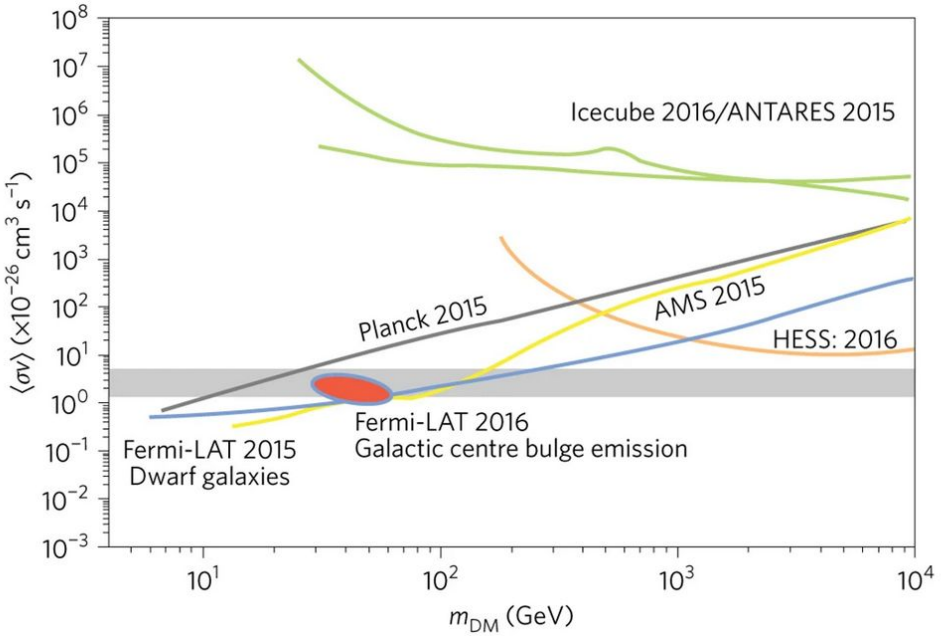

Figure 13 – Compilation of limits on the dark matter annihilation cross-section according to dark matter particle mass from different channels of annihilation. The gray band represents the typical values of the cross-section for WIMP dark matter.

Source: CONRAD *et al.* (114)

pressions for decay are also cited for completeness. This discussion was primarily derived from Cirelli *et al.* (9), which is suggested for the interested reader as a deep review.

3.4.1 The gamma-ray flux from dark matter annihilation

The gamma-ray signal observed on Earth from dark matter annihilation in some astrophysical object can be easily derived from Boltzmann equation (3.28) considering current ($n_{eq} = 0$) and small scale (Hubble H expansion is not important) Universe. In these conditions, the dark matter annihilation rate per volume reads (92)

$$\frac{dn_{DM}}{dt} = -\langle \sigma\, v \rangle\, n_{DM}^2 = -\langle \sigma\, v \rangle\, \frac{\rho_{DM}^2}{m_{DM}^2}. \tag{3.78}$$

From that, the rate of photons emitted per energy, per time and area will be

$$\frac{d\Phi_{\text{ann}}}{dE} = -\frac{1}{2}\int dV \frac{1}{4\pi s^2}\frac{dN}{dE}\frac{dn_{DM}}{dt}, \tag{3.79}$$

where $\frac{dN}{dE}$ is the gamma-ray spectrum per each annihilation, s is the distance between the observer on Earth and the astrophysical region of annihilation (the line of sight, l.o.s.), $1/4\pi s^2$ is the spherical wave propagation term and the $1/2$ avoids double counting.

Using spherical coordinates, the volume element can be written as $dV = s^2 ds\, d\Omega$, which cancels the spherical wave term and introduces a dependence with the solid angle: $dV/4\pi s^2 \rightarrow ds d\Omega/4\pi$. Replacing dn_{DM}/dt in Eq. (3.78) into (3.79) and integrating in the

object volume yields the gamma-ray flux (i.e., the number of photons observed per time, per energy, per area) from dark matter annihilation for an observer on Earth looking to a given source with solid angle $\Delta\Omega$ as

$$\frac{d\Phi_{\rm ann}}{dE}(E,\Delta\Omega) = \frac{\langle\sigma\, v\rangle}{8\pi\, m_{DM}^2}\frac{dN}{dE}\int_{\Delta\Omega} d\Omega \int_{\rm l.o.s.} ds \rho_{DM}^2. \tag{3.80}$$

The expression above is usually written considering that dark matter annihilates into different channels (see Figure 12), depending on a specific model. In this way, considering i a given annihilation channel, $\langle\sigma\, v\rangle_i$ its annihilation cross-section and dN_i/dE the gamma-ray spectrum for this channel can be written as

$$\langle\sigma\, v\rangle \frac{dN}{dE} = \sum_i \langle\sigma\, v\rangle_i \frac{dN_i}{dE} = \langle\sigma\, v\rangle \sum_i B_i \frac{dN_i}{dE}, \tag{3.81}$$

where

$$B_i = \frac{\langle\sigma\, v\rangle_i}{\langle\sigma\, v\rangle} = \frac{\langle\sigma\, v\rangle_i}{\sum_i \langle\sigma\, v\rangle_i} \tag{3.82}$$

is the branching ratio for the i-th channel.

Under these considerations, the final expression for the gamma-ray flux from dark matter annihilation will be

$$\frac{d\Phi_{\rm ann}}{dE}(E,\Delta\Omega) = \underbrace{\frac{\langle\sigma\, v\rangle}{8\pi\, m_{DM}^2}\sum_i B_i \frac{dN_i}{dE}}_{\text{PARTICLE PHYSICS}} \overbrace{J(\Delta\Omega)}^{\text{ASTROPHYSICS}}, \tag{3.83}$$

which depends on the particle physics parameters that were already discussed: the thermally averaged annihilation cross-section times velocity $\langle\sigma\, v\rangle$, the mass of the dark matter particle m_{DM}, the spectrum of gamma rays per annihilation through a i-th channel dN_i/dE and its branching ratio B_i. Beyond these terms, there is a dependency that comes from the dark matter distribution in the target, which depends on the astrophysical type of object. This term is called the J-factor,

$$J(\Delta\Omega) = \int_{\Delta\Omega} d\Omega \int_{\rm l.o.s.} ds \rho_{DM}^2 \left(r\left(s,\Omega\right)\right), \tag{3.84}$$

where r is the distance from the center of the dark matter halo, s is the distance from the observer, and Ω denotes the direction in the sky for a given region with solid angle $\Delta\Omega$.

Analogous considerations can be made for the case of dark matter decay. In this scenario, the flux will be given by

$$\frac{d\Phi_{\rm dec}}{dE}(E,\Delta\Omega) = \frac{\Gamma_{DM}}{4\pi\, m_{DM}}\sum_i B_i \frac{dN_i}{dE} D(\Delta\Omega), \tag{3.85}$$

where $\langle\sigma\, v\rangle$ is replaced by the dark matter particle decay width Γ_{DM}, the flux goes as $\sim m_{DM}^{-1}$ instead of $\sim m_{DM}^{-2}$ and the J-factor is replaced by the D-factor, defined as

$$D(\Delta\Omega) = \int_{\Delta\Omega} d\Omega \int_{\rm l.o.s.} ds \rho_{DM} \left(r\left(s,\Omega\right)\right). \tag{3.86}$$

Both J and D-factors depend on the dark matter halo model assumed. As seen in section 3.2, in the case of the inner parts of the Milky Way dark matter density can change orders of magnitude from different models, implying that the D-factor and, even more, the J-factor (due to the squared density in Eq. (3.84)) are strongly model-dependent. This high variability of the J(D)-factor makes the evaluation of the expected signal from dark matter annihilation (decay) very uncertain. The usual approach is to consider one cuspy or one cored profile model and compare the expected observations and sensitivities of different observatories using the same halo model. Sometimes a cored and a cuspy profile are used as conservative and optimistic limits, respectively. In this work, unless it is said otherwise, the Einasto profile (8) is used for the calculation of gamma-ray signals from dark matter annihilation and the extraction of limits from indirect detection.

Different astrophysical objects can act as targets for dark matter indirect searches. The astrophysical factor J/D, described by Eq. (3.84) /(3.86), depends on two characteristics of the target: its proximity to the Earth, which determines ultimately the solid angle $\Delta\Omega$, and the amount of dark matter in it. Beyond the astrophysical factor, the gamma-ray background that comes from the source is also an important aspect that must be taken into account when analyzing the prospects of indirect detection for a given target.

Dwarf galaxies, for instance, are objects dominated by dark matter, in such a way that the dark matter distribution in these targets can be measured using the motion of its stars. They also are expected to have a clean gamma-ray background, making them a robust target for dark matter indirect detection searches. Despite that, dwarf galaxies are further away than the Milky Way's Galactic Halo, which implies that they have a weaker predicted gamma-ray signal from dark matter annihilation.

The Milky Way's Halo is the closest dark matter distribution from us, which makes it a potential target for indirect detection. While the outer regions of the Galactic Halo are very clean in the astrophysical background, the dark matter density is lower than in the inner regions of the Galaxy. The Galactic Center (GC), thus, is the place where the strongest signal from dark matter annihilation is expected to come from. However, this region has a very complex environment with a strong and complex astrophysical background that is not totally understood. (115) (116) Another problem with the GC region is the high uncertainty of the J(D)-factor. That is illustrated in Figure 14 where the differential $dJ/d\Omega$ and $dD/d\Omega$-factors, defined as (9)

$$\frac{dJ}{d\Omega} = \int_{\text{l.o.s.}} ds\, \rho^2_{DM}(r) \quad \text{and} \quad \frac{dD}{d\Omega} = \int_{\text{l.o.s.}} ds\, \rho_{DM}(r) \,, \tag{3.87}$$

are shown as functions of the opening angle θ from the Galactic Center. The maps of the same quantities, in galactocentric coordinates (b, l), for the NFW, Einasto, and Burket profiles are shown in Figure 15 for comparison.

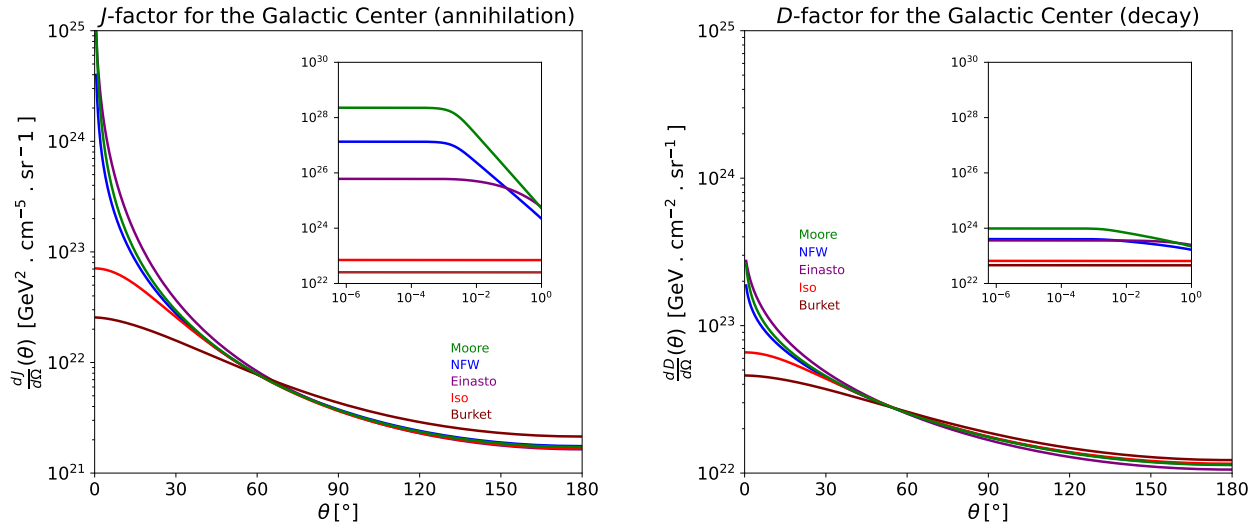

Figure 14 – Differential astrophysical factor in the Milky Way as a function of the opening angle θ from the Galactic Center as defined by Eq. (3.87). Left: the differential J-factor for annihilation in $\mathrm{Gev}^2.\mathrm{cm}^{-5}.\mathrm{sr}^{-1}$ for the profiles specified in Table 2. Right: the differential D-factor for decay in $\mathrm{Gev}.\mathrm{cm}^{-2}.\mathrm{sr}^{-1}$ for the same profiles.

Source: Adapted from CIRELLI *et al.* (9).

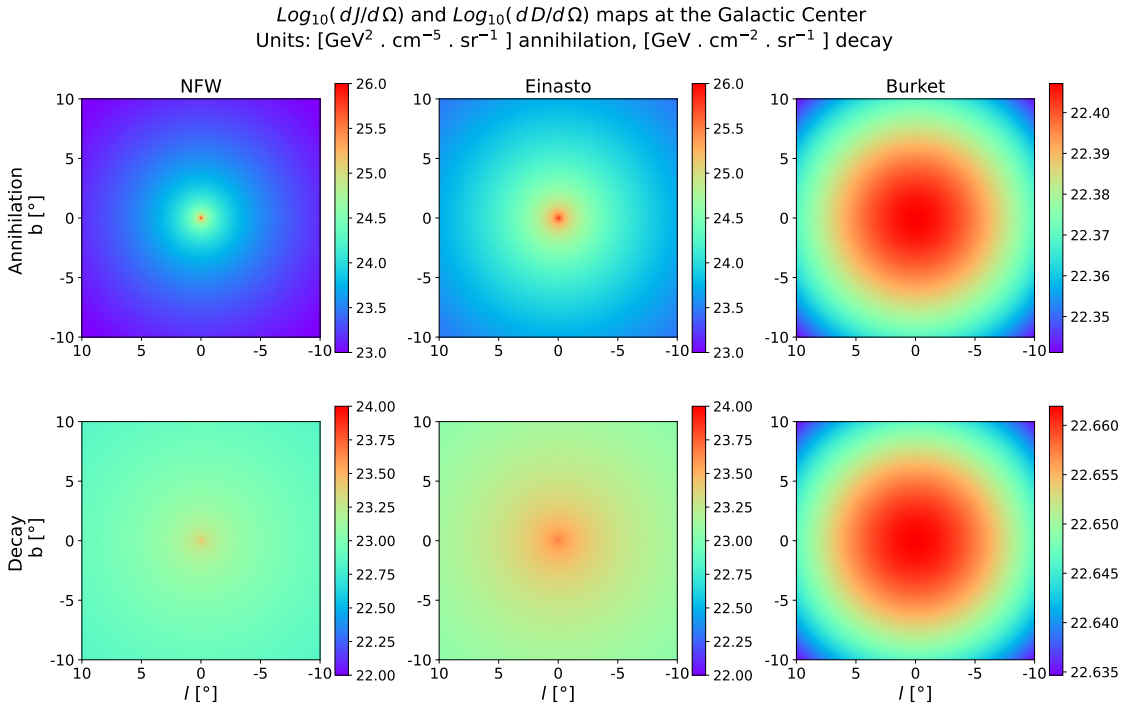

Figure 15 – Maps of the differential astrophysical factors J (annihilation) and D (decay) for the NFW, Einasto, and Burket profiles as specified in Table 2.

Source: By the author.

From these plots, it is possible to see that, for annihilation, the J-factor can change 2 or 3 orders of magnitudes in $\theta \approx 1^o$, considering cuspy or cored profiles. There is also a considerable difference even among cuspy profiles. For decay, the D-factor is approximately one order of magnitude larger for cuspy than for cored profiles, in $\theta \approx 1^o$. In the case of cored profiles, both J and D-factors are basically constants near the Galactic Center, due to the almost flat density near the center in these profiles.

3.4.2 Gamma-ray spectra from dark matter annihilation

As discussed in subsection 3.3.3, dark matter particles can annihilate and produce pairs of SM particles/antiparticles of different types. The branching ratios for these channels (see Eq. (3.82)) will depend on the model considered, but the standard approach is to suppose 100% of branching to a given primary channel and derive the gamma-ray flux and limits from it. It is also possible to use the ratios provided by a theoretical model and consider the total model-dependent spectrum. The first approach will be implemented for validation of results in chapter 6 and the second one will be implemented for a specific theoretical model.

Sub-product particles will be produced by decay or hadronization and parton showers (9), like for instance the gamma production by the channel $\pi^0 \rightarrow \gamma\,\gamma$. Gamma rays, which are the messenger of this work, can also be produced directly, but it usually happens at loop-level from some specific models. The spectra from PPPC 4 DM ID generate Monte Carlo simulations of these processes using the PYTHIA program (117) and obtain the fluxes of the final states (see Figure 12). Cirelli's spectra also consider the effects of particle polarization (left and right-handed components for fermions and longitudinal and transverse modes for vector bosons). In this work, the summed modes are considered. Other important effects are the *Electroweak corrections* (EW corrections) that come from W/Z emitted states. (118) An important case is the *virtual internal bremsstrahlung* (VIB) emission from W^+W^- primary states.

In Figure 16 are shown the gamma-ray spectra of dark matter annihilation into quark ($b\bar{b}$), lepton ($\mu^+\mu^-$) and vector boson (W^+W^-) channels. From these plots, it is possible to see some interesting spectral features of dark matter annihilation signals that differentiate them from astrophysical spectra:

- All the dark matter annihilation spectra have a variable slope, unlike the spectra of astrophysical origin, which usually follow a power-law (i.e., a constant spectral index).

- These spectra have an abrupt cutoff at the dark matter particle mass m_{DM}. That occurs because the dark matter particles are supposed to be non-relativistic, and

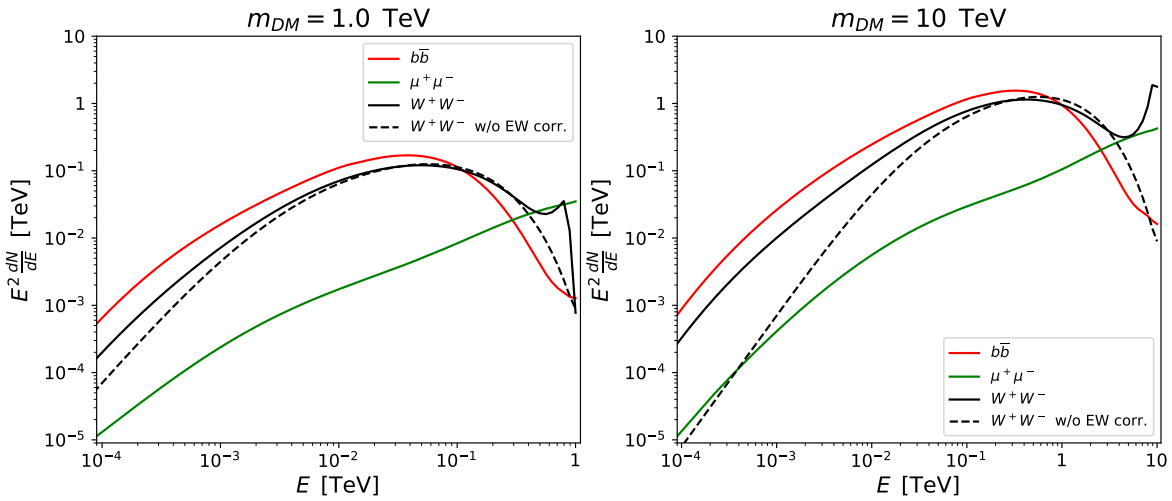

Figure 16 – Dark matter annihilation gamma-ray spectra obtained from PPPC 4 DM ID for the channels $b\bar{b}$ (red line), $\mu^+\mu^-$ (green line) and W^+W^- with (dashed black line) and without (solid black line) EW corrections. Left: spectra for $m_{DM} = 1\,\text{TeV}$. Right: spectra for $m_{DM} = 10\,\text{TeV}$.

Source: Adapted from CIRELLI *et al.* (9).

thus the energy that each gamma photon can have is at most $\approx m_{DM}$ due to four-momentum conservation.

- In the case of the W^+W^- spectra, the EW corrections produce a gamma-line just before the dark matter mass cutoff.

These features are considered spectral signatures that would characterize a dark matter discovery from indirect detection once astrophysical sources cannot reproduce them. For this reason, some dark matter indirect searches with gamma rays try to identify these specified "smoking gun" traces. (6)

The spectra also have differences among themselves: the leptonic $\tau^+\tau^-$ spectra are harder while the bosonic and quark ones are softer, beyond that the EW corrections enhance considerably the W^+W^- spectrum and produce a gamma-line, as said before. These distinctions will produce differences in the $\langle \sigma\, v \rangle$ limits.

4 DETECTING DARK MATTER WITH GAMMA-RAY ASTRONOMY

Now that the flux of gamma rays from dark matter annihilation and the spatial (J-factor) and energetic (spectrum) aspects have been discussed, this chapter will address the observational and statistical basis that is necessary to analyze gamma-ray data and estimate fluxes from dark matter that are studied in indirect detection searches.

Gamma rays are the most energetic form of radiation in the electromagnetic spectrum. Astrophysical gamma rays can be produced in extreme environments such as supernovae, pulsars, supermassive black holes, and gamma-ray bursts (GRB). They are generally produced via the interaction of cosmic rays (i.e., charged particles from space) with the interstellar or intergalactic medium. (112) In fact, gamma rays and cosmic rays are very important for high-energy astrophysics since their spectra cannot be explained by usual thermal processes. Beyond those astrophysical origins, gamma rays theoretically can be produced by the annihilation of dark matter particles across space, as explained in section 3.4, and then be detected with telescopes on Earth.

This type of radiation has some peculiarities that differentiate its detection from other fields of astronomy. When gamma rays reach the Earth, they are absorbed by the atmosphere, producing a series of sub-product particles in their interaction. This means that ground-based instruments cannot detect them directly. Even in the case when gamma rays can be directly detected, neither reflection nor capture techniques can be used since the wavelength of these photons is below the atomic scale. These characteristics imply that gamma rays must be detected using alternative technologies.

This chapter discusses the main telescopes of gamma-ray astronomy and their response to a theoretical flux. It will also discuss the statistical method considered to claim detection in this field. In the end, it will be explored how those gamma-ray observations can point towards a discovery or an exclusion of a region of the parameter space of the WIMP dark matter scenarios.

4.1 Gamma-ray telescopes

There are two main kinds of detection methods used in gamma-ray astronomy: the first one is to use particle detectors in space telescopes before gamma rays interact with the atmosphere. This technique is viable for gamma rays with energies in the $\sim 10\,\mathrm{MeV} - \sim 500\,\mathrm{MeV}$ range. The second one is based on detecting the particles produced by the shower generated when the gamma rays travel in the atmosphere. In this case, only gamma rays with energies roughly above some tens of GeV have sufficient energy to generate a detectable shower. This second type can be divided into two sub-categories: i) air shower

particle detectors, which detect the secondary particles during the development of the shower; ii) *Imaging atmospheric Cherenkov telescopes* (IACTs), which use the Cherenkov light cone that is produced by the particle shower. The representation of a gamma ray and the *extensive air shower* that is produced when it enters the atmosphere with their respective methods of detection along altitude are shown in Figure 17. These different types of telescopes are complementary in energy and together can explore the whole range of gamma-ray events from space.

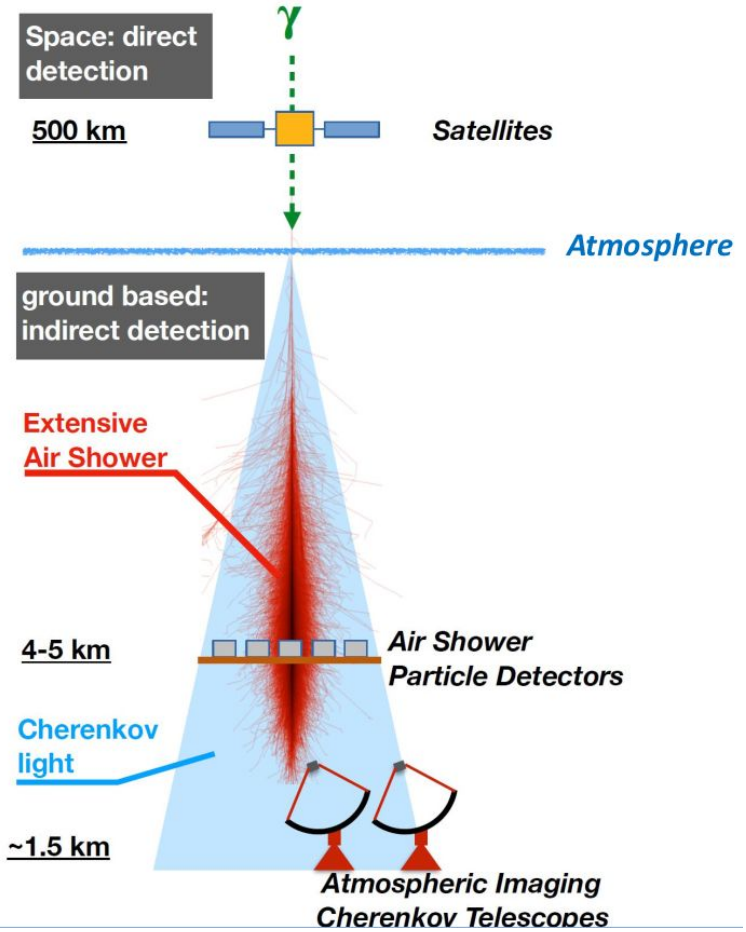

Figure 17 – Representation of the detection methods of gamma-ray astronomy. Above the atmosphere, the primary gamma ray can be measured by detectors embedded in space satellites. After entering the atmosphere, the gamma-ray produces an extensive air shower of secondary particles. In high altitudes, surface detectors can be used to detect the secondary particles along the development of the shower. At low altitudes, IACTs can be used to detect the Cherenkov light cone produced after the development of the shower.

Source: VIANA. (119)

4.1.1 Satellites

Space-based gamma-ray telescopes are instruments onboard satellites that orbit the Earth. These devices are usually based on detectors developed for particle physics that can measure directly the gamma-ray before their interaction with the atmosphere. A strong advantage of space telescopes is that they can have almost 100% of duty cycle because they are not under the day-night cycle, unlike many of the ground-based telescopes. Another advantage is the full sky coverage. A disadvantage is that, due to the high cost of space launching, they must be small in size, which implies a small area and a small rate of observed events. Another problem is that the very-high energy gamma rays cannot be detected by this method because the materials used are usually transparent to them, limiting the energy range up to some hundreds of GeV.

The main gamma-ray telescope nowadays is the Large Area Telescope (Fermi-LAT) which is one of the devices of the Fermi Gamma-Ray Space Telescope spacecraft, together with the Gamma-ray Burst Monitor (GBM). (120) LAT is a gamma-ray telescope that covers an energy range from 20 MeV up to 300 GeV, it has an area of 0.95 m^2 and a field of view of 2.4 sr, approximately 19% of the sky. (121) It was launched by NASA in August 2008 and remains in operation still today. The working principle is the electron-positron pair production when the gamma ray enters the detector. A calorimeter is used for energy measurement and an anticoincidence detector identifies possible cosmic-ray events. The Fermi satellite and the scheme of work of LAT are shown in Figure 18. Fermi-LAT has made not only important discoveries in gamma-ray astrophysics but also has established the best limits for WIMPs in the lower range of dark matter masses (GeV scale). LAT has also discovered an unexpected signal from the Galactic Center known as the Galactic Center Excess which one of the possible explanations is the dark matter annihilation in this region. (122) This claim is still controversial, however.

4.1.2 Ground-based observatories

At high altitudes, around 4000 meters, gamma rays can be indirectly detected. One of the most implemented techniques is using the water tanks. The idea is that the secondary particles of the shower move at relativistic speed and emit Cherenkov light when enter water tanks because they are faster than light in water. The light can be detected by photomultipliers and the energy and direction of the primary gamma ray can be, with given uncertainties, reconstructed by computational methods. This kind of detector has advantages such as a wide field of view (order of one steradian) and a 100% duty cycle. They cover energies above some hundreds of GeV up to several PeV and are especially sensitive above 10 TeV. The main operating air shower particle detectors are the High-Altitude Water Cherenkov Gamma-ray Observatory (HAWC) (123), in Mexico, and the Large High Altitude Air Shower Observatory (LHAASO) (124), in Haizi Moun-

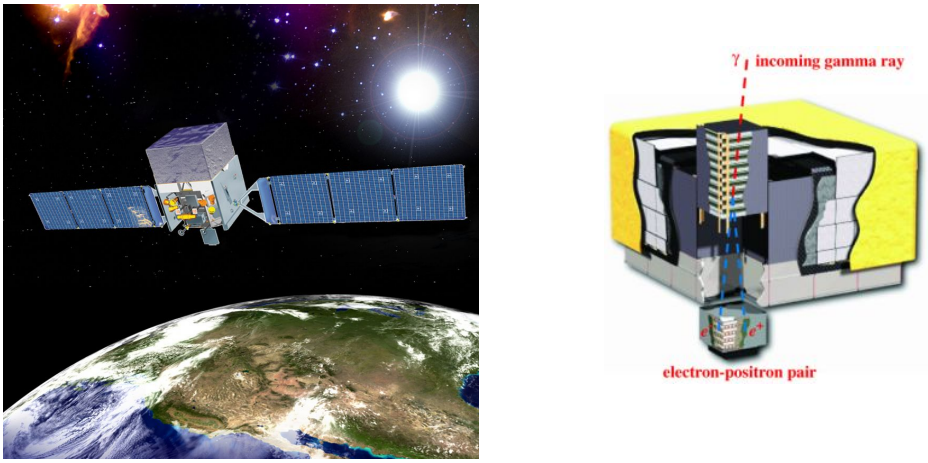

Figure 18 – Left panel: artistic representation of the Fermi satellite in its orbit. Right panel: illustration of the instruments of Fermi-LAT and the electron-positron pair production technique.

Source: NASA (120); ATWOOD *et al.* (121)

tain, China. These two observatories are in the Northern Hemisphere and there is no observatory of such kind in the Southern Hemisphere, which is the best place to observe the Galactic Center. A future instrument that is in development to supply this absence is the Southern Wide-Field Gamma-ray Observatory (SWGO). (125) SWGO will be a detector very similar to HAWC but with a larger area and sensitivity. It will be built in some locations of South America at 4400 meters of altitude or higher.

IACTs are ground-based gamma-ray instruments that use a different method. Instead of detecting the particles at high altitudes, they detect the Cherenkov light cone that is produced in the atmosphere (see Figure 17). They have some disadvantages compared to surface detectors, such as a smaller field of view (<10 degrees) and just night cycle, due to the extreme sensitivity of the cameras to the sunlight. Nevertheless, IACTs are the most sensitive experiments in the 100 GeV - 10 TeV energy range, making them important to cover the gap between satellite detectors and air shower detectors. The pioneering experiment of this type was Whipple (126), which started its operation in 1982 and demonstrated the viability of this strategy. Subsequent experiments have tested the idea of using the stereoscopic technique which consists of using many Cherenkov telescopes to reconstruct the Cherenkov cone and the primary gamma ray. Among them, we can cite the experiments High Energy Stereoscopic System (HESS) (127), Very Energetic Radiation Imaging Telescope Array System (VERITAS) (128), and Major Atmospheric Gamma Imaging Cherenkov telescope (MAGIC) (129). These experiments succeeded in showing the efficiency of this technique having made important discoveries in gamma-ray astronomy.

The HESS telescope is an IACT in operation since 2003 in the Namibian desert at an altitude of 1800 meters and was initially composed of an array of four telescopes of

12-m-diameter (Phase I). After 2012, a single 28-m-diameter telescope was added to the array (Phase II), making HESS the largest atmospheric Cherenkov telescope in the world currently. HESS is also the first IACT in the Southern Hemisphere with good sensitivity and it covers mainly the hundreds of GeV to TeV energies. VERITAS is an array of four 12-m-diameter built in Arizona, United States of America, and it has a sensitivity very similar to HESS, but in the opposite hemisphere. MAGIC is composted by two 17-m-diameter telescopes, in La Palma, Spanish territory of the Canary Islands, at 2200 meters of altitude. (130)

The Cherenkov Telescope Array (CTA) will be an array of many atmospheric Cherenkov telescopes of different sizes that was proposed to increase by at least one order of magnitude the sensitivity, extend the energy range to four decades of energy, from tens of GeV to hundreds of TeV, and improve angular and energy resolutions compared to previous telescopes. (131) The CTA Observatory (CTAO) will have two sites, the northern one is going to be built in the Canary Islands, Span, and the southern site in Paranal, Chile. CTAO North will focus on extragalactic sources while CTAO South will focus on galactic sources. (130) CTA is one of the priorities of the astrophysics community and will investigate questions such as the origin of cosmic rays, compact objects, like pulsars and black holes, Lorentz Invariance Violation, transient phenomena such as GRBs, and dark matter. (132) CTAO South is significant for dark matter indirect searches since the Galactic Center is one of its major targets.

To achieve its goals, CTA is projected to work with three types of telescopes: LSTs, MSTs, and SSTs. The Large Sized Telescopes (LSTs) are 23-m-diameter telescopes projected to detect the lower energy gamma rays, between some tens of GeV and 100 GeV, having a good overlap with the Fermi-LAT energy range. The LSTs will be able to detect new AGNs sources, which makes them promising in the CTAO North site. The prototype of a LST is already installed in La Palma and is the first built telescope of CTAO North. The Medium Sized Telescopes (MSTs) are 12-m-diameter telescopes that operate in the energy range usually searched by IACTs of 100 GeV - 50 TeV, improving previous energy and angular resolutions. The Small Sized Telescopes (SSTs) will cover the high energies from the 50 - 300 TeV range. These are 5-m-diameter and have to cover a larger area to compensate for the expected low signal. SSTs are primarily interesting in CTAO South since the galactic gamma-ray sources are the main targets at these energies. (130) The actual design of CTA is known as “Alpha Configuration” which consists of 4 LSTs and 9 MSTs in CTAO North, covering an area of ≈ 0.25 km^2, and 14 MSTs and 37 SSTs in CTAO South, covering ≈ 3 km^2. (133) Figure 19 illustrates the telescope arrays for HESS and CTA.

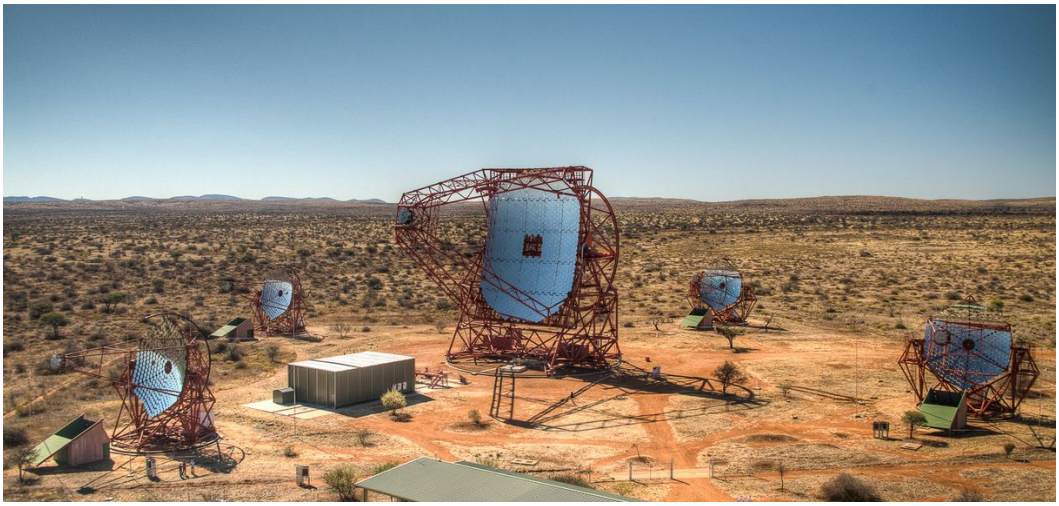

(a) Picture of the 28 and the four 12-meter telescopes of HESS, in the Namibian desert. Image credit: HESS Collaboration. Available at: https://www.mpi-hd.mpg.de/HESS/pages/home/Webgalleries/HESS2_telescope/index.html. Accessible at: Jan 16.

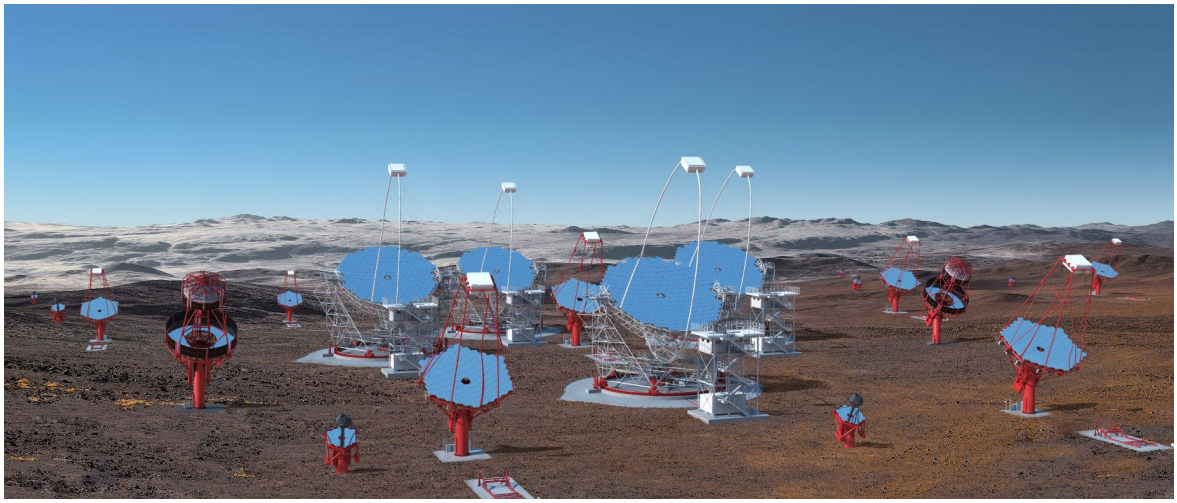

(b) Artistic illustration of the CTA array. Image credit: Gabriel Pérez Diaz, IAC/Marc-AndréBesel, CTAO.

Source: CHERENKOV TELESCOPE ARRAY CONSORTIUM. (134)

Figure 19 – Images of IACT arrays: (a) picture of HESS, with Phase I and Phase II telescopes and (b) artistic representation of CTA.

4.1.3 Instrument response functions and sensitivity

For a given flux to be detected by a gamma-ray telescope, the air shower events are separated into gamma or hadron events, and energy and direction are numerically reconstructed. The observed count of gamma-ray events will depend on certain properties of the detector system. These properties are encoded by the so called *instrument response functions* (IRFs). Suppose a differential flux from a source of solid angle $\Delta\Omega$ is given by $d\Phi/dE$ ($\mathrm{TeV}^{-1}.\mathrm{cm}^{-2}.\mathrm{s}^{-1}$), then the gamma-ray events number in an energy range $\Delta E'$ will be (135)

$$N = T_{\mathrm{obs}} \int_{\Delta E'} dE' \int_0^\infty dE \; \frac{d\Phi}{dE} \; A_{\mathrm{eff}}\left(E, \Delta\Omega\right) R(E, E'), \tag{4.1}$$

where T_{obs} is the observation time, E refers to the *true energy*, E' to the *reconstruct energy*, A_{eff} is the *effective area* in the function of the true energy and R is the probability density function of obtain E' for a given E.

The IRFs are functions usually obtained from Monte Carlo simulations of the extensive air shower and depend mainly on the zenith angle of observation and the offset, (136) i.e., the angle between the pointing of the telescope and the direction of observation. The effective area depends on the energy and is usually described as the acceptance of the detector to a signal. Another important parameter is the energy threshold E_{th}, below which the instrument acceptance becomes negligible. It is often defined as the point of 10% of the maximum effective area. (137) The reconstruction probability R is usually modeled as a normal (or log-normal) distribution above the energy threshold (138) and it is characterized by the energy resolution, defined by the root mean square of $\left(E - E'\right)/E$. For HESS, the energy resolution is around 10% above 200 GeV. (136) Similar considerations can be made for the angular resolution*, but they are not relevant in the context of this work. Figure 20 shows simulations for the effective area and the energy resolution of CTAO South. The effective area depends on the optimization of gamma/hadron separation for different observation times. (133) The energy resolution plot shows that CTAO Souh will surpass Fermi-LAT in energy resolution above $\approx$ 500 GeV and VERITAS for all energies.

Another function important to analyze the performance of a telescope is the differential sensitivity, defined as the minimal flux necessary to obtain a 5σ detection, considering a point-like source. Fig 21 shows the differential sensitivities for different gamma-ray instruments, calculated for logarithmic energy bins, 5 for each decade. Beyond the statistical significance required, 10 photons per bin and at least 1/20 for the signal/background ratio are required. This comparison shows that CTA will overcome the sensitivity of all present and future instruments in the 100 GeV - 10 TeV range, in both hemispheres.

* See the section *Angular Resolution* on (133).

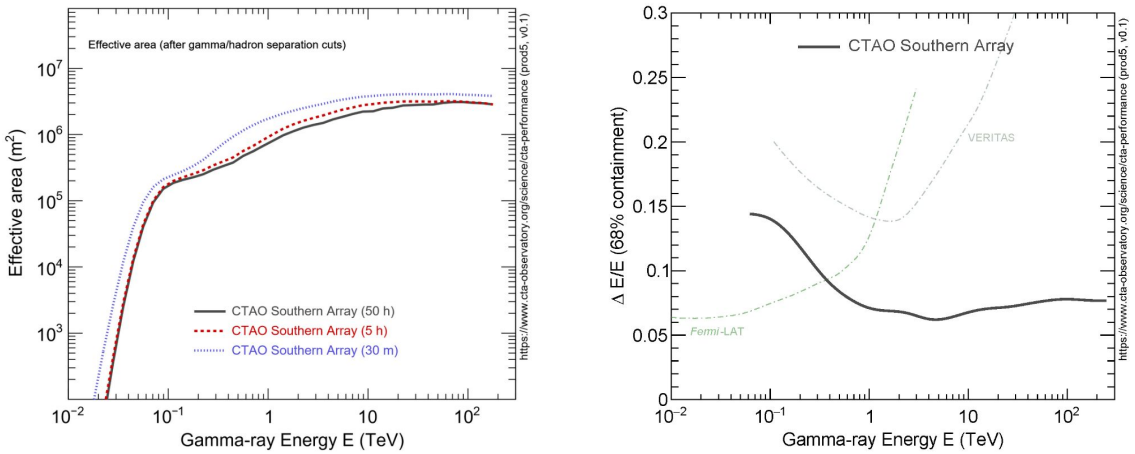

Figure 20 – Instrument response functions of CTAO South according to the current Alpha Configuration. Left panel: effective area versus true energy for 30 m, 5 h and 50 h of time observation. Right panel: energy resolution versus true energy for CTAO South, Fermi-LAT and VERITAS.

Source: CHERENKOV TELESCOPE ARRAY CONSORTIUM. (133)

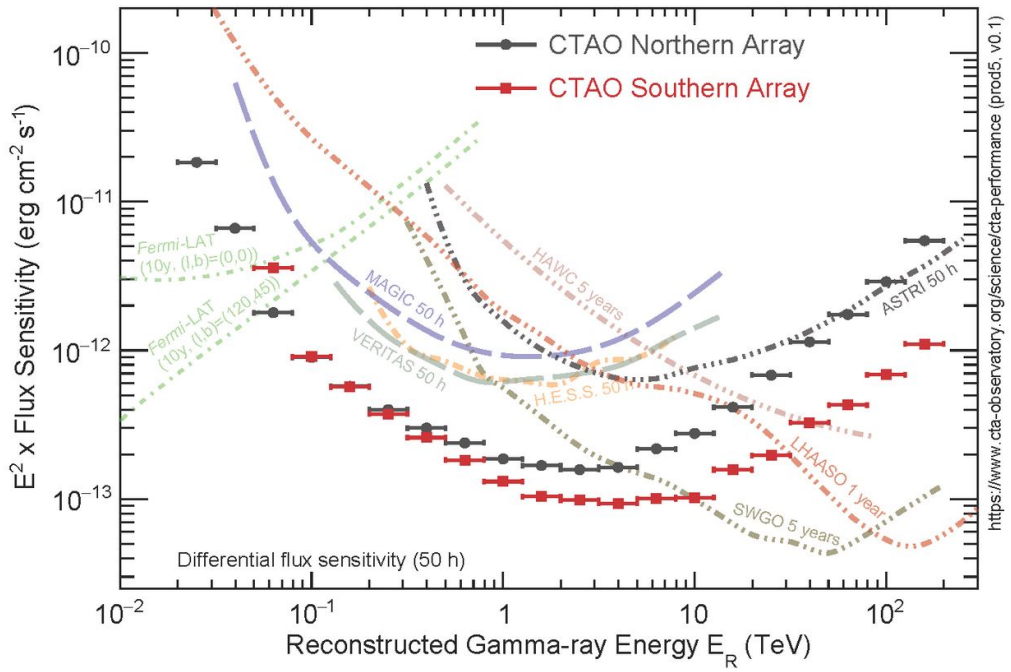

Figure 21 – Differential sensitivity on function of the reconstructed energy for different gamma-ray instruments, in both hemispheres. The differential sensitivities of CTAO North (black) and South (red) are shown together with the energy bins (five per decade).

Source: CHERENKOV TELESCOPE ARRAY CONSORTIUM. (133)

4.2 Statistical analysis

In many fields of science, in special high-energy particle physics and gamma-ray astrophysics, the evidences of new physics (or new astrophysical sources) can be known only statistically, since many processes occur together. Different kinds of statistical tests can be made for different purposes, but here we will focus on the *log-likelihood ratio test* (LLRT) for statistical hypothesis tests. This kind of method was used in the discovery of the Higgs boson, for instance, and is used for the search of new physics and, particularly, in the searches for the dark matter particle.

The main concept that must be defined here is the *likelihood function* of a dataset and a distribution model. Usually, in probability and statistics, the probability of a certain occurrence happening is given by a probability (density) function. This function depends on a set of parameters $\theta = (\theta_1, \theta_2, ..., \theta_n)$ that is known *a priori* and determine the probability (or the probability density in the case of continuous variables) of an aleatory variable to take the value $X = x$, i.e.,

$$p\left(X = x\right) = P_\theta\left(x\right). \tag{4.2}$$

Generalizing this problem to many observations statistically independent is straightforward. In empirical sciences, however, we are usually dealing with the opposite problem, the dataset $\mathbf{x} = (x_1, x_2, ..., x_m)$ is known and the parameters set is what we want to estimate.

To understand this problem better, the likelihood function of the dataset $\mathbf{x}$ with the model P with parameters set θ is a function mathematically identical to the probability function P_θ but with independent variables as θ, and X is set on $X = \mathbf{x}$, i.e.,

$$\mathcal{L}\left(\mathbf{x}|\theta\right) = P_\theta\left(\mathbf{x}\right). \tag{4.3}$$

A simple example of the likelihood function is the estimation of the parameters through a sequence of measurements that gives a dataset. This is also known as parameter fitting.

To give an example of the use of the likelihood function, let us show how to obtain the least squares method for parameter estimation. Suppose that two variables X and Y are related through a function $Y = f\left(X\right)$ which depends on a set of unknown parameters, $f\left(X\right) = f\left(X;\beta\right)$. Consider then that a sequence of measurements of data (x_i, y_i) is taken for the pair of variables considered before. One can model these measurements as normal distributions of y_i with mean $f\left(x_i;\beta\right)$ for each x_i and variance fixed by the instrument properties, σ_i, which can assume different values at each i-th measurement. If each measurement is statistically independent from the others, the likelihood is given by

$$\mathcal{L}\left(\mathbf{x}, \mathbf{y}, \sigma|\beta\right) = \Pi_i \frac{1}{\sqrt{2\pi}\sigma_i} \exp\left(-\frac{\left(y_i - f\left(x_i;\beta\right)\right)^2}{2\sigma_i^2}\right). \tag{4.4}$$

The σ_i's are the only parameter known, while the vector of parameters β must be determined. The maximum likelihood estimation states that the best parameters estimation is the set that maximizes the likelihood, for a given dataset. Therefore, the best values for β can be obtained by the maximum condition

$$\frac{\partial \ln(\mathcal{L})}{\partial \beta_j} = 0, \quad \forall \beta_j. \tag{4.5}$$

See that maximizing $\ln(\mathcal{L})$ corresponds to maximizing $\mathcal{L}$ once the logarithm function is monotonically crescent. In this case, this condition implies that the best fit $\hat{\beta}$ is determined by

$$\hat{\beta} = \arg\min \left(\sum_i \frac{(y_i - f(x_i;\beta))^2}{\sigma_i^2} \right), \tag{4.6}$$

which, of course, will depend on the functional form of f. The quantity to be minimized is usually known as residual error of the least squares method. This is a simple but widely useful method of parameter estimation using the maximization of a likelihood function.

In the next subsections, the likelihood function will be used for comparison of models and test of hypothesis in physics.

4.2.1 The log-likelihood ratio test (LLRT)

In many fields of high-energy physics, a common sort of question that arises is how to compare two competitive models for some phenomenon or how to test a hypothesis of new physics, or, in gamma-ray astronomy, confirm the presence of a new source in some region of the sky. These phenomena are usually ruled by stochastic processes, which implies that the answer to these questions can only be made through statistical tests with a certain confidence level. Among the statistical techniques used, the *log-likelihood ratio test* (LLRT) is one of the most robust and will be used in the present work. This method is based on the Wilks' theorem, (139) stated below.

Wilks' theorem: Consider a model $\mathcal{L}(\mathbf{x}|\theta)$ with parameters $\theta = (\lambda_1, \lambda_2, ..., \lambda_r, \mu_1, \mu_2, ...) = (\lambda, \mu)$. Suppose a hypothesis that consists in assuming that a subset of parameter is fixed to some values, i.e., a null hypothesis, given by $\lambda = \lambda_o = (\lambda_1^o, \lambda_2^o, ..., \lambda_r^o,)$ and $\theta_o = \left(\lambda_o, \hat{\hat{\mu}}_o\right)$ where $\hat{\hat{\mu}}_o$ are the values obtained from the conditional maximization of the likelihood function at $\lambda = \lambda_o$. Defines the log-likelihood test statistic (TS) for a given dataset $\mathbf{x}$ as

$$TS \equiv -2 \ln \left[\frac{\mathcal{L}\left(\mathbf{x}|\lambda_o, \hat{\hat{\mu}}_o\right)}{\mathcal{L}\left(\mathbf{x}|\hat{\lambda}, \hat{\mu}\right)} \right], \tag{4.7}$$

where $\left(\hat{\lambda}, \hat{\mu}\right)$ are the values that give the global maximum of the likelihood function. Wilks' theorem states that, as the dataset becomes larger, if the null hypothesis is true, TS goes to a χ^2 distribution of r degrees of freedom, where r is the number of fixed

parameters in the null hypothesis. Therefore,

$$TS \sim \chi^2(r). \tag{4.8}$$

A χ^2 distribution of r degrees of freedom is the distribution function obtained by the quadratic sum of r normal standard variables, i.e., $TS \sim \chi^2(r)$ if $TS = \sum_k^r u_k^2, u_k \sim N(0,1)$. Using the $\chi^2(r)$ distribution as a standard, it is possible to define a confidence interval (or the p-value). If one wants to determine the confidence level (C.L.) associated with the significance S of a given dataset, it is defined as (140)

$$S = \sqrt{TS} = \Phi^{-1}(C.L.) = \Phi^{-1}(1-p), \tag{4.9}$$

where $\Phi(z) = \int_0^z \rho(z')\,dz'$ is the cumulative function of the probability distribution ρ of S. The p-value and the C.L. are defined as complementary of each other. For instance, if an exclusion limit of 95% C.L. ($p = 0.05$) is required for 1 degree of freedom, the significance level for a one-sided distribution is $S \approx 1.65\,(TS \approx 2.71)$. That is typically the significance required by the exclusion of a hypothesis on new physics searches.

4.2.2 The ON/OFF method

The method to claim a discovery in gamma-ray astronomy was rigorously established by Li & Ma in their 1983 paper (141), where they in principle supposed a point-like source or gamma-lines, but it can be extended to sources such as dark matter annihilation in the Galactic Center, for instance. In this sub-section, this method, known as the ON/OFF method, will be briefly described.

In gamma-ray astronomy, the observable, the gamma-ray count, follows a Poisson distribution whose likelihood is given by

$$\mathcal{L}(N|\lambda) = \frac{\lambda^N e^{-\lambda}}{N!}, \tag{4.10}$$

where N is the observed count and λ is the expected value of the count. The Poisson distribution has the interesting property that its mean equals its variance $\langle N \rangle = \mathrm{Var}(N) = \lambda$. The situation considered by Li & Ma was the following. Suppose a certain region of the sky, called the ON region, where there is possibly an unknown source. There is another region, the OFF region, where there is just a background emission which is also present in the ON region. In the original paper, the authors considered a normalization between the regions considering the observation time. In our case, the ON and OFF regions have the same exposure, but each region has a different solid angle $\Omega_{ON/OFF}$. The background emissions (supposedly uniform) in both regions are related by $\alpha = \Delta\Omega_{ON}/\Delta\Omega_{OFF}$. The likelihood will be thus given by

$$\mathcal{L}(N_{ON}, N_{OFF}, \alpha|S, B) = \frac{(S+B)^{N_{ON}}}{N_{ON}!} e^{-(S+B)} \frac{(B/\alpha)^{N_{OFF}}}{N_{OFF}!} e^{-(B/\alpha)}, \tag{4.11}$$

where N_{ON} and N_{OFF} are the gamma-ray counts in the ON and OFF regions, respectively, S is the expected count from the signal of the new source, and B is the background count, which emission is present in both regions.

The problem considered in this work (dark matter annihilating in an astrophysical object) is very similar, but instead of just one ON and one OFF regions, multiple ON and OFF regions of interest (ROIs) are observed, since the source is not exactly point-like. We are also interested in the spectral features that could differentiate the background from the signal, as discussed in subsection 3.4.2. This means that a 2D analysis is necessary, with a binning in energy and another in space. In this case, the total likelihood will be a combination of the likelihood of each ROI,

$$\mathcal{L} = \Pi_{ij}\mathcal{L}_{ij}, \tag{4.12}$$

where

$$\mathcal{L}_{ij}\left(N_{ONij}, N_{OFFij}, \alpha | S_{ij}, B_{ij}\right) = \frac{\left(S_{ij}+B_{ij}\right)^{N_{ONij}}}{N_{ONij}!} e^{-(S_{ij}+B_{ij})} \frac{\left(B_{ij}/\alpha\right)^{N_{OFFij}}}{N_{OFFij}!} e^{-(B_{ij}/\alpha)}. \tag{4.13}$$

The terms in this expression are analogous to the ones in Eq. (4.11). The index i refers to the energy binning while j refers to the spatial binning.

Wilks' theorem can then be applied to the likelihood of Eq. (4.13), where the null hypothesis consists in $S_{ij} = 0$. The test statistic is given by (141)

$$TS = 2\sum_{ij}\left\{N_{ONij}\ln\left[\left(\frac{1+\alpha}{\alpha}\right)\left(\frac{N_{ONij}}{N_{ONij}+N_{OFFij}}\right)\right] + N_{OFFij}\ln\left[(1+\alpha)\left(\frac{N_{OFFij}}{N_{ONij}+N_{OFFij}}\right)\right]\right\}. \tag{4.14}$$

In gamma-ray astronomy, this test statistic can be used for the discovery of a new source, which can be claimed if $TS \geq 25$ (5σ test). The next subsections will deal with the question of how to use this method to constrain the parameters of self-annihilating dark matter.

4.2.3 Test statistic for dark matter detection with gamma rays

In the case of searches for new physics in high energies and the determination of upper limits for parameter exclusion, a similar log-likelihood statistic test can be used, for both discovery of the new phenomenon or exclusion limits. This method was reviewed by Cowan *et al.* (140) and Rolke *et al.* (142), and are suggested to the interested reader. It is the same method that was used in the Higgs boson discovery at the LHC in 2012. (140)

Suppose that in a certain region of the sky, gamma-ray signals of dark matter annihilation are expected (ON region). Consider, then, that this region is split in spatial bins of solid angle $\Delta\Omega_{ONj}$, and for each one we have an OFF region of solid angle $\Delta\Omega_{OFF_j}$,

and hence an ON-OFF ratio α_j. The reconstructed energy is also split into bins ΔE_i, which must be above the energy threshold, $E_i > E_{\rm th}$. Each of these ROIs and energy bin will have a 2D-binned likelihood given by Eq. (4.13), but now the signal parameters S_{ij} are functions of the annihilation rate $\langle\sigma\, v\rangle$ and the WIMP mass m_{DM} through the expression

$$S_{ij}\left(\langle\sigma\, v\rangle\right) = \langle\sigma\, v\rangle \frac{T_{\rm obs} J\left(\Delta\Omega_j\right)}{8\pi m_{DM}^2} \int_{\Delta E_i'} \int_0^\infty \frac{dN}{dE} A_{\rm eff}(E) R(E, E'), \tag{4.15}$$

which is obtained by substituting Eq. (3.80) into Eq. (4.1). In this expression, the dark matter annihilation spectra dN/dE depend on the dark matter particle mass m_{DM}. This means that the mass must be fixed and, for a given J-factor, annihilation cross-section is the only free variable of S_{ij}. The total likelihood will be, thus,

$$\mathcal{L}\left(N_{ON}, N_{OFF}, \alpha | \langle\sigma\, v\rangle, B\right) = \Pi_{ij} \mathcal{L}_{ij}\left(N_{ONij}, N_{OFFij}, \alpha | \langle\sigma\, v\rangle, B_{ij}\right), \tag{4.16}$$

where $\langle\sigma\, v\rangle$ and $B = \{B_{ij}\}$ are the free variables and $N_{ON} = \{N_{ONij}\}$, $N_{OFF} = \{N_{OFFij}\}$, and α are the dataset. To simplify the notation let us write $\mathcal{L}\left(N_{ON}, N_{OFF}, \alpha | \langle\sigma\, v\rangle, B\right) = \mathcal{L}\left(\langle\sigma\, v\rangle, B\right)$. With these definitions, we can now understand the test statistics for discovery and upper limits determination.

Following the steps made in Ref. (140), one can define the profile likelihood ratio associated with the variable $\langle\sigma\, v\rangle$ as

$$\lambda\left(\langle\sigma\, v\rangle\right) = \frac{\mathcal{L}\left(\langle\sigma\, v\rangle, \hat{\hat{B}}\right)}{\mathcal{L}\left(\widehat{\langle\sigma\, v\rangle}, \widehat{B}\right)}, \tag{4.17}$$

where $\hat{\hat{B}}$ is the background in the conditional maximum of $\mathcal{L}$ for the specific value of $\langle\sigma\, v\rangle$, and $\widehat{\langle\sigma\, v\rangle}$ and $\widehat{B}$ are the parameters of the global maximization of $\mathcal{L}$.

The test statistic for discovery is the same as Wilks' theorem (4.7), with the correction of null significance for the case of $\widehat{\langle\sigma\, v\rangle} < 0$, since the annihilation cross-section must be positive, i.e., (140)

$$TS_{\rm discovery} = \begin{cases} -2\ln\lambda(0), & \widehat{\langle\sigma\, v\rangle} \geq 0 \\ 0, & \widehat{\langle\sigma\, v\rangle} < 0 \end{cases}. \tag{4.18}$$

A discovery can be claimed only if $TS > 25$. For a negative result, the values of $\langle\sigma\, v\rangle$ can be excluded by an upper limit that is obtained according to a different, but similar, test statistic that is given by

$$TS_{\rm upper}\left(\langle\sigma\, v\rangle\right) = \begin{cases} -2\ln\frac{\lambda(\langle\sigma\, v\rangle)}{\lambda(0)}, & \widehat{\langle\sigma\, v\rangle} < 0 \\ -2\ln\lambda\left(\langle\sigma\, v\rangle\right), & 0 \leq \widehat{\langle\sigma\, v\rangle} \leq \langle\sigma\, v\rangle \\ 0, & \langle\sigma\, v\rangle < \widehat{\langle\sigma\, v\rangle} \end{cases}. \tag{4.19}$$

This test statistic thus determines exclusion limits according to the chosen p-value. Usually, an exclusion at 95 % C.L. is considered, which implies a test statistic of $TS = 2.71$.

The upper limit for the annihilation cross-section of a dark matter particle of fixed mass $m_D M$ is thus determined by

$$\langle \sigma\, v \rangle^{95\%CL} = TS^{-1}_{\text{upper}}\,(2.71)\,. \tag{4.20}$$

Other effects can be considered here, such as systematic error and a signal in the OFF regions, but here only statistical error and signal in the ON regions will be considered. Moreover, the exclusion upper limits can be determined by measured N_{ON} and N_{OFF}, which are known as *observed limits*, or evaluated at the condition $N_{ONij} = \alpha N_{OFFij}$, known as *expected limits*, which are the results that would be expected in the absence of an excess signal.

4.3 Upper limits for indirect dark matter detection with gamma-rays at the Galactic Center region

The GC region is, as discussed earlier, the region that must produce the strongest signal near Earth from dark matter annihilation. The search for gamma rays from that origin has, however, limitations due to the complex astrophysical emission in this region. There are, thus, two main approaches. The first one consists of modeling the astrophysical emission while the second implements the ON/OFF method and puts a mask on known gamma-ray sources. In this work, we use the mask method because it is simpler and not so impacted by systematic uncertainties.

In this work, the ON regions are defined as concentric disks around the GC position $(l, b) = (0, 0)$ of 0.1° width with a mask within the galactic latitudes $b = \pm 0.3^\circ$. This mask excludes gamma-ray emissions around the TeV scale (135), such as the diffuse emission in the GC Ridge (143) (144), the GC central source (145) and others (135). The ON regions are chosen to observe the dark matter signals from the largest J-factor possible. The dark matter density model is assumed to be the Einasto profile (8), whose parameters were given in Table 2. The OFF regions, in turn, are chosen as reflected regions of the sky that are symmetric to the ON regions relative to the pointing position. This ensures that the IRFs will be the same at the same offset and observation time. The scheme of pointing and division in the ON/OFF method that will be used by the CTA is illustrated in Figure 22. The opening angles, solid angle, and J-factor of the ON ROIs are shown in Table 3. The OFF regions considered here have the same solid angle ($\alpha = 1$) but insignificant J-factors.

With the values of the J-factor evaluated and the IRF given (either experimentally or numerically simulated), the signal described by Eq. (4.15) can be evaluated, for a given observation time T_{obs}. The only ingredient that remains unknown is the dataset composed by the observed counts N_{ON} and N_{OFF}. They can be given by real data from present observatories, such as the HESS telescope, or by numerical simulations, which is the case

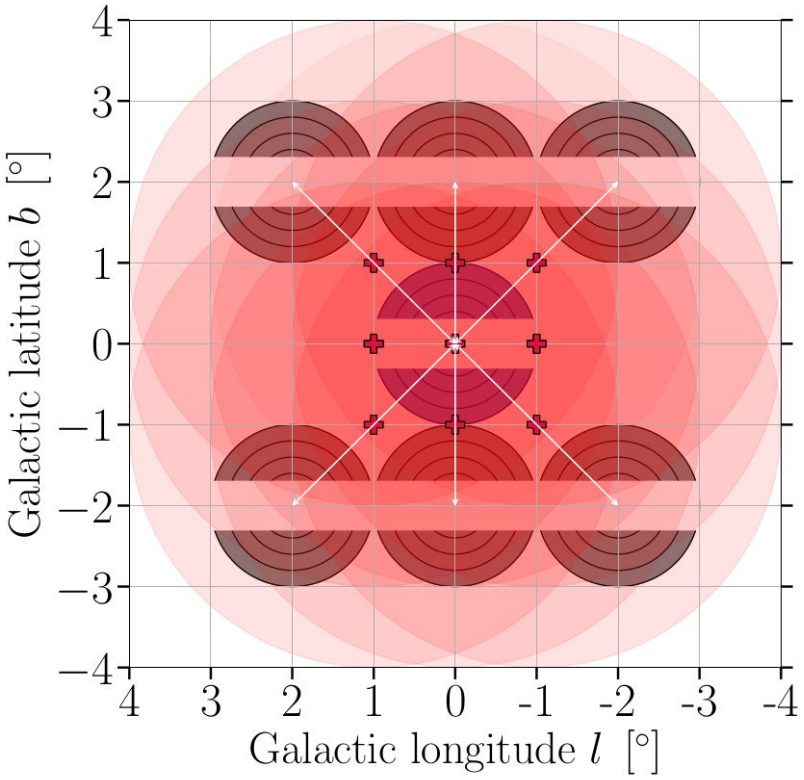

Figure 22 – Scheme of the spatial binning of the GC region as it will be implemented in the CTA's GC survey. The concentric disks around $(0, 0)$ are the ON regions with the exclusion mask $|b| \leq 0.3°$. The pointing positions are represented by crosses in $|b| = 1°$. The OFF regions are determined by the reflection of the ON regions relative to the pointing positions.

Source: CHERENKOV TELESCOPE ARRAY CONSORTIUM. (8)

Table 3 – Values of the J-factor and solid angle in each ROI considered in this work. The first column gives the ROI index. The second and the third ones give the inner and outer radius of the i-th disk in degrees, respectively. The fourth column gives the solid angle in steradian. The fifth column gives the J-factor in GeV^2 cm^{-5} for the Einasto model. (8)

i-th ROI	Inner radius [degree]	Outer radius [degree]	Solid angle $\Delta\Omega_i$ [10^{-4} sr]	J-factor $J\left(\Delta\Omega_i\right)$ [$10^{20}\,\mathrm{GeV}^2\ \mathrm{cm}^{-5}$]
1	0.3	0.4	0.22	2.87
2	0.4	0.5	0.46	5.16
3	0.5	0.6	0.66	6.36
4	0.6	0.7	0.87	7.35
5	0.7	0.8	1.06	7.89
6	0.8	0.9	1.25	8.41
7	0.9	1.0	1.44	8.74

Source: By the author.

of the CTA Observatory. In the case of IACTs, when the astrophysics sources are excluded, such as they are in the mask + disks methodology, the only background present is the events that consist of hadron shower events that are mistakenly classified as gamma-ray events. In the case that N_{OFF} is not measured, it can be estimated as

$$N_{OFFij} = T_{\text{obs}}\,\Delta\Omega_j \int_{\Delta E'_i} B_{\text{rate}}\,(E')\,dE', \tag{4.21}$$

where B_{rate} is the isotropic gamma-like background rate. Figure 23 shows the integrated background rate for logarithmic energy bins (five per decade) of the CTAO North and CTAO South arrays.

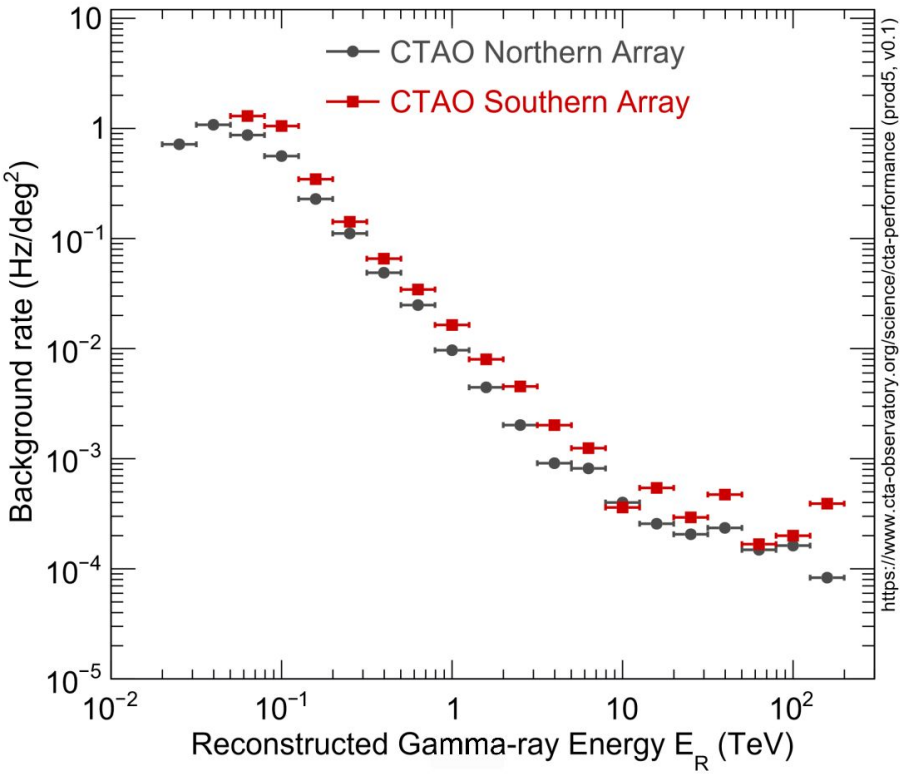

Figure 23 – Background rate of CTAO arrays North (black) and South (red). The background events rate is given in Hz degree^{-2} for five energy bins per decade.

Source: CHERENKOV TELESCOPE ARRAY CONSORTIUM. (133)

With all this information, it is possible to determine the 95% C.L. expected limits of exclusion on the annihilation cross-section of dark matter. A computer code, written in python 3, was developed to obtain the upper limits of $\langle\sigma\,v\rangle$ for different values of dark matter particle mass m_{DM}, using Eqs (4.19) and (4.20). To test the robustness of this code, the exclusion limits for the HESS and CTA telescopes for three primary channels, W^+W^-, $b\bar{b}$, and $\tau^+\tau^-$, were evaluated and compared with the official results of the collaborations.

Ensuring that the primary channel limits are consistent, the code could be further used to establish limits for a specific dark matter model.

For the limits obtained from the telescope HESS, ON and OFF counts from real data of 254 hours of observation were used. (146) Under the assumption that the HESS background rate remains the same, an extrapolation of this data to 546 hours was done, in order to match the observations of the 2014-2020 HESS Inner Galaxy Survey. (138) The HESS IRFs were extracted from Ref. (147) This HESS work (138) has not found any significant signal indicating possible dark matter annihilation in the GC. Using the profile likelihood method, they could exclude annihilation cross-sections near the thermal one, supposing an Einasto or NFW halo model. For CTA, the dataset was simulated using the updated IRFs that are publicly available on the CTA consortium website. (133) We use the more recent Alpha Configuration IRFs which can be downloaded through the file called *prod5 version v0.1*. In this case, 525 hours of observation are considered and the present results are compared with the official results in the 2021 CTA Consortium work. (8)

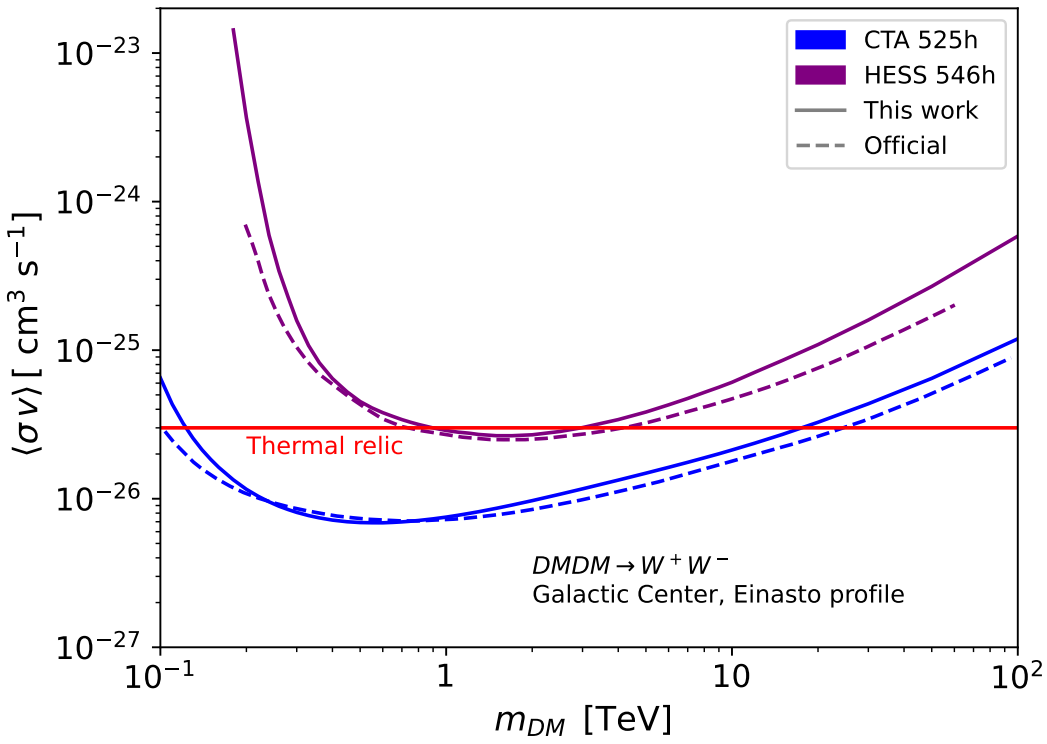

Figure 24 – Expected exclusion limits on the dark matter annihilation cross-section in the $\langle \sigma\, v \rangle \times m_{DM}$ space for the bosonic W^+W^- channel. The limits are shown for the HESS 546h of data (purple lines) and the projected performance of 525h of CTA (blue lines), both with the GC as the target. The results of this work (solid) and the official ones (dashed) are plotted together for comparison. The thermal relic cross-section $\langle \sigma\, v \rangle = 3 \times 10^{-26}\,\mathrm{cm}^3.\mathrm{s}^{-1}$ is shown in red. (6)

Source: By the author.

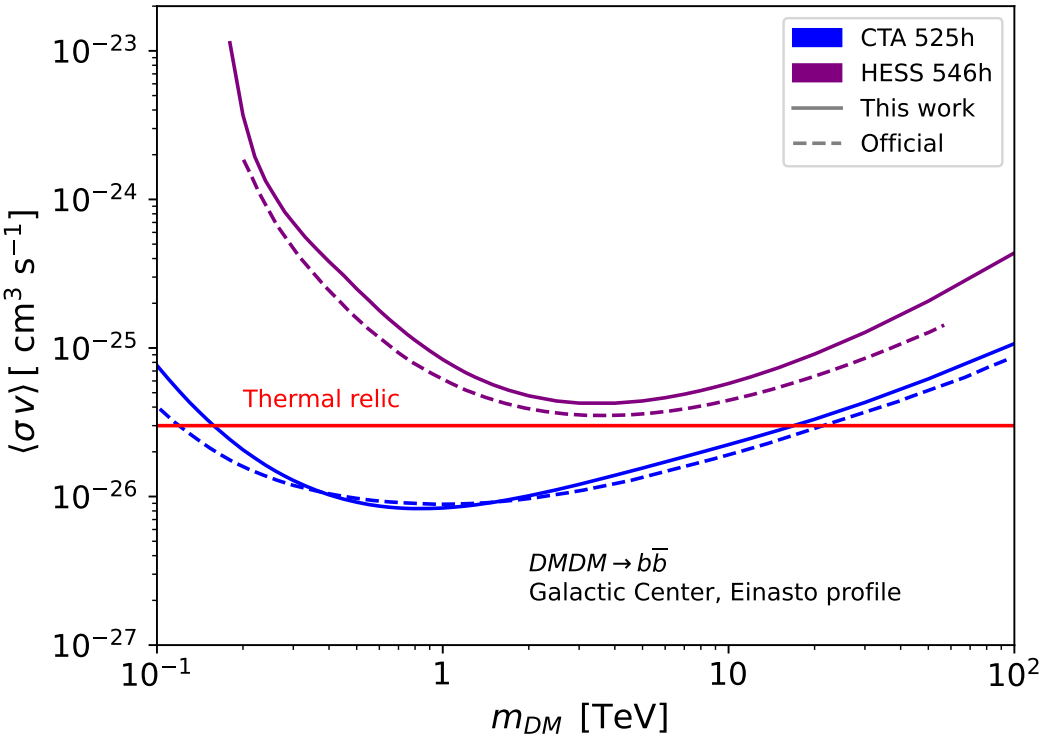

Figure 25 – Expected exclusion limits on the dark matter annihilation cross-section in the $\langle \sigma\, v \rangle \times m_{DM}$ space for the quark $b\bar{b}$ channel. The limits are shown for the HESS 546h of data (purple lines) and the projected performance of 525h of CTA (blue lines), both with the GC as the target. The results of this work (solid) and the official ones (dashed) are plotted together for comparison. The thermal relic cross-section $\langle \sigma\, v \rangle = 3 \times 10^{-26}\,\mathrm{cm}^3.\mathrm{s}^{-1}$ is shown in red. (6)

Source: By the author.

The upper limits on the cross-section $\langle \sigma\, v \rangle$ according to different values of mass m_{DM} for the channels W^+W^-, $b\bar{b}$, and $\tau^+\tau^-$ are shown in the Figures 24, 25, and 26, respectively. In each plot, the CTA limits are shown in blue and the HESS ones in purple. Only statistical expected limits were considered (no systematic errors). The Einasto (8) profile is always considered in this work and the PPPC 4 DM ID spectra (9) are used. It is possible to see that in all cases the results obtained in this work (solid lines) agree reasonably well with the official ones provided by the collaborations (dashed lines).

For the W^+W^- channel, HESS limits reach the WIMP thermal cross-section $\langle \sigma\, v \rangle = 3 \times 10^{-26}$ cm^3 s^{-1} around 1 TeV and CTA will be able to probe the thermal relic cross-section for masses between $\approx 0.1 - 10$ TeV, reaching 7×10^{-27} cm^3 s^{-1} at ≈ 0.6 TeV of dark matter mass. The $b\bar{b}$ channel provides weaker limits, as it is possible to see that HESS cannot probe the thermal cross-section for any mass. CTA, however, will be able to exclude a mass range similar to the W^+W^- channel, with the strongest limit of $\times 10^{-26}$ cm^3 s^{-1} around the TeV mass. The $\tau^+\tau^-$ channel provides the stringent limits among the ones considered here. For this channel, HESS limits surpass the thermal

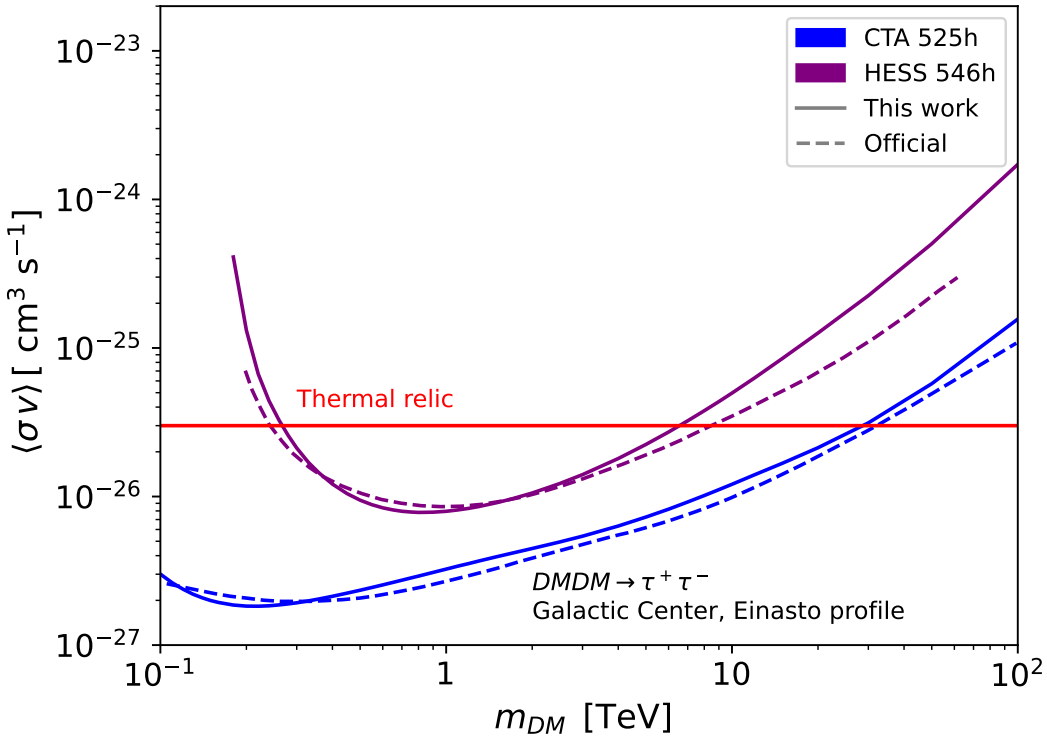

Figure 26 – Expected exclusion limits on the dark matter annihilation cross-section in the $\langle \sigma\, v \rangle \times m_{DM}$ space for the leptonic $\tau^+\tau^-$ channel. The limits are shown for the HESS 546h of data (purple lines) and the projected performance of 525h of CTA (blue lines), both with the GC as the target. The results of this work (solid) and the official ones (dashed) are plotted together for comparison. The thermal relic cross-section $\langle \sigma\, v \rangle = 3 \times 10^{-26}\,\mathrm{cm}^3.\mathrm{s}^{-1}$ is shown in red. (6)

Source: By the author.

cross-section, probing the thermal relic for masses in the $0.3 - 6\,\mathrm{TeV}$ range, while CTA will be able to exclude all the thermal relic cross-section for $m_{DM} \lesssim 30\,\mathrm{TeV}$. The two most important advances of the CTA Observatory compared to HESS are, firstly, the dark matter mass range that will be probed, extending the lower limit to 0.1 TeV, which is around 0.2 TeV for HESS. The other is that, for similar observation times, CTA will probe annihilation cross-sections one order of magnitude smaller, and almost two orders of magnitude for masses below 1 TeV. All these results show the promising capabilities of CTA in probing the annihilation cross-section of dark matter in the multi-TeV scale.

This chapter has presented a brief panorama of the techniques of gamma-ray astronomy and how it can be used in indirect dark matter searches. The kind of technology to be implemented to detect gamma rays depends on the energy range of interest. For heavy dark matter models, i.e., $m_{DM} \gtrsim 100\,\mathrm{GeV}$, Imaging Atmospheric Cherenkov Telescopes arrays are the most promising observatories. The log-likelihood ratio analysis was described for the analysis of gamma-ray signals from dark matter annihilation. The ON/OFF method for indirect detection of dark matter in the Galactic Center Region was

briefly presented. The limits of the currently working HESS and the future CTA telescopes were evaluated in order to validate the efficiency of the indirect detection limits code developed in this work. Now that the evaluation of indirect dark matter detection is established, this work will focus on a specific model of dark matter and obtain the indirect limits and complementary constraints to this model.

5 A MODEL FOR DARK MATTER: THE INERT DOUBLET MODEL

In this work, we review the viability of a specific model of dark matter in light of experimental constraints and theoretical considerations. The chosen model is known as the Inert Doublet Model (IDM) or Inert Two Higgs Doublet Model (I2HDM).

5.1 The construction of the IDM

The IDM is a minimal extension of the Standard Model scalar sector. Beyond the original Higgs doublet, we introduce a new doublet, with the same quantum numbers, but without couplings to the SM fermions (inertness). (88) (148) In the unitary gauge, these doublets are written as

$$H_1 = \frac{1}{\sqrt{2}} \begin{pmatrix} 0 \\ v + h(x) \end{pmatrix} \text{ and } H_2 = \begin{pmatrix} H^+ \\ (H + i\,A)/\sqrt{2} \end{pmatrix}. \tag{5.1}$$

This new doublet is composed of one complex field, that corresponds to the charged particles H^+ and $H^- = (H^+)^*$, and two neutral real fields, the CP-even scalar H and the CP-odd pseudo-scalar A. This doublet can be stabilized through a Z_2 discrete symmetry. A general Z_N symmetry means that the Lagrangian $\mathcal{L} = \mathcal{L}(\phi)$ of the theory must be invariant under a transformation given by

$$\phi \to e^{2\pi\, iX/N}\phi, \quad \mathcal{L} \to \mathcal{L}; \qquad \text{where} \quad X, N \in \mathbb{N}, X \leq N - 1. \tag{5.2}$$

For this Z_2 symmetry, the fields in H_2 are odd ($X = 1$) and all SM fields are even ($X = 0$). Being a new symmetry with a quantum number associated, the lightest particle among the odd fields must be stable, otherwise X would not be conserved. Moreover, if the stable particle is neutral, it can be a viable candidate for the dark matter particle. Either H or A could be this candidate, according to the hierarchy of the new particle masses. Nothing prohibits H^+ from being the lightest one, but, in this case, the IDM will not be useful as a model for the dark matter particle.

Including the additional doublet, the lagrangian of the scalar sector becomes

$$\mathcal{L}_S = (D_\mu H_1)^\dagger\, D^\mu H_1 + (D_\mu H_2)^\dagger\, D^\mu H_2 - V(H_1, H_2), \tag{5.3}$$

which includes the kinetic terms for the Higgs H_1 and the inert H_2 doublets, whose covariant derivative of the electroweak interaction is

$$D_\mu = \partial_\mu + \frac{i}{2} g_W \sigma_j W_\mu^j + \frac{i}{2} g' Y\, B_\mu, \tag{5.4}$$

where the second term relates to the $SU(2)_L$ group and the third one to $U(1)$, as described in Ref (149). These terms determine the couplings between the new particles and the EW gauge bosons, that represent important channels by which the IDM can be searched for.

The potential term, in turn, gives the masses of the scalars and the interactions between them. It reads

$$\begin{aligned} V(H_1,H_2) &= \mu_1^2|H_1|^2 + \mu_2^2|H_2|^2 + \lambda_1|H_1|^4 + \lambda_2|H_2|^4 \\ &+\lambda_3|H_1|^2|H_2|^2 + \lambda_4|H_1^\dagger H_2|^2 + \lambda_5 Re\left[\left(H_1^\dagger H_2\right)^2\right], \end{aligned} \tag{5.5}$$

where $\mu_1^2 < 0$ and parameters μ_2 and λ_i's are all real, which guarantees the CP symmetry of the scalar sector. (88) This term is also invariant under the Z_2 symmetry. The electroweak symmetry is spontaneously broken by the vacuum expectation value (VEV) of H_1 (see Refs. (88) and (150)),

$$\langle H_1 \rangle = \frac{v}{\sqrt{2}}, \tag{5.6}$$

where $v \equiv -\frac{\mu_1^2}{\lambda_1} = 246$ GeV. (151) The VEV of H_2, $\langle H_2 \rangle = 0$, does not change the spontaneous electroweak symmetry breaking due to the assumption $\mu_2^2 > 0$.

The parameters related to the Standard Model, μ_1 and λ_1, are determined by usual particle physics experiments, as the LHC, remaining five free parameters for the model: μ_2, λ_2, λ_3, λ_4 and λ_5. It is also useful to write the combined couplings λ_{345} and $\bar{\lambda}_{345}$ (also known as λ_L and $\bar{\lambda}_L$),

$$\lambda_{345} = \frac{1}{2}\left(\lambda_3 + \lambda_4 + \lambda_5\right), \quad \bar{\lambda}_{345} = \frac{1}{2}\left(\lambda_3 + \lambda_4 - \lambda_5\right). \tag{5.7}$$

Thus, the potential can then be rewritten as

$$\begin{aligned} V(H_1,H_2) = V(h) &+ \left(\mu_2^2 + \frac{\lambda_3}{2}v^2\right)H^+H^- + \frac{1}{2}\left(\mu_2^2 + \lambda_{345}v^2\right)H^2 + \frac{1}{2}\left(\mu_2^2 + \bar{\lambda}_{345}v^2\right)A^2 \\ &+\lambda_2\left(H^+H^-\right)^2 + \lambda_2\frac{H^4 + A^4}{4} + \lambda_2 H^+H^-H^2 + \lambda_2 H^+H^-A^2 + \lambda_2\frac{H^2A^2}{2} \\ &+\lambda_3 vhH^+H^- + \lambda_{345}vhH^2 + \bar{\lambda}_{345}vhA^2 \\ &+\frac{\lambda_{345}}{2}h^2H^2 + \frac{\bar{\lambda}_{345}}{2}h^2A^2 + \frac{\lambda_3}{2}h^2H^+H^-, \end{aligned} \tag{5.8}$$

from which the Feynman rules of the scalar interactions and the masses terms can be extracted. The masses of the scalar sector are, therefore, (152)

$$\begin{aligned} m_h^2 = 2\lambda_1 v^2,\ m_H^2 = \mu_2^2 + \lambda_{345}v^2, \\ m_A^2 = \mu_2^2 + \bar{\lambda}_{345}v^2, m_{H^\pm}^2 = \mu_2^2 + \frac{1}{2}\lambda_3 v^2. \end{aligned} \tag{5.9}$$

A similar expansion can be made on the kinetic term, which gives the couplings

between scalars and gauge bosons:

$$\begin{aligned}
&(D_\mu H_2)^\dagger (D^\mu H_2) = \\
&\frac{1}{2}\partial_\mu H \partial^\mu H + \frac{1}{2}\partial_\mu A \partial^\mu A + \partial_\mu H^+ \partial^\mu H^- + ieA_\mu \left(H^+\partial^\mu H^- - H^-\partial^\mu H^+\right) \\
&+\frac{g_Z}{2} Z_\mu \left(i\left(1-2\sin^2\theta_W\right) H^+\partial^\mu H^- - i\left(1-2\sin^2\theta_W\right) H^-\partial^\mu H^+ - H\partial^\mu A + A\partial^\mu H\right) \\
&+eg_Z A_\mu Z^\mu \left(1-2\sin^2\theta_W\right) H^+H^- + e^2 A_\mu A^\mu H^+H^- \\
&+g_Z^2 Z_\mu Z^\mu \left(\frac{(1-2\sin^2\theta_W)}{4} H^+H^- + \frac{(H^2+A^2)}{8}\right) \\
&+\frac{g_W}{2} W_\mu^+ \left(iH\partial^\mu H^- - iH^-\partial^\mu H - A\partial^\mu H^- + H^-\partial^\mu A\right) \\
&+\frac{g_W}{2} W_\mu^- \left(-iH\partial^\mu H^+ + iH^+\partial^\mu H - A\partial^\mu H^+ + H^+\partial^\mu A\right) \\
&+\frac{eg_W}{2} A_\mu W^{+\mu} \left(H^-H + iH^-A\right) \\
&+\frac{eg_W}{2} A_\mu W^{-\mu} \left(H^+H - iH^+A\right) \\
&-\frac{g_Z g_W}{2}\sin^2\theta_W Z_\mu W^{+\mu} \left(H^-H + iH^-A\right) \\
&-\frac{g_W g_W}{2}\sin^2\theta_W Z_\mu W^{-\mu} \left(H^+H - iH^+A\right) \\
&+g_W^2 W_\mu^+ W^{-\mu} \left(\frac{H^+H^-}{2} + \frac{H^2}{4} + \frac{A^2}{4}\right).
\end{aligned} \tag{5.10}$$

With the masses determined one can fix them according to the appropriate parameters and study the phenomenology that emerges from there. It is possible to see that through Eq. (5.9) the model can be reparameterized and the five independent variables are now $m_H, m_{H^\pm}, m_A, \lambda_{345}$ and λ_2, beyond the SM fixed parameters m_h (Higgs mass) and v (VEV).

The IDM provides three particles beyond the SM, but just the scalar H and the pseudoscalar A can be taken as the dark matter particle candidate, due to the neutral electric charge condition. For convention, here H is taken as the dark matter particle. This implies a mass hierarchy $m_{H^\pm}, m_A > m_H$ that will be considered hereafter. Another characteristic of the IDM is the impact of co-annihilation processes of the two partner particles, which will be significant for small mass-splittings, as explained in section 3.1. This motivates the reparameterization of this model to the masses basis, in the first place, and then to the mass-splittings.

5.2 Reparameterization of model

The model can be reparameterized to the masses and physical coupling basis $(\mu_2, \lambda_2, \lambda_3, \lambda_4, \lambda_5) \to (m_H^2, m_{H^\pm}^2, m_A^2, \lambda_{345}.\lambda_2)$:

$$\mu_2^2 = m_H^2 - \lambda_{345} v^2 > 0 \tag{5.11}$$

$$\lambda_3 = 2\lambda_{345} + \frac{2\left(m_{H^\pm}^2 - m_H^2\right)}{v^2} \tag{5.12}$$

$$\lambda_4 = \frac{m_A^2 + m_H^2 - 2m_{H^\pm}^2}{v^2} \tag{5.13}$$

$$\lambda_5 = \frac{m_H^2 - m_A^2}{v^2}. \tag{5.14}$$

It is useful to define the mass-splittings as

$$\Delta_+ = m_{H^\pm} - m_H, \tag{5.15}$$

$$\Delta_o = m_A - m_H. \tag{5.16}$$

Making a change to the basis $(m_H, \Delta_+, \Delta_o, \lambda_{345}, \lambda_2)$ one obtains, finally,

$$\lambda_3 = 2\lambda_{345} + \frac{2\Delta_+\left(2m_H + \Delta_+\right)}{v^2}, \tag{5.17}$$

$$\lambda_4 = \frac{\Delta_o\left(2m_H + \Delta_o\right) - 2\Delta_+\left(2m_H + \Delta_+\right)}{v^2}, \tag{5.18}$$

$$\lambda_5 = -\frac{\Delta_0\left(2m_H + \Delta_0\right)}{v^2}, \tag{5.19}$$

$$\bar{\lambda}_{345} = \lambda_{345} + \frac{\Delta_0\left(2m_H + \Delta_0\right)}{v^2}. \tag{5.20}$$

In the following, we discuss the theoretical constraints that these parameters must satisfy in the current parameterization.

5.3 Theoretical constraints

This model has to obey certain constraints that come from theoretical reasons. (152) In this section, we cite these conditions and give some necessary or sufficient conditions in scenarios where $m_{H^\pm}, m_A > m_H$ in the $(m_H, \Delta_+, \Delta_o, \lambda_{345}, \lambda_2)$ parameterization.

5.3.1 Electroweak vacuum stability

To ensure the electroweak vacuum stability (88), the λ's parameters have to obey:

$$\lambda_1 > 0,\ \lambda_2 > 0,\ \lambda_3 > -2\sqrt{\lambda_1\lambda_2}, \quad \lambda_3 + \lambda_4 - |\lambda_5| > -2\sqrt{\lambda_1\lambda_2},\ \lambda_4 - |\lambda_5| < 0. \tag{5.21}$$

We use that λ_1 is a known SM parameter and verify

$$\lambda_1 = \frac{m_h^2}{2v^2} \approx \frac{1}{2}\left(\frac{125\,\mathrm{GeV}}{246\,\mathrm{GeV}}\right)^2 \approx 0.129,. \tag{5.22}$$

For positive mass-splittings, $\lambda_3 > 2\lambda_{345}$, in such a way that a sufficient condition for the third stability inequality is

$$\lambda_{345} > -\sqrt{\lambda_1\lambda_2}. \tag{5.23}$$

One can just adopt the simpler condition

$$\lambda_{345} > 0. \tag{5.24}$$

For the fourth inequality we use $\lambda_5 < 0$ for $\Delta_o > 0$, which implies

$$\lambda_3 + \lambda_4 - |\lambda_5| = 2\lambda_{345} > -2\sqrt{\lambda_1 \lambda_2}, \tag{5.25}$$

that also is filled by (5.24). The last relation is automatically guaranteed by the mass hierarchy.

5.3.2 Perturbative unitarity constraints

To guarantee the validity of the perturbative limit, the couplings must be small enough to allow the series convergence of $2 \to 2$ diagrams. As shown in (88) and (153), the eigenvalues of the scattering matrix must be $|c_i| < 8\pi$. These coefficients are combinations of the λ_i parameters and read (88)

$$c_{1,2} = \lambda_3 \pm \lambda_4, \quad c_{3,4} = -3\left(\lambda_1 + \lambda_2\right) \pm \sqrt{9\left(\lambda_1 - \lambda_2\right)^2 + \left(2\lambda_3 + \lambda_4\right)^2}, \tag{5.26}$$

$$c_{5,6} = \lambda_3 \pm \lambda_5, \quad c_{7,8} = -\left(\lambda_1 + \lambda_2\right) \pm \sqrt{\left(\lambda_1 - \lambda_2\right)^2 + \lambda_4^2}, \tag{5.27}$$

$$c_{9,10} = \lambda_3 + 2\lambda_4 \pm 3\lambda_5, \quad c_{11,12} = -\left(\lambda_1 + \lambda_2\right) \pm \sqrt{\left(\lambda_1 - \lambda_2\right)^2 + \lambda_5^2}. \tag{5.28}$$

The usual approach is to consider $|\lambda_i| < 8\pi$ or even a smaller superior limit (e.g., in (154) it is considered $|\lambda_i| < 1$). But in present parameterization m_H, Δ_+, Δ_o and λ_{345} must be upper limited. As far as these conditions depend on Δ_+ and Δ_o, the superior values of λ_{345} and m_H change according to it. Despite this, it is possible to choose ranges for λ_{345} and m_H conservative enough to satisfy conditions (5.26) - (5.28) for almost all parameter space.

It is possible to substitute Eqs. (5.26) - (5.28) by sufficient conditions that do not depend on the λ_2 coupling. Moreover, some of these relations are redundant in the considered mass hierarchy. The new conditions, which satisfy the previous ones, in the current parameterization are

$$2\lambda_{345} + \frac{\Delta_o\left(2m_H + \Delta_o\right)}{v^2} < 8\pi, \tag{5.29}$$

$$2\lambda_{345} + \frac{4\Delta_+\left(2m_H + \Delta_+\right) - \Delta_o\left(2m_H + \Delta_o\right)}{v^2} < 8\pi, \tag{5.30}$$

$$4\lambda_{345} + \frac{\Delta_o\left(2m_H + \Delta_o\right) + 2\Delta_+\left(2m_H + \Delta_+\right)}{v^2} < 8\pi\sqrt{1 + \frac{3\lambda_1}{4\pi}}, \tag{5.31}$$

$$2\lambda_{345} + \frac{\Delta_o\left(2m_H + \Delta_o\right) + 2\Delta_+\left(2m_H + \Delta_+\right)}{v^2} < 8\pi, \tag{5.32}$$

$$\left|\frac{\Delta_o\left(2m_H + \Delta_o\right) - 2\Delta_+\left(2m_H + \Delta_+\right)}{v^2}\right| < 8\pi\sqrt{1 + \frac{\lambda_1}{4\pi}}, \tag{5.33}$$

$$2\lambda_{345} + \frac{5\Delta_o\left(2m_H + \Delta_o\right) - 2\Delta_+\left(2m_H + \Delta_+\right)}{v^2} < 8\pi, \tag{5.34}$$

$$\frac{\Delta_0\left(2m_H + \Delta_0\right)}{v^2} < 8\pi\sqrt{1 + \frac{\lambda_1}{4\pi}}. \tag{5.35}$$

Besides, it is possible to determine an upper bound to λ_{345} which will be used for further scans. This comes from inequality (5.31) (condition from $c_{3,4}$). In the limit $\Delta_o, \Delta_+ \to 0$, one obtains

$$\lambda_{345} < 2\pi, \tag{5.36}$$

which, together Eq. (5.24), provide the range of scan for λ_{345}.

5.4 Experimental constraints

Some collider experiments, especially the Large Electron-Positron Collider (LEP) and the Large Hadron Collider (LHC), provide constraints to the IDM, acting in complement to the previous theoretical constraints. In this section, we will explore some of them in more detail.

5.4.1 Electroweak precision data from LEP

Measurements from LEP of electroweak precision data establish limits to the scalar sector masses that make the decay of Z and W bosons kinetically forbidden for the channels $W^+ \to H\,H^+$, $A\,H^+$ and $Z \to H\,A$, $H^+\,H^-$ (88):

$$\begin{aligned} m_H + m_{H^\pm} > m_{W^\pm}, \quad m_A + m_{H^\pm} > m_{W^\pm} \\ m_H + m_A > m_Z, \quad m_{H^\pm} > \frac{m_Z}{2}. \end{aligned} \tag{5.37}$$

These conditions strongly constrain the parameters for $m_H, m_{H^\pm}, m_A \lesssim 100\,\text{GeV}$, while are trivially fulfilled for higher masses.

5.4.2 Electroweak precision test

Models of physics beyond the SM must respect data from Electroweak Precision Tests (EWPT). The parameters S, T and U, proposed by Peskin and Takeuchi (155), parameterize contributions from new physics to electroweak radiative corrections. For this model (156), S and T parameters are given by

$$S = \frac{1}{72\pi\left(x_2^2 - x_1^2\right)^3}\left[x_2^6 f_a\left(x_2\right) - x_1^6 f_a\left(x_1\right) + 9x_2^2x_1^2\left(x_2^2 f_b\left(x_2\right) - x_1^2 f_b\left(x_1\right)\right)\right] \tag{5.38}$$

and

$$T = \frac{1}{32\pi^2\alpha v^2}\left[f_c\left(m_{H^\pm}^2, m_A^2\right) + f_c\left(m_{H^\pm}^2, m_H^2\right) - f_c\left(m_A^2, m_H^2\right)\right], \tag{5.39}$$

where

$$x_1 = \frac{m_H}{m_{H^\pm}}, \quad x_2 = \frac{m_A}{m_{H^\pm}}, \tag{5.40}$$

and the functions f_a and f_b are given by

$$f_a(x) = -5 + 13\log(x), \quad f_b(x) = 3 - 4\log(x), \tag{5.41}$$

and

$$f_c(x,y) = \begin{cases} \frac{x+y}{2} - \frac{x\,y}{x-y}\log\left(\frac{x}{y}\right), & x \neq 0 \\ 0, & x = y \end{cases}. \tag{5.42}$$

Taking $m_h = 125\,\text{GeV}$ and $U = 0$, the best fit for S and T is (157)

$$S = 0.06 \pm 0.09, \quad T = 0.1 \pm 0.07. \tag{5.43}$$

According to (88) just not too large mass-splittings $\Delta_+, \Delta_o \lesssim 100\,\text{GeV}$ are allowed by this data. (88)

5.4.3 LHC Higgs decay data

Several studies of LHC data analyze the decay of the SM Higgs into non-SM particles from new physics, i.e., $h \to$ invisible. (152) They could be, for instance, $h \to H\,H$, if $m_H < m_h/2$. (88) The rate of new particles production from decay can then be bounded by the Particle Data Group limit (151)

$$BR(h \to \text{invisible}) < 0.11, \tag{5.44}$$

which provides a strong constraint in the low mass regime ($m_H < m_{W^\pm}, m_Z$) of the model.

5.5 The Inert Doublet Model as dark matter

The previous sections have discussed the theoretical framework and constraints of the IDM. This section focuses on how the IDM can provide a viable dark matter particle candidate and the observables that can be probed by astrophysical experiments. The dark matter particle candidate was taken as the scalar H, but choosing H or A as dark matter does not change the phenomenology of the model: it just exchanges the couplings $\lambda_{345} \leftrightarrow \overline{\lambda}_{345}$. Let us keep this choice. Concerning the thermal production of dark matter, the unstable particles A and $H^\pm$ must have decayed at the actual time but, in the Early Universe, they could participate in co-annihilation processes that can play an important role in the freeze-out mechanism of thermal production. The current abundance is well known by the Planck satellite measurements of CMB as being $\Omega\,h^2 = 0.1200 \pm 0.0012$ (7) and must be obtained by possible scenarios of the model. Direct detection also provides another important constraint of the IDM, which, in this model, provides a direct constraint in the $\lambda_{345} \times m_H$ parameter space. Another search complementary to the last ones is indirect detection which will be the principle search investigated in this work.

The following subsections detail the observables probed by these three kinds of astrophysical constraints: DD, ID, and relic abundance. In this work, just the tree-level

contributions are taken into account, as a first-order approximation. This makes the quartic parameter λ_2 not important in present analyses because it just enters in four non-Standard Model vertices, as seen in Eq. (5.8). This coupling does matter on the loop-level since H can rescatter before the annihilation process. This was analyzed in Ref. (158) which showed that λ_2 could impact up to 20% of some cross-sections and as a consequence change the relic abundance. Despite this shortcoming, the treatment in this work can be considered as a limit $\lambda_2 \to 0$ which still can lead to interesting results.

5.5.1 WIMP-nucleon scattering in the IDM

The IDM can be constrained using direct detection experiments. The particle H in the local dark matter distribution can interact with protons or neutrons of some inert gas and transfer energy in a spin-independent scattering process. This is able through two possible channels: a H particle and a q quark exchange a Higgs boson h, or, these particles exchange a Z boson producing a A particle. The last process is already excluded by experiments (150), but the first one is still viable. In this case, at tree level, the WIMP-nucleon scattering cross-section is (159) (156)

$$\sigma_{H-N} = \frac{\lambda_{345}^2 v^2}{m_h^4} \frac{f_N^2 m_N^2}{\left(m_H + m_N\right)^2}, \tag{5.45}$$

where m_N is the nucleon mass (proton or neutron) and f_N^2 is the squared form factors for a given nucleon. (159) Figure 27 shows the diagrams of these channels of direct detection.

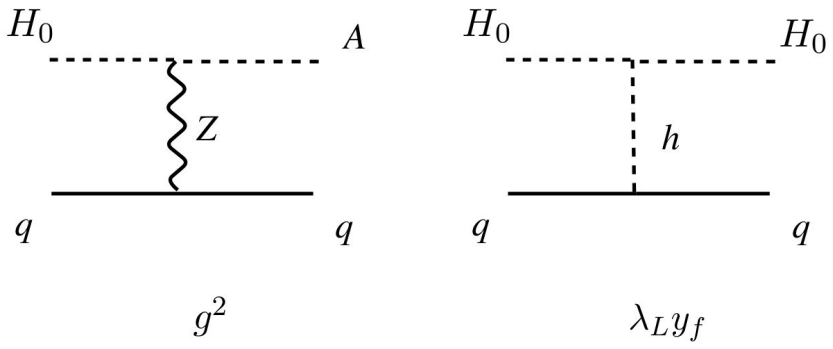

Figure 27 – Main channels of direct detection for the Inert Doublet Model.

Source: Adapted from TYGAT *et al.* (150)

The expression for the cross-section (5.45) depends only on λ_{345} and m_H, not on $m_{H^\pm}$ or m_A. This implies that experimental constraints on the $\sigma_{SI} \times m_H$ space from direct detection experiments are mapped to constraints on the $\lambda_{345} \times m_H$ parameter space.

5.5.2 Annihilation processes in the IDM

In the IDM, the dark matter particle can self-annihilate in three main kinds of channels:

- 1) Vector bosons: $HH \to W^+W^-, \quad HH \to ZZ$.
- 2) Higgs bosons: $HH \to hh$.
- 3) Fermions through the Higgs portal: $HH \to h \to f\bar{f}$.

For the EW boson states, annihilation can occur through a four-vertex $HHV\overline{V}$ interaction, a s-channel mediated by the Higgs boson h, and t-channel or u-channel mediated by the other two non-SM particles, A for Z and $H^\pm$ for $W^\pm$. The two Higgs hh states can be produced through analogous processes: a 4-vertex $HHhh$, a s Higgs h-mediated channel, and the t and u non-Standard Model Higgs H-mediated channels. Due to the Z_2 symmetry, the only possible channel for fermionic states is through the s-channel mediated by the Higgs boson h (known as the Higgs portal, see Refs. (152) and (150)). The diagrams of the main annihilation processes are represented in Figure 28 with the respective associated couplings.

Making the non-relativistic limit expansion of the dark matter annihilation cross-section times velocity (see E. (3.36)), its analytic expressions are given by (152) (159)

$$\langle \sigma\, v\rangle_{2SM} = \langle \sigma\, v\rangle_{W^+W^-} + \langle \sigma\, v\rangle_{ZZ} + \langle \sigma\, v\rangle_{hh} + \sum_f \langle \sigma\, v\rangle_{f\bar{f}}\,, \tag{5.46}$$

$$\langle \sigma\, v\rangle_{f\bar{f}} = \frac{N_c}{4\pi}\frac{\lambda_{345} m_f^2}{\left(4m_H^2 - m_h^2\right)^2}\left(1 - r_f\right)^{\frac{3}{2}}, \tag{5.47}$$

$$\langle \sigma\, v\rangle_{hh} = \frac{1}{64\pi}\frac{\lambda_{345}^2}{m_H^2}\left[1 + \frac{3m_h^2}{4m_H^2 - m_h^2} + \frac{2\,\lambda_{345} v^2}{m_h^2 - 2m_H^2}\right]^2 \sqrt{1 - r_h}, \tag{5.48}$$

and

$$\langle \sigma\, v\rangle_{VV} = \frac{m_H^2}{2\,\delta_V \pi v^4}\left[\left(1 + \frac{\lambda_{345} v^2}{4m_H^2 - m_h^2}\right)\left(1 - r_V + \frac{3}{4}r_V^2\right) + \frac{4m_H^4}{\left(m_H^2 + m_{\phi_V}^2 - m_V^2\right)^2}\left(1 - r_V\right)^2 - \frac{2m_H^2}{m_H^2 + m_{\phi_V}^2 - m_V^2}\left(1 + \frac{\lambda_{345} v^2}{4m_H^2 - m_h^2}\right)\left(2 - 3r_V + r_V^2\right)\right]\sqrt{1 - r_V}, \tag{5.49}$$

where we define

$$r_x = \frac{m_x^2}{m_H^2}, \quad \delta_{W(Z)} = 1\,(2)\,, \quad m_{\phi_{W^\pm(Z)}} = m_{H_\pm(A)}. \tag{5.50}$$

These approximations are not valid at the freeze-out time. (152) In this case, the thermal distribution and co-annihilation play a role in the determination of $\langle \sigma\, v\rangle_{\text{eff}}$. For

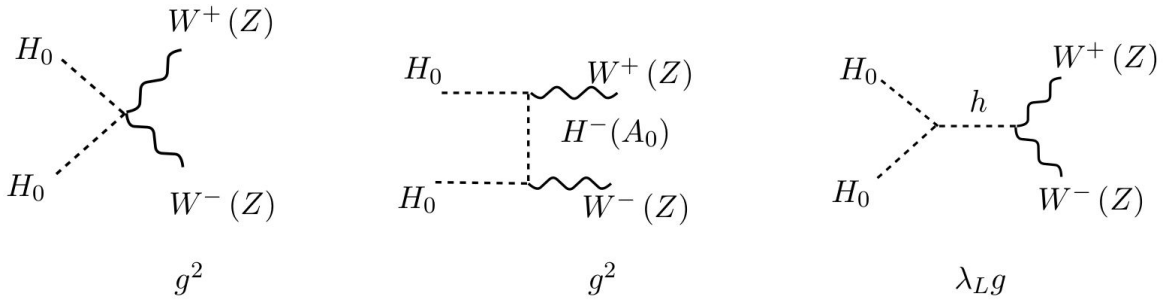

(a) Vector bosons channel of annihilation.

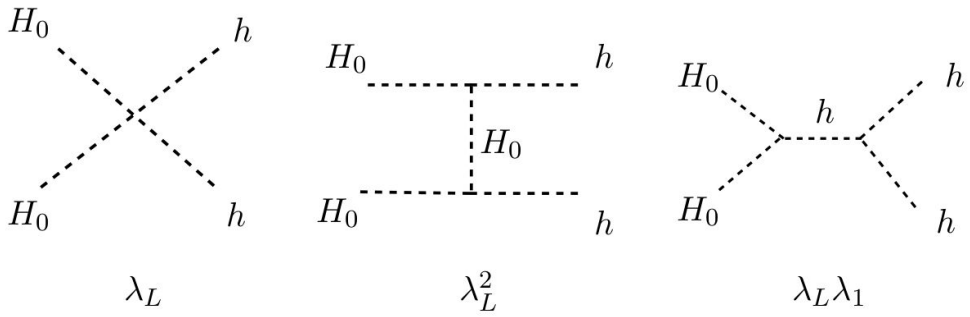

(b) Two Higgs channel of annihilation.

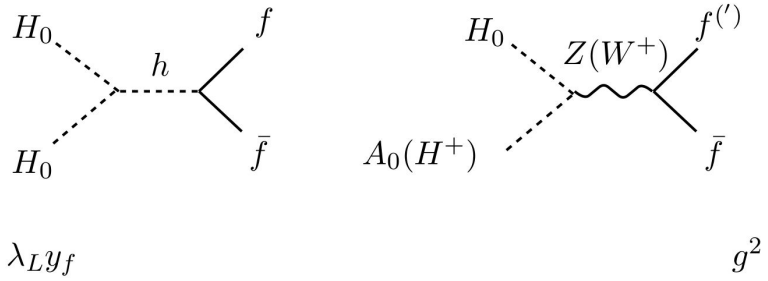

(c) Fermions channel of annihilation.

Figure 28 – Diagrams of the main channels of annihilation for the Inert Doublet Model and the respective couplings. Each row corresponds to one kind of channel: (a) vector bosons final state, (b) two Higgs final state, and (c) fermions state.

Source: TYGAT *et al.* (150)

that, we use the numerical softwares CalcHEP, which evaluates matrix elements, and micrOMEGAs 5.3.35 (160), which evaluates the thermal average of cross-section given by Eq. (3.61) and solves numerically the Boltzmann Equation to determine the relic abundance. The formalism of the Boltzmann Equation and co-annihilation was discussed

in detail in section 3.1.

The expressions (5.47) - (5.49) also show that, for fixed values of $m_{H^\pm}$ and m_A, the total annihilation cross-section times velocity is a function only on m_H and λ_{345}, what will enable a straight comparison between DD and ID limits. The fact that both $\langle \sigma\, v \rangle_{2SM}$ and σ_{H-N} observables depend only on these two variables (for fixed mass-splittings) enables us to compare directly DD and ID limits, which is a usual feature of minimal extensions of the Standard Model. After discussing the ID and DD observables, we will look to another astrophysical constraint: the measured relic abundance of dark matter in our universe.

5.5.3 Relic abundance in the IDM

As said before, the present work uses only tree-level calculations to evaluate cross-sections and solve the Boltzmann Equation in order to obtain the dark matter relic abundance for different IDM scenarios. The effects of loop-level can be important in some cases and could be conferred in Ref. (158). One can assign different combinations of $(m_H, m_{H^\pm}, m_A, \lambda_{345})$ and put them as inputs to micrOMEGAs and obtain as return the evaluated relic abundance (micrOMEGAs takes $\lambda_2 = 0.01$). A scan for masses m_H in the range $10 - 10,000\,\text{GeV}$, $\Delta_+, \Delta_o = 1, 100\,\text{GeV}$ and $\lambda_{345} = 1, 10^{-1}, 10^{-2}$ and 10^{-3} was made and the abundance evaluated by micrOMEGAs in each case as shown in Fig. 29. (For $\Delta_+, \Delta_o = 100\,\text{GeV}$ the dark matter mass is upper bound to 1000 GeV to ensure unitarity.)

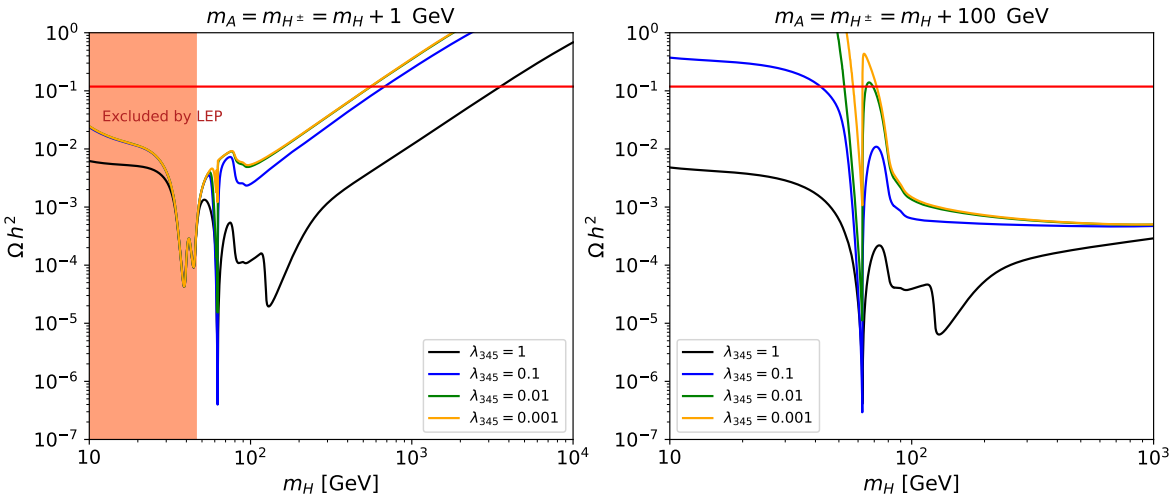

Figure 29 – Relic abundance for a scan on the $\lambda_{345} \times m_H$ space. On the left (right) panel is shown the scan for the low (high) mass-splitting regime (i.e., $\Delta_+ = \Delta_o = 1\,(100)$ GeV). The observed relic abundance $\Omega\, h^2 = 0.1200 \pm 0.0012$ (7) is shown in solid red line. The dark matter masses are in the range $10 - 1000\,\text{GeV}$ and the coupling $\lambda_{345} = 1, 10^{-1}, 10^{-2}$ and 10^{-3} (solid black, blue, green and yellow lines).

Source: Adapted from BELYAEV *et al.* (88)

This scan was previously made in Ref. (88) and (152) where it was analyzed in

detail. In the following, we give a brief analysis of their results. In both mass-splitting limits, the dark matter abundance versus dark matter mass curves is dominated by a resonance around $m_H = m_h/2$. This occurs because the dominant processes at $m_H < m_h$ is $HH \to h \to b\bar{b}$ through the Higgs portal, given that the coupling to the Higgs is proportional to the fermion mass. For the low mass-splitting regime, the production of a gauge boson is relevant at $m_H = m_{W^\pm,Z}/2$, also generating resonances. Nevertheless, it is important to say that LEP constraints (5.37) already excludes masses below $m_H < m_{W^\pm,Z}$ for the low mass-splitting case. Further resonances are found when the two EW gauge bosons channels are open at $m_H = m_{W^\pm,Z}$ and for the two Higgs one at $m_H = m_h$. The slop at $m_H > m_t$ is dominated by the $t\bar{t}$-Higgs portal channel. For high mass-splittings ($\Delta m >> 10\,\text{GeV}$), the observed abundance is obtained near the $m_H \approx m_h/2$ resonance. It is possible to see that for low mass-splittings, due to co-annihilation processes that are significant at $\Delta m < 10\,\text{GeV}$ (see section 3.1), the correct relic abundance is obtained at high masses, approximately $m_H > 500\,\text{GeV}$, characterizing what is called the "high-mass regime". These considerations motivate the interest in very low mass-splittings $\Delta \leq 10\,\text{GeV}$ to explore the high-mass regime $m_H > 500\,\text{GeV}$.

In this chapter, we reviewed the construction and phenomenology of the Inert Doublet Model and its viability as a dark matter model. With its parameters, the theoretical and experimental constraints were shown and the processes for dark matter direct and indirect detection were briefly discussed. The evaluation of relic abundance by numerical software was made for some cases, where it was checked the presence of two mass regimes, the low-mass regime and the high-mass regime. The first one is already very bound by collider data and is not the interest here. In the high-mass regime, the model is characterized by the presence of co-annihilation. This feature will be important to enhance the annihilation cross-section that is probed in indirect detection searches. This will be the target of the next chapter.

6 LIMITS TO THE INERT DOUBLET MODEL

After discussing the theoretical construction of IDM and existing constraints, this chapter deals with the scans in the parameter space and the extraction of new restrictions coming from indirect detection methods using gamma rays. As shown in subsection 5.5.3, there are two regimes where the observed relic abundance $\Omega h^2 = 0.1200 \pm 0.0012$ (7) is obtainable: the low-mass regime ($m_H \lesssim m_W, m_Z$) and the high-mass regime ($m_H \gtrsim 500\,\mathrm{GeV}$). The low-mass regime is already strongly constrained by collider and direct detection data, see for instance (88) and (150). The intermediate-mass range ($m_W, m_Z < m_H < 500\,\mathrm{GeV}$) is excluded by relic abundance because it is very suppressed by annihilation into the gauge bosons (154). The high-mass regime can only yield the right abundance if the mass-splittings are very small ($\Delta_{o,+} \lesssim 10\,\mathrm{GeV}$). In this case, the thermal production of dark matter is dominated by co-annihilation effects, as seen in subsection 3.1.4. The co-annihilation regime establishes that the dark matter annihilation cross-section must be higher than the typical WIMP one, providing the same dark matter abundance. This means that the gamma-ray flux from annihilation in the IDM is also higher than usually expected, making indirect detection a very promising detection method.

The high-mass regime was deeply investigated in the 2016 work by Queiroz and Yaguna (154) where the authors analyzed the contributions of co-annihilation channels to the relic abundance and the main relevant channels to dark matter annihilation in the IDM, which were found to be the boson states W^+W^-, ZZ and hh. They also selected the scenarios that satisfy all theoretical, collider (see sections 5.3 and 5.4), direct detection, and relic abundance constraints. The results of Queiroz and Yaguna have shown a strong potential of the CTA in probing the IDM in the Galactic Center region, excluding almost all scenarios. In another study, Garcia-Cely and Ibarra (161) have made a detailed analysis of the annihilation gamma-ray signal for the IDM taking into account the Sommerfeld enhancement and other channels, the VIB γW^+W^- channel and the loop-level gamma lines $\gamma\gamma$ and γZ. The effect of the Sommerfeld enhancement is basically to increase the annihilation cross-section, making the indirect detection probing even more sensitive to the IDM. The key results of these two works are equivalent. These two studies used the CTA's sensitivity expected according to the Array I Configuration (3 LSTs, 18 MSTs and 56 SSTs). They also used a morphological analysis of the Galactic Diffuse Emission (GDE) with systematic errors for 100h and 500h of observation, as described in Refs (162) and (163). In both studies, the Einasto profile was considered for the GC region. The sensitivity of CTA to the IDM for dwarf galaxies was projected by Duangchan *et al.* (159), where was found that Draco and Sculptor do not provide limits strong enough to

probe the IDM thermal cross-section. They also fixed the mass-splittings Δ_+ and Δ_o for a benchmark, which enables comparing direct and indirect detection experiments in the $\langle \sigma\, v \rangle \times m_{DM}$ space. The main results for these indirect detection studies are shown in Figure 30.

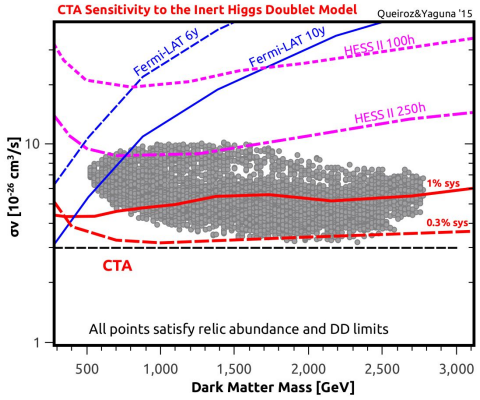

(a) Sensitivity of Fermi-LAT (blues line), HESS (magenta line) and CTA (red line) for the W^+W^- channel at the GC and the relic abundance points of the IDM.

Source: QUEIROZ; YAGUNA. (154)

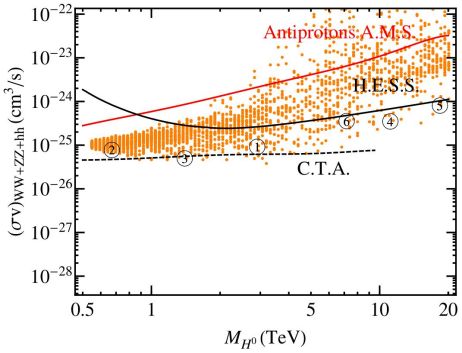

(b) Sensitivity of HESS (black solid line), CTA (black dashed line) and antiprotons AMS (red line) at the GC to the IDM considering the Sommerfeld enhancement for the main bosonic channels.

Source: GARCIA-CELY; GUSTAFSSON; IBARRA.(161)

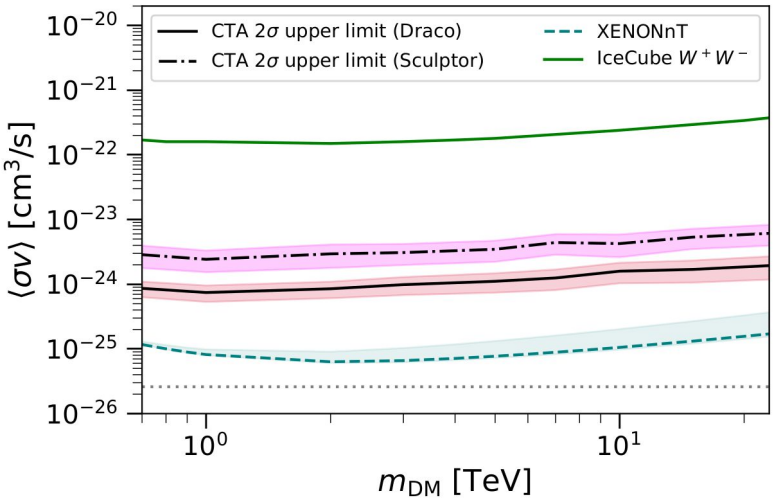

(c) Complementary limits in terms of annihilation cross-section $\langle \sigma\, v \rangle$ from the projected CTA sensitivity at the dwarf galaxies Draco and Sculptor compared with projected XENONnT and IceCube.

Source: DUANGCHAN *et al.* (159)

Figure 30 – Indirect detection exclusion limits to the IDM in the annihilation cross-section times velocity versus dark matter mass space for different experiments and targets.

Nevertheless, these results must be updated for the following experimental reasons:

1) The CTA's instrument response functions have been updated in the last few years and the new limits from 525h of observation must be checked. 2) HESS has been taking more data since then and the current 546h limits (138) could potentially exclude part of the available scenarios. 3) XENONnT first results have been published recently, making direct detection limits stronger than older ones. (110)

The present study adopts an approach with the following premises:

- Consider the more updated experimental and instrumental results from direct detection and indirect detection. For that, we use the last updated IRFs for CTA, *prod5 version v0.1* (Alpha Configuration), and 525h of observation of the GC to estimate the CTA sensitivity. For HESS, recent 546h data of HESS observation at GC is used. (138) In both cases the Einasto (2) profile is considered. For direct detection limits, the 1.09 t.y exposure data of XENONnT experiment is used. (110)

- The previous studies of indirect detection limits to the IDM have considered a morphological analysis of the astrophysical emission near the GC. In this work, the Ring method is used, where the GR is masked and a 2D-binned analysis is performed and just statistic errors are considered, just as implemented in chapter 4. That method is very promising once it contours the astrophysical uncertainties.

- Consider only tree-level processes in the IDM. With that, numerical calculations of processes are made with the *micrOMEGAs 5.3.35* software. (164) Neither Sommerfeld enhancement nor gamma lines are considered in this work.

The following sections deal with the methodology used to perform scans in the parameter space of the IDM and present the bounds from theoretical constraints, relic abundance, and direct detection. After that, the exclusion limits of indirect detection will be evaluated in the model-dependent approach, from the current data of HESS and simulations of the CTA performance. With all this information, it will be possible to determine the scenarios where the IDM is still a viable dark matter model according to actual data and the ones that will be probed by CTA in the future.

6.1 Methodology

In this study, two scans in the parameter space $(m_H, \Delta_+, \Delta_o, \lambda_{345})$ have been performed to obtain samples of possible scenarios of the IDM. The first scan was generated by a random sampling of these parameters to determine the points in the $\langle \sigma\, v \rangle \times m_H$ space that provide the correct relic abundance together with the theoretical, collider, and direct detection constraints. Evaluating the indirect detection limits for all the parameter space of the IDM is very expensive computationally. For that reason, a second scan is

made by selecting some benchmarks that will be used to determine the limits of indirect detection with gamma-rays. Both scans use the following parameter ranges:

$$\begin{gathered} 0 < \lambda_{345} < 2\pi, \\ 300\,\mathrm{GeV} < m_H < 30,000\,\mathrm{GeV}, \\ 0.5\,\mathrm{GeV} < \Delta_+ < 10\,\mathrm{GeV}, \\ 0.5\,\mathrm{GeV} < \Delta_o < 10\,\mathrm{GeV}. \end{gathered} \tag{6.1}$$

As said before, the only parameter of the model that remains fixed is λ_2 because this coupling only enters in loop-level interactions between the non-Standard Model particles (see Equation (5.8)).

Once the scenarios are generated, the constraints discussed in the previous chapter must be applied to the sample. In the ranges displayed in Eq. (6.1) vacuum stability, LEP electroweak precision data, and LHC Higgs decay are automatically preserved. It was checked that these ranges agree with EWPT parameters S and T within 1 and 2 standard deviations of containment, respectively. Next, we closely follow the steps by Belyaev *et al.* (88) where the remaining constraints are used as subsequent cuts in the parameter space. They are:

- Cut-1) constraints from unitarity (Eqs. (5.29) - (5.35)), which basically put upper bounds on λ_{345} and m_H, and inertness, i.e., $\mu^2 = m_H^2 - \lambda_{345} v^2 > 0$;
- Cut-2) constraint from the measured relic abundance of dark matter by the Planck satellite (7) $\Omega\, h^2 = 0.1200 \pm 0.0012$;
- Cut-3) upper limits at 90 % C.L. from the dark matter direct detection experiment XENONnT (110), which establishes upper limits on λ_{345} for each selected mass m_H.

After the scan is made and cut-1 is applied, we use the software micrOMEGAs 5.3.35 (165) to evaluate the relic abundance for each scenario allowed in the scan, determining cut-2. MicrOMEGAs is a modular software written in C and Fortran that computes the relic density for a stable massive particle and the cross-sections of direct detection and indirect detection of dark matter. MicrOMEGAs uses the package CalcHEP (166) that evaluates the cross-sections at tree-level from the squared matrix elements. For that, a model file that contains the list of particles, vertices (Feynman rules), and parameters is required. Some models such as the Minimal Supersymmetric Standard Model (MSSM) or the IDM are already implemented in the program. A new model can be implemented through the LanHEP package which evaluates the Feynman rules from a Lagrangian file that could be given by the user. The software has modules that evaluate different observables for different experiments: the SD and SI WIMP-nucleon cross-section, for both proton or neutron scattering; the annihilation and co-annihilation cross-sections and the relic density evaluated by solving the Boltzmann Equation; the annihilation cross-section

at zero temperature limit, the observable of indirect detection; cross-sections and decay widths for particles produced at colliders. The framework of micrOMEGAs is represented in Figure 31. For further details the Refs. (164) and (160) and *The micrOMEGAs user's manual, version 5.3.34* (165) are suggested for the interested reader and also the micrOMEGAs official web site page https://lapth.cnrs.fr/micromegas/. (167)

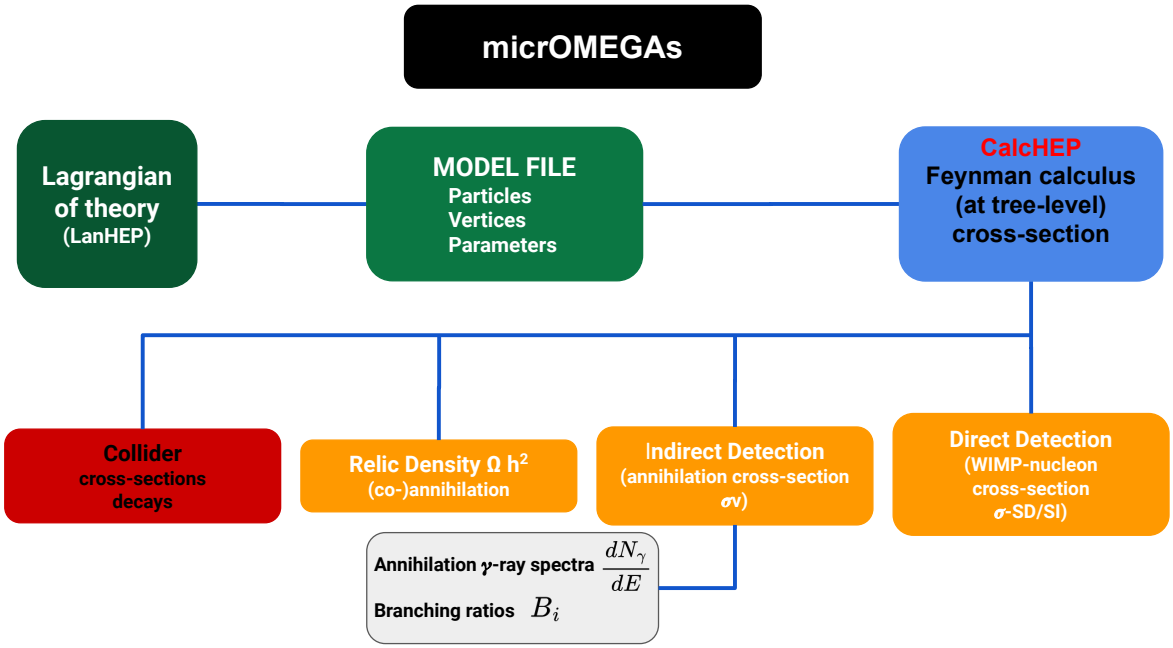

Figure 31 – Flow chart of micrOMEGAS framework with the auxiliary packages and modules.

Source: Adapted from BELANGER *et al.* (164)

As seen in subsection 5.5.1, the main channel for direct detection is the spin-independent scattering between our dark matter candidate H with a nucleon mediated by the SM Higgs h, which cross-section depends only on the coupling λ_{345} and the dark matter mass $m_{DM} = m_H$ (see Eq. (5.45)). Currently, the strongest limits for the SI WIMP-nucleon cross-section come from the XENONnT experiment (110) as seen in Figure 11b. For masses above 100 GeV the SI cross-section goes as $\sigma_{SI} \sim m_{DM}$, as is possible to see from Eq. (3.73), what enables us to extrapolate the limits from $m_{DM} \approx 100\,\text{GeV}$ to the TeV scale. Then, the limits in the $\sigma_{H-N} \times m_H$ space are mapped into the $\lambda_{345} \times m_H$ space using the micrOMEGAs calculations. The evaluation made by micrOMEGAs was compared with the expression given by Eq. (5.45) and both were checked as compatible. Now that the cuts and the working scheme of micrOMEGAs have been described, the next subsections deal with the scans made in the parameter space and the results obtained.

6.2 Random scan

In the first scan, 250,000 scenarios were generated with parameters logarithmically sampled in the ranges displayed in Eq. (6.1). Then, cut-1 (unitarity) was applied and the relic abundance was evaluated by micrOMEGAs. Cut-2 (relic abundance) can be implemented as an upper limit, in the possibility that there could be other dark matter components, or an exact constraint if there is just one dark matter candidate. Cut-3 from XENONnT data provides as upper limits a curve $\lambda_{345} \sim m_H^{3/2}$ (see Eq. (5.45) and the linear extrapolation in Figure 11b), which considerably restricts the available parameter space.

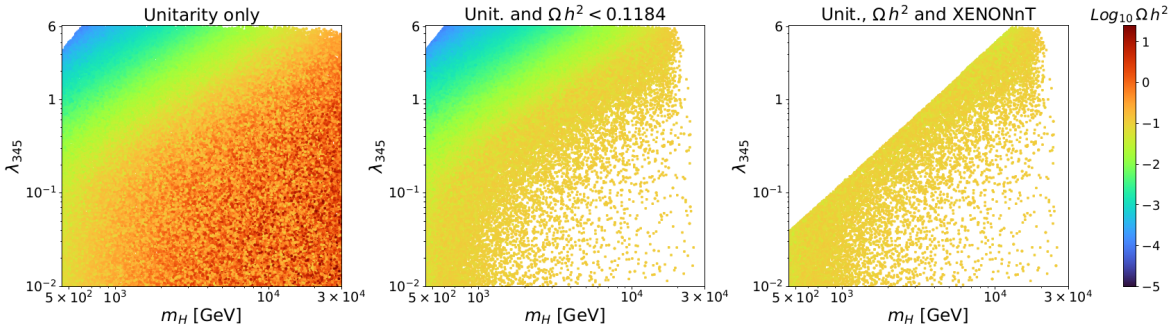

Figure 32 – Color map of the relic abundance Ωh^2 at logarithmic scale in the $\lambda_{345} \times m_H$ parameter space for the random scan. Left panel: just unitarity cut-1 is applied. Center panel: cut-1 and cut-2 with the upper limit $\Omega h^2 < 0.1184$. Right panel: beyond cut-1 and cut-2, the direct detection limits from XENONnT cut-3 are imposed.

Source: By the author.

The relic abundance Ωh^2 for the random scan is shown in the color map at logarithmic scale in Figure 32, where the axes are the scalar particle mass m_H and the coupling λ_{345}. In this graph, the abundance map is shown after each cut is applied. On the left panel it can be seen that abundance increases as the dark matter particle mass m_H increases and the coupling λ_{345} decreases. This is easily understood from the estimate of abundance in the WIMP miracle (see subsection 3.1.3) $\Omega h^2 \sim m_{DM}/\langle\sigma v\rangle$. The center panel shows how unitarity and relic abundance constrain the dark matter mass up to some tens of TeV. Direct detection on the right panel cuts high couplings and low masses.

The same cuts and analysis can be made by taking cut-2 ($\Omega h^2 = 0.1184$) as an exact constraint. The result is shown in Figure 33. This picture shows how unitarity and relic abundance constrain the dark matter particle mass to be greater than 500 GeV and bellow $\approx$ 25 TeV. Direction detection cuts some points (yellow) for low masses, $m_H \lesssim$ 5 TeV, leaving approximately 800 scenarios (red points) satisfying all constraints.

Then, for each one of the approximately 800 scenarios, the annihilation cross-section times velocity in the zero temperature limit $\langle\sigma v\rangle$ and the branching ratios of

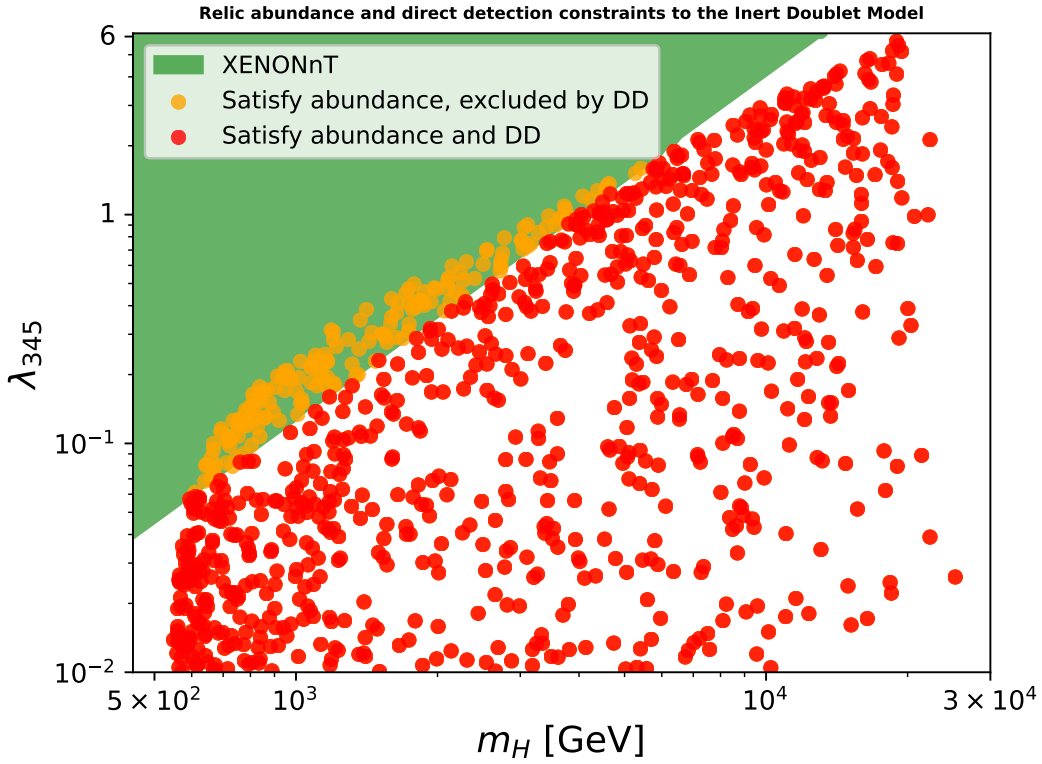

Figure 33 – Random scan in the $\lambda_{345} \times m_H$ parameter space of the IDM. Each point represents a scenario that agrees with unitarity (cut-1) and relic abundance $\Omega\, h^2 = 0.1184$ (cut-2). Direct detection exclusion from XENONnT (cut-3) is represented in green. Yellow points: satisfy relic abundance but are excluded by direct detection. Red points: satisfy relic abundance and direct detection.

Source: By the author.

annihilation channels B_i were evaluated using micrOMEGAs. This mapping $\lambda_{345} \times m_H \rightarrow \langle \sigma\, v \rangle \times m_H$ will enable comparing the scenarios consistent with theoretical, abundance, and direct detection constraints to the limits from indirect detection. The limits from indirect detection will be obtained from the discrete scan that is the subject of the next section.

6.3 Discrete scan

For the evaluation of indirect detection limits, we follow the approach of Ref. (159) where some benchmarks are taken by fixing the mass-splitting of the co-annihilating particles. We choose mass-splittings of $\Delta_o, \Delta_+ = 0.5, 1, 5$ and $10\,\text{GeV}$, providing 16 benchmarks. For each benchmark, the mass m_H was varied with logarithmic steps between $300\,\text{GeV}$ and $30,000\,\text{GeV}$, the same was made for the coupling λ_{345} between 10^{-2} and 2π. For each combination of the parameters, the abundance was evaluated by micrOMEGAs and the points that provide the correct relic abundance $\Omega\, h^2$ were selected defining *correct abundance curves* $\lambda_{345}\,(m_H)$ for each benchmark. For each mass value m_H of these curves,

the annihilation gamma-ray spectra $\frac{dN}{dE} = \sum_i B_i \frac{dN_i}{dE}$ and the branching ratios B_i of the main channels were evaluated using micrOMEGAs. This data will be used to evaluate the indirect detection limits for the benchmarks.

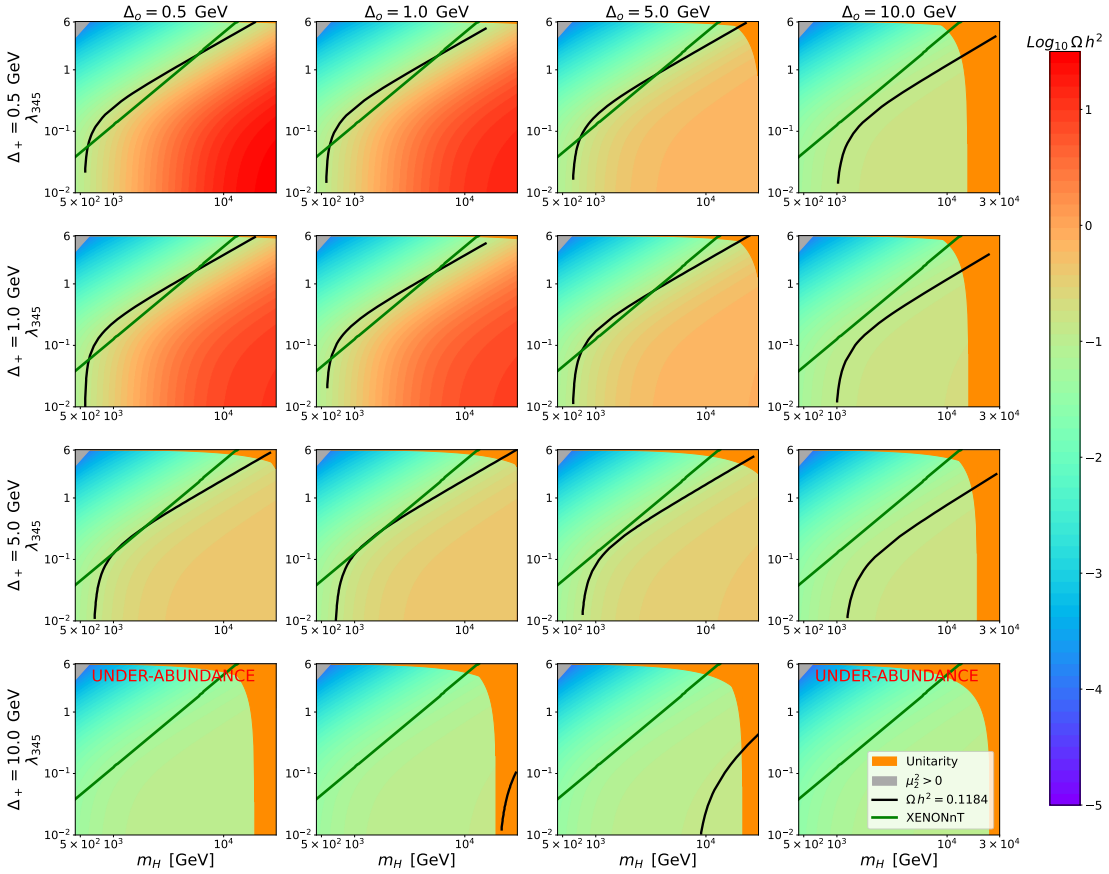

Figure 34 – Color map of the relic abundance Ωh^2 at logarithmic scale in the $\lambda_{345} \times m_H$ parameter space for the discrete scan. Each row corresponds to one of the mass-splittings $\Delta_+ = (0.5, 1, 5, 10)$ GeV and each column to one Δ_o in the same selection of values. Black lines: correct relic abundance. Green lines: XENONnT exclusion limits. Orange band: unitarity constraint. Grey band: inertness constraint.

Source: By the author.

The abundance maps for the discrete scan are shown in Figure 34 together with unitarity and inertness constraints (cut-1). The correct abundance curves are represented in black (cut-2) while the direct detection XENONnT exclusion limits are in green (cut-3). From that, some properties of the IDM can be derived. As already seen in Figure 32, abundance increases to high dark matter masses m_H or low couplings λ_{345}. The effect of co-annihilation is seen as small mass-splitting implying an enhancement of the abundance. It is also perceptible how complementary direct detection and relic abundance are for the

IDM. This means that the increasing of direct detection sensitivity in the future will constrain even more the available scenarios. Unitarity constraints, which are shown in orange, basically limit the upper value for the mass m_H up to $\approx 25\,\text{TeV}$. The $\Delta_+ = 10\,\text{GeV}$ row is excluded either by under-abundance or by unitary, except for $\Delta_o = 5\,\text{GeV}$.

With theoretical, collider, direct detection, and abundance constraints established, the next sections will focus on the indirect detection limits of gamma-ray observatories to the Inert Doublet Model.

6.4 Indirect detection limits to the Inert Doublet Model

The discrete scan has provided relic abundance curves $\lambda_{345}(m_H)$ that give the gamma-ray spectrum at each mass value m_H of each curve, i.e.,

$$\left.\frac{dN}{dE}(m_H)\right|_{(\Delta_+,\Delta_o)} = \sum_i B_i\left(m_H, \Delta_+, \Delta_o, \lambda_{345}(m_H)\right)\frac{dN_i}{dE}, \tag{6.2}$$

which is used as input for the sensitivity of the indirect detection code developed before. This code returns the 95% C.L. upper limit of the annihilation cross-section times velocity for a specific gamma-ray observatory at a given dark matter particle mass m_{DM}. The indirect detection limits can then be compared with the relic abundance cross-section at zero temperature supplied by the same relic curves. Fixing the splittings Δ_+ and Δ_o also allows comparing directly the indirect and direct detection limits: if the three particle masses are fixed, both annihilation $\langle\sigma\, v\rangle$ and WIMP-nucleon σ_{H-N} cross-sections will be proportional to λ_{345}, what makes possible a univocal comparison between these two limits.

Figure 35 shows the compilation of all the limits of the IDM benchmarks considered in this work: unitarity, relic abundance, direct detection, and indirect detection. The available scenarios are represented by the points in the relic abundance curves (red) that are below the limits of XENONnT, HESS (546h of observation at the GC), and the projected CTA (525h of observation at the GC) limits. In the first place, the main IDM feature is evidenced as $\langle\sigma\, v\rangle$ lies in the $5\times10^{-26} - 10^{-25}\,\text{cm}^3\text{s}^{-1}$ range, some times greater than the typical annihilation cross-section. In this picture, it is also possible to see the complementarity between direct detection and indirect detection limits: for small mass-splittings, $\Delta_+, \Delta_o \lesssim 1\,\text{GeV}$, XENONnT exclusion dominates in the $0.5\,\text{TeV} - 2\,\text{TeV}$ mass range while HESS is stronger for m_{DM} in $2 - 20\,\text{TeV}$. For greater mass-splittings, HESS always dominates over direct detection. HESS excludes masses between $\approx 1\,\text{TeV}$ and $\approx 10\,\text{TeV}$, for all benchmarks. This means that most IDM scenarios are already excluded by the actual indirect detection data from the HESS telescope. Furthermore, the projected CTA limits surpass the XENONnT and HESS limits for all masses. In this way, CTA will be able to probe all viable scenarios leading to a total exclusion of the model or a discovery.

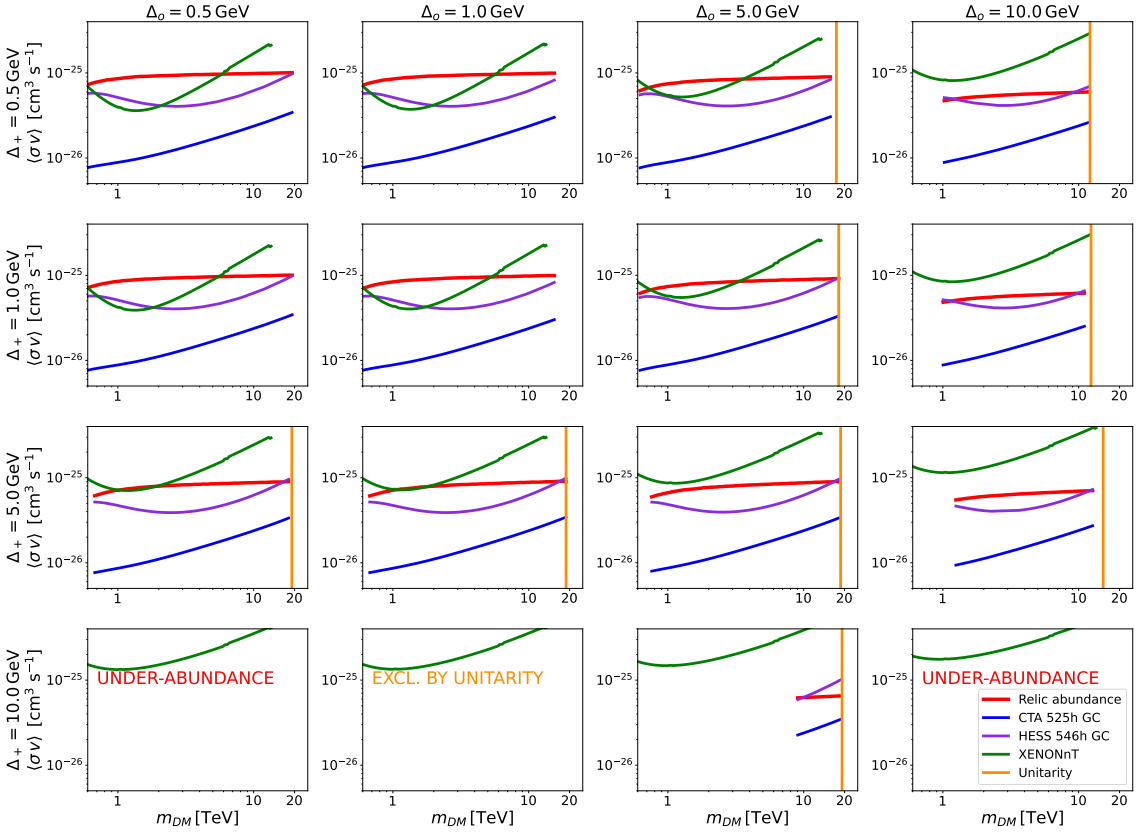

Figure 35 – Compilation of constraints to the IDM in the annihilation cross-section times velocity versus dark matter particle mass $\langle\sigma\, v\rangle \times m_{DM}$ space: relic abundance (red lines), direct detection exclusion limits at 90% C.L. from XENONnT (green lines) and indirect detection expected limits at 95% C.L. for HESS (purple lines) and for CTA (blue lines), both at the Galactic Center. Each row corresponds to one of the mass-splittings $\Delta_+ = (0.5, 1, 5, 10)\,\text{GeV}$ and each column to one Δ_o in the same selection of values. The unitarity upper bound for mass is shown in orange. The viable points are the ones in the red abundance curves below the direct and indirect detection limits.

Source: By the author.

The indirect detection limits change very little for each benchmark. This slight difference appears due to the difference in the branching ratios B_i. The main channels in the high mass regime are the bosonic channels W^+W^-, ZZ, and hh. The quark channel tt is the more relevant between the fermion states, but its contribution is at most $\approx 1\%$. Another channel that can play a role is the EW radiative emission $HH \to \gamma W^+W^-$ (see Refs (168) and (169) for a detailed discussion about this channel). The distributions of branching ratios for these four channels are shown in Figure 36 for three ranges of mass sampled from the random scan: $0.6\,\text{TeV} < m_{DM} < 0.7\,\text{TeV}$, $1.5\,\text{TeV} < m_{DM} < 2.0\,\text{TeV}$

and 15 TeV $< m_{DM} <$ 20 TeV. These histograms demonstrate that W^+W^- and ZZ states dominate the annihilation channels, contributing together almost 90%. Both of these channels have branching fractions concentrated around 50% for the first sample (first row of Figure) and their distributions become spread for higher masses. The W^+W^- state is dominant over ZZ for $m_{DM} > 1.5$ TeV for most scenarios. Regarding other channels, the Higgs hh one does not surpass $\approx 20\%$ of contribution, while the EW radiative γW^+W^- correction reaches contributions of at most $\approx 10\%$.

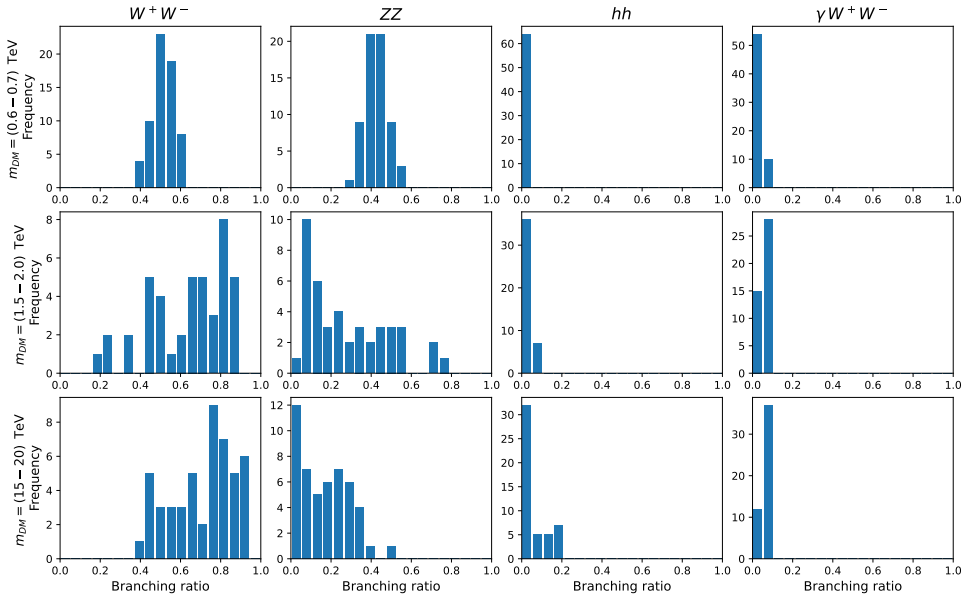

Figure 36 – Distribution of branching ratios B_i for the main channels of dark matter annihilation in the IDM: W^+W^-, ZZ, hh, and γW^+W^-. Each column represents one of these channels and each row the sample of scenarios considered.

Source: By the author.

That variability of branching contribution also applies to the discrete scan, which explains the difference between indirect detection limits. To lead with that, the upper and lower limits of the benchmarks were taken as a *band of exclusion*. This enables comparing the viable scenarios, taken from the random scan, with the indirect detection limits, obtained from the discrete scan.

Figure 37 shows the comparison of the exclusion bands and the abundance points. The bottom panel shows the same result with color maps of the mass-splittings Δ_+ and Δ_o. The red points correspond to the scenarios obtained from the random scan that satisfy relic abundance, unitarity, and direct detection limits from XENONnT data. As in Figure 35, thermal annihilation cross-sections times velocity is in the $5 \times 10^{-26} - 10^{-25}\,\mathrm{cm^3 s^{-1}}$ range, greater than the typical WIMP value due to co-annihilation, as stated before. Regarding indirect detection, all the points above the bands are excluded, points below the band

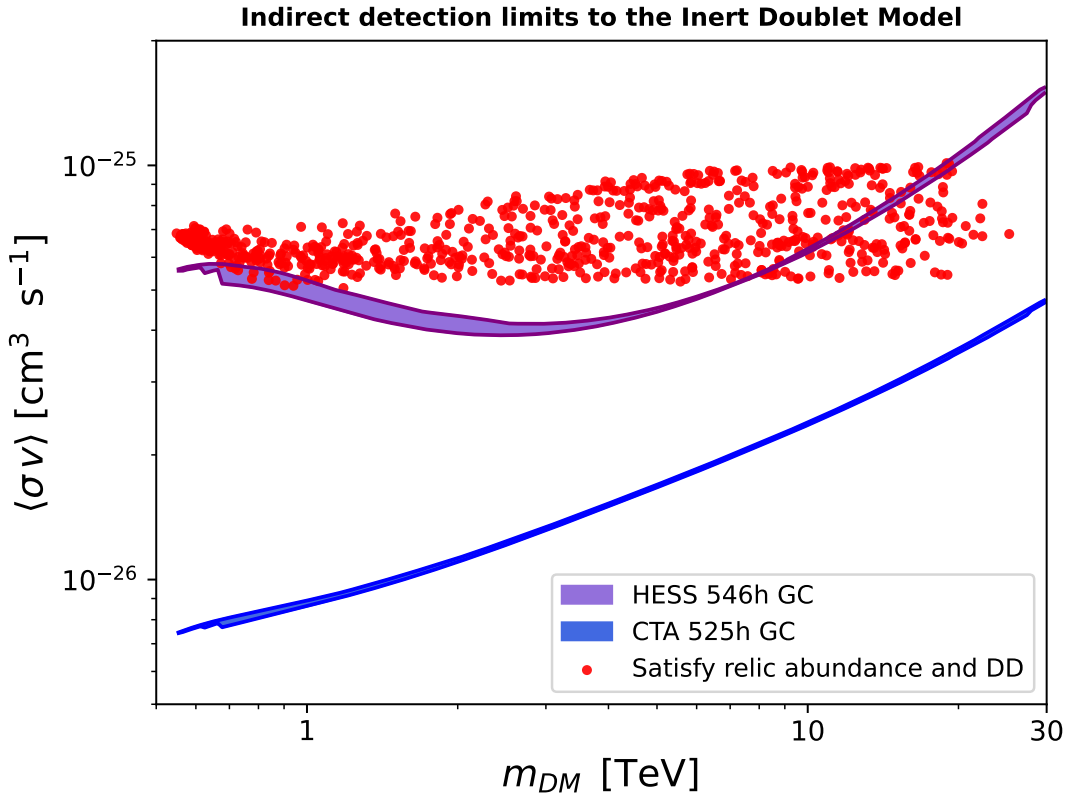

(a) Sensitivity of gamma-ray observatories to the Inert Doublet Model. Points in red represent viable scenarios obtained in the random scan that satisfy unitarity, relic abundance, and XENONnT direct detection limits.

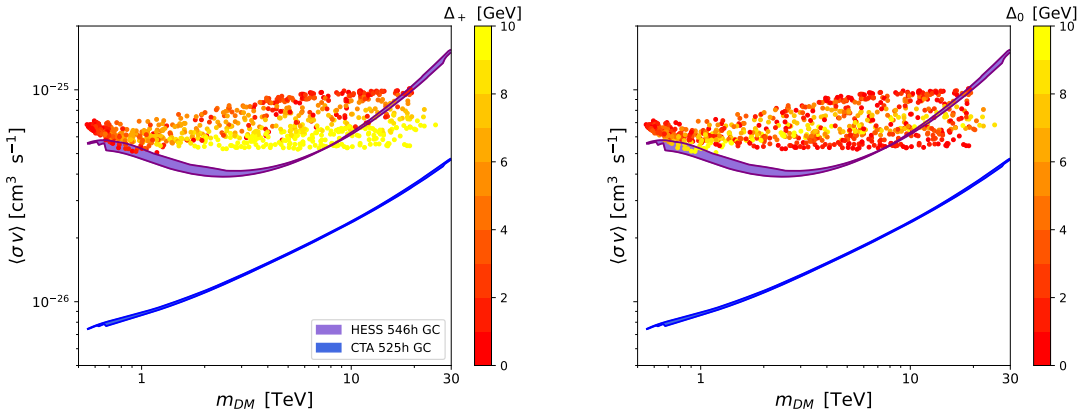

(b) Indirect detection limits to the Inert Doublet Model, as above, with color maps of the mass-splittings Δ_+ and Δ_o.

Figure 37 – Compilation of indirect detection exclusion limits at 95% C.L. to the Inert Doublet Model: HESS (purple) and CTA (blue), both at the Galactic Center. The exclusion limits are shown as bands due to the difference in branching ratio between benchmarks.

Source: By the author.

are still viable and points within the band have an annihilation cross-section near the sensitivity of the observatory, and their exclusion remains inconclusive. The conclusions are equivalent to the ones from the discrete scan: actual HESS data excludes a great

part of viable scenarios, including all dark matter masses m_{DM} between $\approx 1 - 8\,\text{TeV}$. Some scenarios in the $0.6 - 1\text{TeV}$ mass range with $\Delta_+ \lesssim 2\,\text{GeV}$ and $\Delta_o \gtrsim 5\,\text{GeV}$ are within the band of HESS exclusion. A significant number of points with masses in the $10\,\text{TeV} \lesssim m_{DM} \lesssim 20\,\text{TeV}$ range are under HESS limits and are still valid scenarios of the Inert Doublet Model. These remaining high-mass scenarios have, in general, $\Delta_+ \gtrsim 8\,\text{GeV}$ while, at the same time, Δ_o does not seem to have any correlation in this region. The projected CTA limits are almost one order of magnitude stronger than the ones from HESS and they would exclude all viable scenarios. This means that CTA will be able to probe all the parameter space of the Inert Doublet model, excluding it or even making a discovery.

In this chapter, the limits of indirect detection for HESS and CTA have been obtained for the Inert Doublet Model and compared with relic abundance and direct detection constraints. For that, one random scan and one discrete scan were made to obtain the scenarios that satisfy these limits. That was possible using the micrOMEGAs software that performs tree-level calculations of the annihilation and WIMP-nucleon cross-section and solves the Boltzmann Equation. From the discrete scan, relic abundance curves for chosen benchmarks were used to obtain annihilation spectra and the associated branching ratios. This data, then, is used as input in the indirect detection sensitivity code developed before, obtaining thus the limits in the velocity-averaged annihilation cross-section versus mass space. One of the key results is that the 546h data of observation by the HESS telescope already excludes all scenarios of the Inert Doublet Model with masses m_{DM} in the $1 - 8\,\text{TeV}$ range. XENONnT excludes some scenarios but just for very small mass-splittings ($\Delta_+, \Delta_o \lesssim 5\,\text{GeV}$). Some scenarios with masses $m_{DM} \lesssim 1\,\text{TeV}$ or $10\,\text{TeV} \lesssim m_{DM} \lesssim 25\,\text{TeV}$ remain close or under HESS sensitivity and then can still be viable. All these scenarios will be probed by CTA, which will act as the definitive experiment that can discard or discover the dark matter particle in the Inert Doublet Model.

7 CONCLUSION

In this work, we have explored the viability of a specific model for dark matter, the Inert Doublet Model, and evaluated the associated indirect detection limits from gamma-ray observatories. The limits of current data from HESS and the projected performance of CTA were compared with direct detection and thermal relic abundance constraints.

Before presenting the limits of the chosen model, the main evidences and candidates for dark matter were reviewed in chapter 2. A brief description of the ΛCDM model of cosmology was also made. Chapter 3 described the particle dark matter paradigm, with special attention to the thermal production processes in the Early Universe, such as the freeze-out mechanism and co-annihilation. After that, the profile models of the dark matter distribution in galactic halos were described. Chapter 3 ends with the strategies that can be implemented to detect WIMP particles of dark matter. Among them, there is the indirect detection search with gamma rays, which is the focus of this work.

Chapter 4 presents the main properties of gamma-ray astronomy and how these techniques can be applied for the indirect detection of dark matter annihilation. The main kinds of gamma-ray telescopes were described. Among them, Imaging Cherenkov telescopes, such as HESS and CTA, have the best capability to explore dark matter annihilation in the TeV scale. The statistical method of likelihood was presented in order to establish exclusion limits on the dark matter annihilation cross-section. A code was developed to evaluate indirect detection limits from gamma-ray observatories to both model-independent and model-dependent approaches.

The Inert Doublet Model of dark matter was reviewed in chapter 5. The constraints of the IDM from theoretical considerations and collider searches were presented. Next, it was discussed how the IDM provides a viable candidate for dark matter and how it can be explored by direct detection and relic abundance constraints. The IDM is an interesting model for indirect detection searches because its annihilation cross-section is enhanced by co-annihilation, allowing current data to probe thermal relic abundance already.

Chapter 6 presents the determination of indirect detection limits to the IDM and the complementarity with direct detection and relic abundance. Scans on the parameter space of IDM provide scenarios on the high-mass regime that are consistent with unitarity constraints. Furthermore, relic abundance was evaluated using numerical calculations from micrOMEGAs and it was used as a cut in the parameter space. Limits from the direct detection experiment XENONnT are mapped into the annihilation cross-section of the IDM as a further constraint. The indirect detection limits were evaluated for different benchmarks, which differ from each other due to the difference in branching ratios of the

primary channels. The branching ratios of the IDM were revealed to be dominated by the bosonic channels. The HESS data on the Galactic Center excludes all scenarios on the 1 - 8 TeV mass range. Some scenarios out of this range were determined as still inconclusive or below the HESS sensitivity.

The most important conclusion of this work is that CTA will be able to probe the remaining scenarios of the IDM in the future, leading to a discovery or a total exclusion. Further improvements can be made, such as accounting for Sommerfeld enhancement and considering loop-level evaluations. Even in those cases, CTA limits at the Galactic Center should surpass the sensitivity of direct detection experiments and other gamma-ray telescopes for all the parameter space of the Inert Doublet Model. These results illustrate the importance of CTA for the searches for dark matter in the model-dependent approach.

REFERENCES

1 BABCOCK, H. W. The rotation of the andromeda nebula. **Lick Observatory Bulletin**, n. 498, p. 41–51, 1939. DOI:10.5479/ADS/bib/1939LicOB1941b.

2 RUBIN, V. C.; FORD, W. K. Rotation of the andromeda nebula from a spectroscopic survey of emission regions. **Astrophysical Journal**, v. 159, p. 379, 1970. DOI: 10.1086/150317.

3 WHITEHURST, R. N.; ROBERTS, M. S. High-velocity neutral hydrogen in the central region of the andromeda galaxy. **Astrophysical Journal**, v. 175, p. 347–352, 1972.

4 FREEMAN, K. C. On the disks of spiral and s0 galaxies. **Astrophysical Journal**, v. 160, p. 811, 1970.

5 GELLER, M. J.; HUCHRA, J. P. Mapping the universe. **Science**, v. 246, n. 4932, p. 897–903, 1989.

6 PROFUMO, S.; GIANI, L.; PIATTELLA, O. F. An introduction to particle dark matter. **Universe**, v. 5, n. 10, p. 213, 2019. DOI: 103390/universe5100213.

7 AGHANIM, N. *et al.* Planck 2018 results-vi. cosmological parameters. **Astronomy & Astrophysics**, v. 641, p. A6, 2020. DOI: 10.1051/0004–6361/20188339910.

8 ACHARYYA, A. Sensitivity of the Cherenkov Telescope Array to a dark matter signal from the galactic centre. **Journal of Cosmology and Astroparticle Physics**, v. 2021, n. 01, p. 057, 2021. DOI 10.1088/1475–7516/2021/01/057.

9 CIRELLI, M. *et al.* PPPC 4 DM ID: a poor particle physicist cookbook for dark matter indirect detection. **Journal of Cosmology and Astroparticle Physics**, v. 2011, n. 03, p. 051–051, 2011. DOI: 10.1088/1475–7516/2011/03/051.

10 BERTONE, G.; HOOPER, D. History of dark matter. **Reviews of Modern Physics**, APS, v. 90, n. 4, p. 045002, 2018.

11 ZWICKY, F. Die rotverschiebung von extragalaktischen nebeln. **Helvetica Physica Acta**, v. 6, p. 110–127, 1933.

12 KELVIN, W. T. B. **Baltimore lectures on molecular dynamics and the wave theory of light**. Cambridge: Cambridge University Press, 2010.

13 POINCARÉ, H. The milky way and the theory of gases. **Popular Astronomy**, v. 14, p. 475–488, 1906.

14 JEANS, J. H. The motions of stars in a kapteyn universe. **Monthly Notices of the Royal Astronomical Society**, v. 82, p. 122–132, 1922.

15 OORT, J. H. The force exerted by the stellar system in the direction perpendicular to the galactic plane and some related problems. **Bulletin of the Astronomical Institutes of the Netherlands**, v. 6, p. 249, 1932.

16 ZWICKY, F. On the masses of nebulae and of clusters of nebulae. **Astrophysical Journal**, v. 87, p. 217–246, 1937. DOI: 10.4159/Harvard.9780674366688.c.115.

17 HUBBLE, E.; HUMASON, M. L. The velocity-distance relation among extra-galactic nebulae. **Astrophysical Journal**, v. 74, p. 43, 1931. DOI: 10.1086/143323.

18 ŁOKAS, E. L.; MAMON, G. A. Dark matter distribution in the coma cluster from galaxy kinematics: breaking the mass–anisotropy degeneracy. **Monthly Notices of the Royal Astronomical Society**, v. 343, n. 2, p. 401–412, 2003.

19 HUBBLE, E. P. Extra-galactic nebulae. **Astrophysical Journal**, v. 64, p. 321–369, 1926.

20 HULST, H. C.; RAIMOND, E.; WOERDEN, H. V. Rotation and density distribution of the andromeda nebula derived from observations of the 21-cm line. **Bulletin of the Astronomical Institutes of the Netherlands1**, v. 14, n. 480, p. 1, 1957.

21 ROGSTAD, D.; SHOSTAK, G. Gross properties of five scd galaxies as determined from 21-centimeter observations. **Astrophysical Journal**, v. 176, p. 315, 1972. DOI: 10.1086/151636.

22 ROBERTS, M.; ROTS, A. Comparison of rotation curves of different galaxy types. **Astronomy and Astrophysics**, v. 26, p. 483–485, 1973.

23 EINASTO, J.; KAASIK, A.; SAAR, E. Dynamic evidence on massive coronas of galaxies. **Nature**, v. 250, n. 5464, p. 309–310, 1974.

24 BOSMA, A. The distribution and kinematics of neutral hydrogen in spiral galaxies of various morphological types. 1978. Ph. D. Thesis (Doctor) – Groningen University, Groningen, 1978.

25 RUBIN, V. C.; FORD, W. K.; THONNARD, N. Extended rotation curves of high-luminosity spiral galaxies. iv-systematic dynamical properties, SA through SC. **Astrophysical Journal**, v. 225, p. L107–L111, 1978. DOI:10.1086/182804.

26 ALPHER, R. A.; HERMAN, R. Evolution of the universe. **Nature**, v. 162, n. 4124, p. 774–775, 1948.

27 GAMOW, G. The evolution of the universe. **Nature**, v. 162, n. 4122, p. 680–682, 1948.

28 BUCHER, M. Physics of the cosmic microwave background anisotropy. **International Journal of Modern Physics D**, v. 24, n. 02, p. 1530004, 2015. DOI: 10.1142/SO218271815300049.

29 PENZIAS, A. A.; WILSON, R. W. A measurement of excess antenna temperature at 4080 mhz. *In*: LANG, K. R.; GINGERICH, O. (ed.). **A source book in astronomy and astrophysics, 1900–1975**, Cambridge: Harvard University Press, 1979. p. 873–876.

30 DICKE, R. H. *et al.* Cosmic black-body radiation. **Astrophysical Journal**, v. 142, p. 414–419, 1965.

31 FIXSEN, D. The temperature of the cosmic microwave background. **The Astrophysical Journal**, IOP Publishing, v. 707, n. 2, p. 916, 2009.

32 FIXSEN, D. *et al.* The cosmic microwave background spectrum from the full cobe* firas data set. **Astrophysical Journal**, IOP Publishing, v. 473, n. 2, p. 576, 1996.

33 BENNETT, C. L. *et al.* Nine-year wilkinson microwave anisotropy probe (wmap) observations: final maps and results. **Astrophysical Journal Supplement Series**, IOP Publishing, v. 208, n. 2, p. 20, 2013.

34 ADAM, R. *et al.* Planck 2015 results-i. overview of products and scientific results. **Astronomy & Astrophysics**, v. 594, p. A1, 2016. DOI: 10.1051/0004–6361/201527101.

35 PRIMACK, J. R. **Dark matter and structure formation in the Universe**. 1997. Available at: https://arxiv.org/pdf/astro--ph/9707285.pdf. Accessible at: 23 Jan. 2024.

36 SPRINGEL, V.; FRENK, C. S.; WHITE, S. D. The large-scale structure of the universe. **Nature**, v. 440, n. 7088, p. 1137–1144, 2006.

37 COLLESS, M. *et al.* The 2df galaxy redshift survey: spectra and redshifts. **Monthly Notices of the Royal Astronomical Society**, Blackwell Science Ltd Oxford, UK, v. 328, n. 4, p. 1039–1063, 2001.

38 BLANTON, M. R. *et al.* Sloan digital sky survey iv: mapping the milky way, nearby galaxies, and the distant universe. **Astronomical Journal**, IOP Publishing, v. 154, n. 1, p. 28, 2017.

39 CROTON, D. J. *et al.* The many lives of active galactic nuclei: cooling flows, black holes and the luminosities and colours of galaxies. **Monthly Notices of the Royal Astronomical Society**, Blackwell Science Ltd Oxford, UK, v. 365, n. 1, p. 11–28, 2006.

40 MAKSIMOVA, N. A. *et al.* Abacussummit: a massive set of high-accuracy, high-resolution n-body simulations. **Monthly Notices of the Royal Astronomical Society**, Oxford University Press, v. 508, n. 3, p. 4017–4037, 2021.

41 WALD, R. M. **General relativity**. Chicago: University of Chicago Press, 2010.

42 DYSON, F. W.; EDDINGTON, A. S.; DAVIDSON, C. A determination of the deflection of light by the sun's gravitational field, from observations made at the total eclipse of may 29, 1919. **Philosophical Transactions of the Royal Society of London Series A: containing papers of a mathematical or physical character**, The Royal Society London, v. 220, n. 571-581, p. 291–333, 1920.

43 SCHNEIDER, P.; EHLERS, J.; FALCO, E. Gravitational lenses. **Berlin: Springer-Verlag**, 1992.

44 CRANE, P. *et al.* First results from the faint object camera-images of the gravitational lens system g2237+ 0305. **Astrophysical Journal, Part 2-Letters**, v. 369, p. L59–L61, 1991.

45 MASSEY, R.; KITCHING, T.; RICHARD, J. The dark matter of gravitational lensing. **Reports on Progress in Physics**, IOP Publishing, v. 73, n. 8, p. 086901, 2010.

46 CLOWE, D. *et al.* A direct empirical proof of the existence of dark matter. **Astrophysical Journal**, IOP Publishing, v. 648, n. 2, p. L109, 2006.

47 GREGO, L. *et al.* Galaxy cluster gas mass fractions from sunyaev-zeldovich effect measurements: Constraints on Ωm. **Astrophysical Journal**, IOP Publishing, v. 552, n. 1, p. 2, 2001.

48 NASA. **The bullet Cluster**. 2007. Available at: https://www.esa.int/ESA_Multimedia/Images/2007/07/The_Bullet_Cluster2. Accessible at: 28 Feb. 2024.

49 RANDALL, S. W. *et al.* Constraints on the self-interaction cross section of dark matter from numerical simulations of the merging galaxy cluster 1e 0657–56. **Astrophysical Journal**, v. 679, n. 2, p. 1173, 2008.

50 KADOTA, K.; SEKIGUCHI, T.; TASHIRO, H. **A new constraint on millicharged dark matter from galaxy clusters**. 2016. Available at: https://arxiv.org/pdf/1602.04009.pdf. Accessible at: 30 Nov. 2023.

51 WHITE, S. D.; FRENK, C. S.; DAVIS, M. Clustering in a neutrino-dominated universe. **Astrophysical Journal, Part 2-Letters,**, v. 274, p. L1–L5, 1983.

52 POULIN, V.; SERPICO, P. D.; LESGOURGUES, J. A fresh look at linear cosmological constraints on a decaying dark matter component. **Journal of Cosmology and Astroparticle Physics**, IOP Publishing, v. 2016, n. 08, p. 036, 2016.

53 BERTONE, G.; HOOPER, D.; SILK, J. Particle dark matter: Evidence, candidates and constraints. **Physics Reports**, Elsevier, v. 405, n. 5-6, p. 279–390, 2005.

54 ARBEY, A.; MAHMOUDI, F. Dark matter and the early universe: a review. **Progress in Particle and Nuclear Physics**, Elsevier, v. 119, p. 103865, 2021.

55 BERTONE, G.; TAIT, T. M. A new era in the search for dark matter. **Nature**, v. 562, n. 7725, p. 51–56, 2018.

56 MILGROM, M. A modification of the newtonian dynamics as a possible alternative to the hidden mass hypothesis. **Astrophysical Journal, Part 1**, v. 270, p. 365–370, 1983.

57 MILGROM, M. A modification of the newtonian dynamics-implications for galaxies. **Astrophysical Journal**, v. 270, p. 371–383, 1983.

58 SANDERS, R. Clusters of galaxies with modified newtonian dynamics. **Monthly Notices of the Royal Astronomical Society**, Blackwell Science Ltd Oxford, UK, v. 342, n. 3, p. 901–908, 2003.

59 DODELSON, S. The real problem with mond. **International Journal of Modern Physics D**, World Scientific, v. 20, n. 14, p. 2749–2753, 2011.

60 BEKENSTEIN, J. D. Relativistic gravitation theory for the modified newtonian dynamics paradigm. **Physical Review D**, APS, v. 70, n. 8, p. 083509, 2004.

61 FAMAEY, B.; MCGAUGH, S. Challenges for λcdm and mond. **Journal of Physics:** conference series. v. 437, n. 1, p. 012001, 2013.

62 GRIEST, K. Galactic microlensing as a method of detecting massive compact halo objects. **Astrophysical Journal, Part 1**, v. 366, p. 412–421, 1991.

63 LASSERRE, T. *et al.* **Not enough stellar mass Machos in the Galactic halo**. 2000. Available at: https://arxiv.org/pdf/astro--ph/0002253.pdf. Accessible at: 30 Jan. 2024.

64 CARR, B.; CLESSE, S.; GARCÍA-BELLIDO, J. Primordial black holes from the qcd epoch: linking dark matter, baryogenesis, and anthropic selection. **Monthly Notices of the Royal Astronomical Society**, Oxford University Press, v. 501, n. 1, p. 1426–1439, 2021.

65 CARR, B. J.; HAWKING, S. W. Black holes in the early universe. **Monthly Notices of the Royal Astronomical Society**, Oxford University Press Oxford, v. 168, n. 2, p. 399–415, 1974.

66 BIRD, S. *et al.* Did ligo detect dark matter? **Physical Review Letters**, APS, v. 116, n. 20, p. 201301, 2016.

67 HAWKING, S. W. Particle creation by black holes. **Communications in Mathematical Physics**, Springer, v. 43, n. 3, p. 199–220, 1975.

68 TISSERAND, P. *et al.* Limits on the macho content of the galactic halo from the eros-2 survey of the magellanic clouds. **Astronomy & Astrophysics**, EDP Sciences, v. 469, n. 2, p. 387–404, 2007.

69 POULIN, V. *et al.* CMB bounds on disk-accreting massive primordial black holes. **Physical Review D**, APS, v. 96, n. 8, p. 083524, 2017.

70 GAGGERO, D. *et al.* Searching for primordial black holes in the radio and x-ray sky. **Physical Review Letters**, APS, v. 118, n. 24, p. 241101, 2017.

71 BARNACKA, A.; GLICENSTEIN, J.-F.; MODERSKI, R. New constraints on primordial black holes abundance from femtolensing of gamma-ray bursts. **Physical Review D**, APS, v. 86, n. 4, p. 043001, 2012.

72 PECCEI, R. D.; QUINN, H. R. Cp conservation in the presence of pseudoparticles. **Physical Review Letters**, APS, v. 38, n. 25, p. 1440, 1977.

73 PECCEI, R. D.; QUINN, H. R. Constraints imposed by cp conservation in the presence of pseudoparticles. **Physical Review D**, APS, v. 16, n. 6, p. 1791, 1977.

74 ROSENBERG, L. J.; BIBBER, K. A. V. Searches for invisible axions. **Physics Reports**, Elsevier, v. 325, n. 1, p. 1–39, 2000.

75 GALANTI, G. **Axion-like particles and high energy astrophysics**. 2019. Available at: https://arxiv.org/pdf/1911.09372.pdf. Accessible at: 10 Dec. 2023.

76 IRASTORZA, I. G.; REDONDO, J. New experimental approaches in the search for axion-like particles. **Progress in Particle and Nuclear Physics**, Elsevier, v. 102, p. 89–159, 2018.

77 DASGUPTA, B.; KOPP, J. Sterile neutrinos. **Physics Reports**, Elsevier, v. 928, p. 1–63, 2021.

78 DODELSON, S.; WIDROW, L. M. Sterile neutrinos as dark matter. **Physical Review Letters**, APS, v. 72, n. 1, p. 17, 1994.

79 CAMPOS, M. D. *et al.* Search for right-handed neutrinos from dark matter annihilation with gamma-rays. **Journal of Cosmology and Astroparticle Physics**, IOP Publishing, v. 2017, n. 07, p. 016, 2017.

80 ESCUDERO, M.; RIUS, N.; SANZ, V. Sterile neutrino portal to dark matter II: exact dark symmetry. **European Physical Journal C**, Springer, v. 77, p. 1–11, 2017.

81 LEE, B. W.; WEINBERG, S. Cosmological lower bound on heavy-neutrino masses. **Physical Review Letters**, APS, v. 39, n. 4, p. 165, 1977.

82 DICUS, D. A.; KOLB, E. W.; TEPLITZ, V. L. Cosmological upper bound on heavy-neutrino lifetimes. **Physical Review Letters**, APS, v. 39, n. 4, p. 168, 1977.

83 HUT, P. Limits on masses and number of neutral weakly interacting particles. **Physics Letters B**, Elsevier, v. 69, n. 1, p. 85–88, 1977.

84 BERTONE, G. **Particle dark matter**: observations, models and searches. Cambridge: Cambridge University Press, 2010.

85 JUNGMAN, G.; KAMIONKOWSKI, M.; GRIEST, K. Supersymmetric dark matter. **Physics Reports**, Elsevier, v. 267, n. 5-6, p. 195–373, 1996.

86 AGASHE, K.; SERVANT, G. Warped unification, proton stability, and dark matter. **Physical Review Letters**, APS, v. 93, n. 23, p. 231805, 2004.

87 BIRKEDAL-HANSEN, A.; WACKER, J. G. Scalar dark matter from theory space. **Physical Review D**, APS, v. 69, n. 6, p. 065022, 2004.

88 BELYAEV, A. *et al.* Anatomy of the inert two-higgs-doublet model in the light of the lhc and non-lhc dark matter searches. **Physical Review D**, v. 97, n. 3, p. 035011, 2018. DOI: 10.1103/PhysRevD.97.035011.

89 OSTRIKER, J.; PEEBLES, P.; YAHIL, A. The size and mass of galaxies and the mass of the universe. **Astrophysical Journal**, v. 193, p. L1, 1974. DOI: 10.1086/181617.

90 KOLB, E. W.; TURNER, M. S. **The early universe**. Boca Raton: CRC Press, 2018.

91 BAUER, M.; PLEHN, T. **Yet another introduction to dark matter:** the particle physics approach. Cham: Springer, 2019.(Lecture notes in physics, v. 959).

92 GONDOLO, P.; GELMINI, G. Cosmic abundances of stable particles: Improved analysis. **Nuclear Physics B**, Elsevier, v. 360, n. 1, p. 145–179, 1991.

93 LISANTI, M. Lectures on dark matter physics. *In:* POLCHINSKI, J.; VIEIRA, P.; DEWOLFE, O. (ed.) **New frontiers in fields and strings**. Singapore: World Scientific, p. 399–446, 2017.

94 ARCADI, G. *et al.* The waning of the wimp? a review of models, searches, and constraints. **The European Physical Journal C**, v. 78, p. 1–57, 2018.

95 GRIEST, K.; SECKEL, D. Three exceptions in the calculation of relic abundances. **Physical Review D**, APS, v. 43, n. 10, p. 3191, 1991.

96 EDSJÖ, J.; GONDOLO, P. Neutralino relic density including coannihilations. **Physical Review D**, APS, v. 56, n. 4, p. 1879, 1997.

97 NAVARRO, J.; FRENK, C.; WHITE, S. The structure of cold dark matter halos. **Astrophysical Journal**, v. 462, p. 563–575, 1996. DOI: 10.1086/177173.

98 MOORE, B. *et al.* Cold collapse and the core catastrophe. **Monthly Notices of the Royal Astronomical Society**, The Royal Astronomical Society, v. 310, n. 4, p. 1147–1152, 1999.

99 BEGEMAN, K.; BROEILS, A.; SANDERS, R. Extended rotation curves of spiral galaxies: dark haloes and modified dynamics. **Monthly Notices of the Royal Astronomical Society**, The Royal Astronomical Society, v. 249, n. 3, p. 523–537, 1991.

100 BERGSTRÖM, L.; ULLIO, P.; BUCKLEY, J. H. Observability of γ rays from dark matter neutralino annihilations in the milky way halo. **Astroparticle Physics**, Elsevier, v. 9, n. 2, p. 137–162, 1998.

101 BURKERT, A. The structure of dark matter halos in dwarf galaxies. **Astrophysical Journal Letters**, v. 447, p. L25–L28, 1995. DOI: 10.1086/309560.

102 GILLESSEN, S. *et al.* Monitoring stellar orbits around the massive black hole in the galactic center. **Astrophysical Journal**, IOP Publishing, v. 692, n. 2, p. 1075, 2009.

103 CATENA, R.; ULLIO, P. **A novel determination of the local dark matter density**. 2009. Available at: https://arxiv.org/pdf/0907.0018.pdf. Accessible at: 30 Nov. 2023.

104 XUE, X.-X. *et al.* The milky way's circular velocity curve to 60 kpc and an estimate of the dark matter halo mass from the kinematics of $\sim$ 2400 sdss blue horizontal-branch stars. **Astrophysical Journal**, IOP Publishing, v. 684, n. 2, p. 1143, 2008.

105 IOCCO, F.; BENITO, M. An estimate of the dm profile in the galactic bulge region. **Physics of the Dark Universe**, Elsevier, v. 15, p. 90–95, 2017.

106 QUEIROZ, F. S. **Dark matter overview**: collider, direct and indirect detection searches. 2016. Available at: https://arxiv.org/pdf/1605.08788.pdf. Accessible at: 30 Nov. 2023.

107 GOODMAN, M. W.; WITTEN, E. Detectability of certain dark-matter candidates. **Physical Review D**, APS, v. 31, n. 12, p. 3059, 1985.

108 SMITH, M. C. *et al.* The rave survey: constraining the local galactic escape speed. **Monthly Notices of the Royal Astronomical Society**, Blackwell Publishing Oxford, v. 379, n. 2, p. 755–772, 2007.

109 BILLARD, J. *et al.* Direct detection of dark matter—APPEC committee report. **Reports on Progress in Physics**, IOP Publishing, v. 85, n. 5, p. 056201, 2022.

110 APRILE, E. *et al.* First dark matter search with nuclear recoils from the xenonnt experiment. **Physical Review Letters**, APS, v. 131, n. 4, p. 041003, 2023.

111 SCHUMANN, M. Direct detection of wimp dark matter: concepts and status. **Journal of Physics G:** nuclear and particle physics. IOP Publishing, v. 46, n. 10, p. 103003, 2019.

112 LONGAIR, M. S. **High energy astrophysics**. Cambridge: Cambridge University Press, 2010.

113 GIESEN, G. *et al.* Ams-02 antiprotons, at last! secondary astrophysical component and immediate implications for dark matter. **Journal of Cosmology and Astroparticle Physics**, IOP Publishing, v. 2015, n. 09, p. 023, 2015.

114 CONRAD, J.; REIMER, O. Indirect dark matter searches in gamma and cosmic rays. **Nature Physics**, v. 13, n. 3, p. 224–231, 2017.

115 JUSTINO, L. R.; VIANA, A. Reconstruction of neutral pion-decay gamma-ray emission in the central molecular zone. **Boletim da Sociedade Astronômica Brasileira**, v. 34, n. 1, p. 161–162, 2023.

116 GABICI, S. *et al.* Acceleration of particles up to pev energies at the galactic centre. **Proceedings of the International Astronomical Union**, Cambridge University Press, v. 12, n. S324, p. 317–321, 2016.

117 SJÖSTRAND, T. *et al.* An introduction to pythia 8.2. **Computer physics communications**, Elsevier, v. 191, p. 159–177, 2015.

118 CIAFALONI, P. *et al.* Weak corrections are relevant for dark matter indirect detection. **Journal of Cosmology and Astroparticle Physics**, IOP Publishing, v. 2011, n. 03, p. 019, 2011.

119 VIANA, A. **Searching for dark matter with the southern wide-field Gamma-ray Observatory (SWGO)**. 2021. Available at: https://indico.ihep.ac.cn/event/11934/contributions/14609/. Accessible at: 11 Jan. 2024. DOI: 10.22323/1/395.0555.

120 NASA. **Fermi Gamma-ray Space Telescope**. Available at: https://fermi.gsfc.nasa.gov/. Accessible at: 11 Jan. 2024.

121 ATWOOD, W. *et al.* The large area telescope on the fermi gamma-ray space telescope mission. **Astrophysical Journal**, v. 697, n. 2, p. 1071–1102, 2009.

122 HOOPER, D.; GOODENOUGH, L. Dark matter annihilation in the galactic center as seen by the fermi gamma ray space telescope. **Physics Letters B**, Elsevier, v. 697, n. 5, p. 412–428, 2011.

123 HAWC COLLABORATION. **HAWC**: The high-altitude water cherenkov gamma-ray observatory. Available at: https://www.hawc-observatory.org/. Accessible at: 12 Jan. 2024.

124 LHAASO COLLABORATION. **LHAASO**: large high altitude air shower observatory. Available at: http://english.ihep.cas.cn/lhaaso/. Accessible at: 12 Jan. 2024.

125 SWGO COLLABORATION. **SWGO**: the southern wide-field gamma-ray observatory. Available at: https://www.swgo.org/SWGOWiki/doku.php?id=start. Accessible at: 12 Jan. 2024.

126 KILDEA, J. *et al.* The whipple observatory 10 m gamma-ray telescope, 1997–2006. **Astroparticle Physics**, Elsevier, v. 28, n. 2, p. 182–195, 2007.

127 BERNLÖHR, K. *et al.* The optical system of the Hess imaging atmospheric Cherenkov Telescopes. part i: layout and components of the system. **Astroparticle Physics**, Elsevier, v. 20, n. 2, p. 111–128, 2003.

128 ACCIARI, V. *et al.* Observation of gamma-ray emission from the galaxy m87 above 250 gev with veritas. **Astrophysical Journal**, IOP Publishing, v. 679, n. 1, p. 397, 2008.

129 FERENC, D. *et al.* The magic gamma-ray observatory. **Nuclear Instruments and Methods in Physics Research Section A:** accelerators, spectrometers, detectors and associated equipment. Elsevier, v. 553, n. 1-2, p. 274–281, 2005.

130 BOSE, D. *et al.* Ground-based gamma-ray astronomy: history and development of techniques. **The European Physical Journal Special Topics**, Springer, v. 231, n. 1, p. 3–26, 2022.

131 ACHARYA, B. S. *et al.* Introducing the CTA concept. **Astroparticle physics**, Elsevier, v. 43, p. 3–18, 2013.

132 THE CTA CONSORTIUM. Science with the Cherenkov telescope array. Singapore: World Scientific, 2017.

133 CHERENKOV TELESCOPE ARRAY. **CTAO's expected "Alpha Configuration" performance**. Available at: https://www.cta-observatory.org/science/ctao-performance/. Accessible at: 23 Jan. 2024.

134 THE CTA CONSORTIUM. **Usage of the CTAO media materials, images and videos**. Available at: https://www.cta-observatory.org/outreach-education/multimedia/media-usage/. Accessible at: 16 Jan. 2024.

135 VIANA, A. *et al.* Searching for dark matter in the galactic halo with a wide field of view tev gamma-ray observatory in the southern hemisphere. **Journal of Cosmology and Astroparticle Physics**, IOP Publishing, v. 2019, n. 12, p. 061, 2019.

136 NAUROIS, M. D.; ROLLAND, L. A high performance likelihood reconstruction of γ-rays for imaging atmospheric Cherenkov Telescopes. **Astroparticle Physics**, Elsevier, v. 32, n. 5, p. 231–252, 2009.

137 RINCHIUSO, L. **Study of the Galactic Center and dark matter search with HESS**. 2019. Thése (Doctorat) – Université Paris Saclay, Paris, 2019.

138 ABDALLA, H. *et al.* Search for Dark Matter Annihilation Signals in the H.E.S.S. Inner Galaxy Survey. **Physical Review Letters**, v. 129, n. 11, p. 111101, 2022.

139 WILKS, S. S. The large-sample distribution of the likelihood ratio for testing composite hypotheses. **Annals of Mathematical Statistics**, JSTOR, v. 9, n. 1, p. 60–62, 1938.

140 COWAN, G. *et al.* Asymptotic formulae for likelihood-based tests of new physics. **European Physical Journal C**, Springer, v. 71, p. 1–19, 2011.

141 LI, T.-P.; MA, Y.-Q. Analysis methods for results in gamma-ray astronomy. **Astrophysical Journal, Part 1**, v. 272, p. 317–324, 1983.

142 ROLKE, W. A.; LÓPEZ, A. M.; CONRAD, J. Limits and confidence intervals in the presence of nuisance parameters. **Nuclear Instruments and Methods in Physics Research Section A:** accelerators, spectrometers, detectors and associated equipment. Elsevier, v. 551, n. 2-3, p. 493–503, 2005.

143 AHARONIAN, F. *et al.* Discovery of very-high-energy γ-rays from the galactic centre ridge. **Nature**, Nature Publishing Group, v. 439, n. 7077, p. 695–698, 2006.

144 ABRAMOWSK, A. *et al.* Acceleration of Petaelectronvolt protons in the galactic centre. **Nature**, Nature Publishing Group, v. 531, n. 7595, p. 476–479, 2016.

145 AHARONIAN, F. *et al.* Very high energy gamma rays from the direction of sagittarius a. **Astronomy & astrophysics**, EDP Sciences, v. 425, n. 1, p. L13–L17, 2004.

146 ABDALLA, H. *et al.* Search for dark matter annihilations towards the inner galactic halo from 10 years of observations with H.E.S.S. **Physical Review Letters**, APS, v. 117, n. 11, p. 111301, 2016.

147 LEFRANC, V. **Recherche de matiére noire, observation du centre galactique avec HESS et modernisation des caméras de HESS I**. 2016. Thése (Doctorat en Astroparticules et cosmologie) – Université Paris–Saclay (ComUE), Paris, 2016.

148 DESHPANDE, N. G.; MA, E. Pattern of symmetry breaking with two higgs doublets. **Physical Review D**, APS, v. 18, n. 7, p. 2574, 1978.

149 NOVAES, S. F. **Standard model:** an introduction. 2000. Available at: https://arxiv.org/pdf/hep--ph/0001283.pdf. Accessible at: 12 Jan. 2024.

150 TYTGAT, M. *et al.* The inert doublet model: an archetype for dark matter? **Journal of Cosmology and Astroparticle Physics**, v. 7, p. 028, 2006. DOI: 10.1088/1475–7516/2007/02/028.

151 PARTICLE DATA GROUP. Review of particle physics. **Progress of Theoretical and Experimental Physics**, Oxford University Press, v. 2020, n. 8, p. 083C01, 2020.

152 FABIAN, S. **Study of the inert doublet model in the light of dark matter physics and electroweak phase transition**. 2020. Master Thesis (Department of Physics and Astronomy) – University of Heidelberg, Heidelberg, 2020.

153 ARHRIB, A.; BENBRIK, R.; GAUR, N. H$\rightarrow \gamma\ \gamma$ in the inert higgs doublet model. **Physical Review D**, APS, v. 85, n. 9, p. 095021, 2012.

154 QUEIROZ, F. S.; YAGUNA, C. E. The cta aims at the inert doublet model. **Journal of Cosmology and Astroparticle Physics**, IOP Publishing, v. 2016, n. 02, p. 038, 2016.

155 PESKIN, M. E.; TAKEUCHI, T. Estimation of oblique electroweak corrections. **Physical Review D**, APS, v. 46, n. 1, p. 381, 1992.

156 BARBIERI, R.; HALL, L. J.; RYCHKOV, V. S. Improved naturalness with a heavy higgs boson: an alternative road to cern LHC physics. **Physical Review D**, APS, v. 74, n. 1, p. 015007, 2006.

157 GFITTER GROUP. *et al.* The global electroweak fit at NNLO and prospects for the LHC and ILC. **The European Physical Journal C**, Springer, v. 74, p. 1–14, 2014.

158 BANERJEE, S. *et al.* Relic density of dark matter in the inert doublet model beyond leading order: The heavy mass case. **Physical Review D**, APS, v. 100, n. 9, p. 095024, 2019.

159 DUANGCHAN, C. *et al.* CTA sensitivity on TeV scale dark matter models with complementary limits from direct detection. **Journal of Cosmology and Astroparticle Physics**, IOP Publishing, v. 2022, n. 05, p. 038, 2022.

160 BÉLANGER, G. *et al.* micromegas5. 0: Freeze-in. **Computer Physics Communications**, Elsevier, v. 231, p. 173–186, 2018.

161 GARCIA-CELY, C.; GUSTAFSSON, M.; IBARRA, A. Probing the inert doublet dark matter model with cherenkov telescopes. **Journal of Cosmology and Astroparticle Physics**, IOP Publishing, v. 2016, n. 02, p. 043, 2016.

162 SILVERWOOD, H. *et al.* A realistic assessment of the cta sensitivity to dark matter annihilation. **Journal of Cosmology and Astroparticle Physics**, IOP Publishing, v. 2015, n. 03, p. 055, 2015.

163 LEFRANC, V. *et al.* Prospects for annihilating dark matter in the inner galactic halo by the cherenkov telescope array. **Physical Review D**, APS, v. 91, n. 12, p. 122003, 2015.

164 BELANGER, G.; BOUDJEMA, F.; PUKHOV, A. micromegas: a code for the calculation of dark matter properties in generic models of particle interaction. 2014. Available at: https://arxiv.org/pdf/1402.0787.pdf. Accessible at: 23 Jan. 2024. DOI: 10.1142/9789814390163 0012.

165 ALGUERO, G. *et al.* **The micromegas user's manual, version 5.3. 34**. 2022. Available at: https://lapth.cnrs.fr/micromegas/v5.3.35/manual_5.3.41.pdf. Accessible at: 23 Jan. 2024.

166 BELYAEV, A.; CHRISTENSEN, N. D.; PUKHOV, A. Calchep 3.4 for collider physics within and beyond the standard model. **Computer Physics Communications**, Elsevier, v. 184, n. 7, p. 1729–1769, 2013.

167 AGGARWAL, A. **MicrOMEGAs:** a code for the calculation of dark matter properties including the relic density, direct and indirect rates in a general supersymmetric model and other models of new physics. 2022. Available at: https://lapth.cnrs.fr/micromegas/. Accessible at: 23 Jan. 2024.

168 GARCIA-CELY, C.; IBARRA, A. Novel gamma-ray spectral features in the inert doublet model. **Journal of Cosmology and Astroparticle Physics**, IOP Publishing, v. 2013, n. 09, p. 025, 2013.

169 CELY, C. A. G. **Dark matter phenomenology in scalar extensions of the standard model**. 2014. Ph D. Thesis (Doctor) – Technische Universität München, Müchen, 2014.